UNIVERSIDAD COMPLUTENSE DE MADRID
FACULTAD DE CIENCIAS FÍSICAS

TESIS DOCTORAL

Electrochemical effects in doping with ionic liquids: the case of cuprate superconductor $YBa_2Cu_3O_{7-x}$

Efectos electroquímicos en el dopado con líquidos iónicos: el caso del cuprato superconductor $YBa_2Cu_3O_{7-x}$

MEMORIA PARA OPTAR AL GRADO DE DOCTORA

PRESENTADA POR

Ana María Pérez Muñoz

DIRECTORES

Jacobo Santamaría Sánchez-Barriga
Javier García Barriocanal

Madrid, 2018

Facultad de Ciencias Físicas

Universidad Complutense de Madrid

Electrochemical effects in doping with ionic liquids: the case of cuprate superconductor $YBa_2Cu_3O_{7-X}$

Efectos electroquímicos en el dopado con líquidos iónicos: el caso del cuprato superconductor $YBa_2Cu_3O_{7-X}$

Memoria presentada por
Ana Mª Pérez Muñoz
para optar al grado de Doctor en Ciencias Físicas

Directores:
Jacobo Santamaría Sánchez-Barriga
Javier García Barriocanal

Madrid, 2016

Content

CHAPTER 1

Introduction

1 Motivation

The use of an electric field to modulate the charge density of a material in a controlled way is extensively used in metal oxide semiconductor MOS technology. It is also a promising technique to manipulate the properties of complex oxides to generate new devices with exciting functionalities for novel-generation electronics. Many correlated oxides exist in the vicinity of a metal to insulator transition and, as such, their rich phase diagrams are critically controlled by the charge density [1]. Gating experiments allowing its controlled modification have attracted much attention [2–8], and in recent years unprecedented changes in the carrier concentration of complex materials have been achieved by using Electric Double Layer (EDL) techniques that employ ionic liquids as gate dielectrics [9–11]. Superconductivity has been induced in otherwise band insulating materials such as $SrTiO_3$ [12], ZrNCl [13], $KTaO_3$ [14] or MoS_2 [15] and the superconducting properties of several cuprates have been tuned to the insulating state [16–20]. These results have focused much attention on the EDL technique not only from an applied point of view but also for providing an opportunity to obtain fundamental knowledge about the phase diagrams.

Specifically, in the case of high temperature cuprate superconductors [16, 18–21] a striking similarity between the bulk phase diagram and the one achieved with the EDL technique was observed. This settled that the application of positive gate voltages to hole-doped cuprate EDL transistors induces the depletion of charge carriers. However, recent results obtained with EDL transistors based on VO_2 have challenged the conventional interpretation that EDL doping of oxides is due only to the electrostatic screening of the accumulated charges at the interfaces showing

that it also involves the migration of oxygen atoms of the crystallographic unit cell [22, 23]. These results highlight the necessity of careful studies of the mechanism of doping induced by the electric field generated at the interface between the tested material and the ionic liquid to fully understand the innermost origin of the generated electric charge.

In this thesis, we revisit the superconductor to insulator transition of $YBa_2Cu_3O_{7-x}$ (YBCO) induced by means of the EDL technique. To address the doping mechanisms involved in the IL- gating different experiments have been carried out being the "in-situ" hard x-ray absorption spectroscopy measurements while doping the cornerstone experiment of this thesis. We have tuned the cuprate from superconductor to insulator by applying positive gate voltages to an EDL transistor while measuring absorption spectra in the Cu K-edge. Density functional theory calculations show that the spectral changes found at the absorption edges arise from oxygen depletion of the CuO_x chains. Experiments using intermediate layers acting as oxygen barriers and oxygen reservoirs confirm that the effect of the large electric field at the interface between the ionic liquid and the YBCO induces the electromigration of oxygen ions from the CuO_x chains. The charge transfer between CuO_2 planes and CuO_X chains yielding superconducting planes is therefore hindered and the superconductivity suppressed. Impedance spectroscopy measurements verify the scenario of creation of oxygen vacancies indicating electrochemical reactions in the ionic liquid(IL)-YBCO interface while doping.

This thesis provides direct evidence of deoxygenation in ionic liquid gating of YBCO and the results exposed here outline the importance of electrochemical processes in doping with ionic liquids. We have demonstrated that EDL involves atomic displacements associated to the very strong electric fields generated at the interface of the cuprate and the ionic liquid and it should not be regarded equivalent to chemical doping or conventional electrostatic doping using solid gates.

2 Thesis Outline

- Chapter 2: this chapter is a general background introduction concerning electric field-driven metal-insulator transitions. The physics behind transition metal oxides is described, in particular, Mott insulators which are appealing candidates for field-effect experiments due to the existence of many competing states. In addition, a detail de explanation of the phase diagram, and the crystal and electronic structure of the high Tc superconductor $YBa_2Cu_30_7$ (YBCO) is given. The possibility to modify the physical properties of condensed matter systems by controlling the charge carrier density has become crucial. A brief exploring the theoretical and experimental historical evolution of electric field-driven switching devices is presented introducing the new and novel electrostatic double layer transistors (EDLT).

- Chapter 3: in this chapter the experimental techniques that are used through the thesis are briefly explained. Details of the growth method, structural and spectroscopy characterization are given; in particular X-ray absorption spectroscopy (XAS) describing specifically XANES and EXFAS technique.

- Chapter 4: in this chapter it is summarized the device fabrication and patterning of the electrostatic double layer transistor (EDLT). YBCO thin layer, trilayers with PBCO and superlattices have been characterized to optimized the growth conditions. In addition, a full impedance spectroscopy characterization has been done to analyses the IL. The operation of the EDLT and the measurement procedure is described in detail.

- Chapter 5: The aim of this chapter is to give a first approximation of the operation of the EDL transistor by studying the YBCO superconductor-insulator transition and to analyze the reversibility of the process by means of the disorder induced in the sample.

- Chapter 6: This chapter is the cornerstone to understand the doping mechanism behind the YBCO IL-doping. In situ X-ray absorption measurements have been done while doping in an EDL configuration. Pronounced spectral changes are observed at the Cu K-edge, evidencing a deoxygenation of the CuO chains in the YBCO, that have been studied using ligand field molecular orbital theory and have been confirmed by first principles density functional theory (DFT) simulations.

- Chapter 7: To further verify the scenario of creation of oxygen vacancies by electromigration, two different gating experiments have been carried out introducing insulating interlayers (either Al_2O_3 and $PrBa_2Cu_3O_7$ (PBCO)) between the YBCO and the ionic liquid for the examination of the role of oxygen out-diffusion from the sample during the doping process.

- Chapter 8: Impedance spectroscopy measurements have been done as a direct method to differentiate and characterize electrochemical reactions while IL-doping a YBCO think film layer. It has allowed us to discover the boundaries of the electrostatic and electrochemical processes at the IL-YBCO interface during the EDL formation evidencing and supporting the two step-doping process scenario governed by the creation of oxygen vacancies.

- Chapter 9: In this chapter the general conclusions and results are described in detail.

CHAPTER 2

Background

1 Introduction

A wide variety of experimental results and theoretical investigations in recent years have convincingly demonstrated that several transition metal oxides and other materials have dominant states that are not spatially homogeneous. This occurs in cases in which several physical interactions—spin, charge, lattice, and/or orbital—are simultaneously active. This phenomenon causes interesting effects, such as colossal magnetoresistance (CMR), and it also appears crucial to understand the high-temperature superconductors (HTSC).

The spontaneous emergence of electronic nanometer-scale structures in transition metal oxides, and the existence of many competing states, are properties that could have potential consequences for applications of correlated electronic materials, because not only charge (semiconducting electronic), or charge and spin (spintronics) are of relevance, but in addition the lattice and orbital degrees of freedom are active, leading to giant responses to small perturbations. Moreover, several metallic and insulating phases compete, increasing the potential for novel behavior.

The understanding of these oxides has dramatically challenged our view of solids. In fact, after one of the largest research efforts ever in physics, involving hundreds of scientists, even basic properties of the HTSC cuprates, such as the pairing mechanism, linear resistivity, and pseudogap phase, are still only poorly understood.

The aim of this chapter is to provide relevant background information pertaining to electric field-driven metal-insulator transitions. We begin with a general introduction to the physics metal-insulator transition. This is followed by a

description of the basic properties of YBCO, including its phase diagram, crystal structure and electronic structure. Finally, some recent theoretical and experimental conclusions of electric field-driven switching in those materials have been reviewed, introducing the new and novel electrostatic double layer transistors (EDLT).

2 Transition metal oxides

Transition Metal oxides (TMO) are oxide compounds based on combination of oxygen with atomic number elements between 22 and 29 (Ti, V, Cr, Mn, Fe, Co, Ni, Cu). To this group belong a wide range of materials, from the ancient magnetite (Fe_3O_4) already known in the old Grece, to more modern systems, like the cuprate superconductors or the managites. All those systems present electronic correlations and their physical properties cannot be explained in a simple way based on their electronic structure [24].

The localization of its electrons together with the directional bonding limits the screening electrostatic repulsion. Electrons have thus low motilities and strongly feel the lattice giving rise to the strong electron lattice coupling (Jahn-Teller) which may further split the degeneracy of crystal field levels. Most of this compounds have a perovskite structure due to the Metal Transition (MT) ions are surrounded by oxygen ions (O_2^-) in octahedral, pyramidal or square environments. Transition metal oxides have in common the presence of 3d electrons The five d degenerated states in a spherical potential, feel the electrostatic potential (Madelung) due to the negative oxygen ions what breaks the degenerating of the states.

The multiplicity of competing phases with similar characteristic energies in transition metal oxides leads to rich phase diagrams and inhomogeneous ground states [25]. The competition between interactions underlies the complex (often giant) collective responses exhibited by these materials upon small perturbations whose understanding and prediction remains a major challenge of condensed matter physics for the years to come [26].

In recent years growing and characterizing heterostructures combining complex transition metal oxides has also attracted the interest of the scientific community. A rich variety of new effects and phenomena have been found at oxide interfaces nucleating novel phases in a process called electronic reconstruction [27–29].The fabrication technique of these oxide heterostructures has reached a level of control comparable to the semiconductor technology and interfaces can be grown with atomic precision allowing the lattices with dissimilar materials to match with a high degree of crystalline perfection.

Much in the same way, field effect experiments of transition metal oxides have become an appealing playground for the exploration of exciting new physics behind those novel and complex materials opening a whole new route for technological development and designing of new devices.

In transition metal oxides interactions combined with low dimensionality lead to novel phases, which are strongly influenced by the carrier concentration [1]. Because the carrier concentration is a crucial parameter that governs the properties of these systems, the electrostatic field effect approach is an ideal tool to investigate the physics of correlated electron systems, allowing controlled and reversible changes of the carrier density without altering the disorder.

Despite the technical challenges of fabricating transition metal oxide FETs, the notion of switching exotic behaviors (such as superconductivity) on and off just by turning the knob on a power supply is so tempting that dozens of groups have addressed these obstacles, with experiments starting as early as 1960 [30]. One can also consider the possibility of achieving electric-field-tuned metal–insulator phase transitions, an idea that has being explored over the last decade for applications based on oxide channel FETs operating at room temperature [31].

The field effect, which has been so spectacularly successful in its application to semiconductors, is only in its infancy in exotic correlated systems; the combination of advanced twentyfirst- century techniques with this new materials approach offers broad perspectives for basic science and technology [2].

3 Metal-Insulator Transitions

3.1 Mott insulators

The basic model to describe the electronic structure of a solid is the conventional band theory, which takes in account the Bloch theorem and describes the electrons moving in a periodic lattice as a periodic plane wave. The electrons are moving freely in an effective periodic potential imposed by ions and other electrons, and are scattered by impurities in the lattice. The periodic potential makes electron dispersion curves discontinue at Brillouin zone boundaries opening gaps in the energy space, and forming energy bands. Therefore, metals contain a partially filled band while insulators' electron bands are fully occupied at zero temperature.

This simple single electron band picture, that works exceptionally well in many materials, is not sufficient because it neglects disorder-electron interaction (induced Anderson localization), phonon-electron interaction (induced Peierls transition) and electron-electron interaction (induced Mott transition) or treats them as perturbations. Consequently, in some scenarios where these interactions become strong, it is expected that the above approximation would fail to provide a full account of corresponding physical phenomena.

The electron-electron interaction gives rise to the so-called "strongly correlated electron materials", which includes any material having emergent physical properties that are strongly influenced by the interactions between its electrons. The electron-electron interactions need not always be Coulomb repulsion in nature, and they can involve spin, lattice and orbital coupling as well.

To appreciate the strongly correlated material's place in the universe, it is instructive to consider the full spectrum of possible crystalline condensed matter systems, sorted by the degree to which their electrons' probability density functions are localized, as depicted in Figure 2.1. In one extreme, electrons are tightly bound to their donor nuclei and have spatially localized wave functions. These states have discrete energy levels, just as they would in an isolated atom. In the other extreme, nearly free electrons exist as delocalized Bloch waves. The energy levels of these states form continuous bands, and the filling of these bands determine whether the system is insulating or conducting. Strongly correlated

electron materials exist in the middle ground between these two extremes, and they can demonstrate a multitude of exotic and technologically useful properties such as high-temperature superconductivity [32, 33], ferroelectricity [34], half-metallicity [35], colossal magnetoresistance [36], and metal-to-insulator transitions [1].

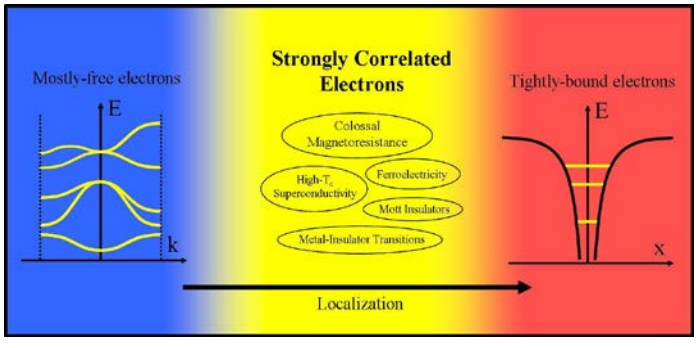

Figure 2.1. A generalized spectrum of condensed matter systems, sorted by degree of electron localization. Strongly correlated materials lie in the fertile middle ground between systems with mostly-free electrons and systems with tightly-bound electrons, and they are host to a number of materials with exotic and technologically useful properties. From Ref [37].

In the framework of solid-state physics, electron-electron interactions are responsible for opening up an energy gap *U* that splits what would otherwise be a metallic, half-filled conduction band into a filled Lower Hubbard Band (LHB) and an empty Upper Hubbard Band (UHB) [1, 38]. This is the well-known Hubbard model[39] and those insulators materials with strong electron correlations are called as Mott insulators[40].

A Mott insulator can be generally characterized as a material whose conduction electrons are gridlocked into a traffic jam that impedes the normal flow of current. This gridlock is created because the material has one electron in the valence band per atomic site, and Coulomb repulsion forces make the double occupation of these sites energetically unfavorable, as depicted in Figure 2.2

For example, in the above tight-binding model, conduction happens by electrons hopping through the lattice from one site to another. When the electron is to hop from its original site to a new site, which is already occupied by another electron,

it will experience Coulomb repulsion from the electron in the new site. If the Coulomb repulsion energy *U* or blockade is much larger than electrons' kinetic energy, electrons would be bounded to their original sites instead of being itinerant in the lattice.

Since this insulating state requires exactly one electron per site, the transport properties should be extremely sensitive to even incremental changes in carrier density. This property of Mott insulators is what makes them an appealing candidate for field-effect experiments [31, 41].

Furthermore, these properties can be highly sensitive to carrier concentration, opening up the possibility for a whole new class of proposed field-effect devices [2, 3].

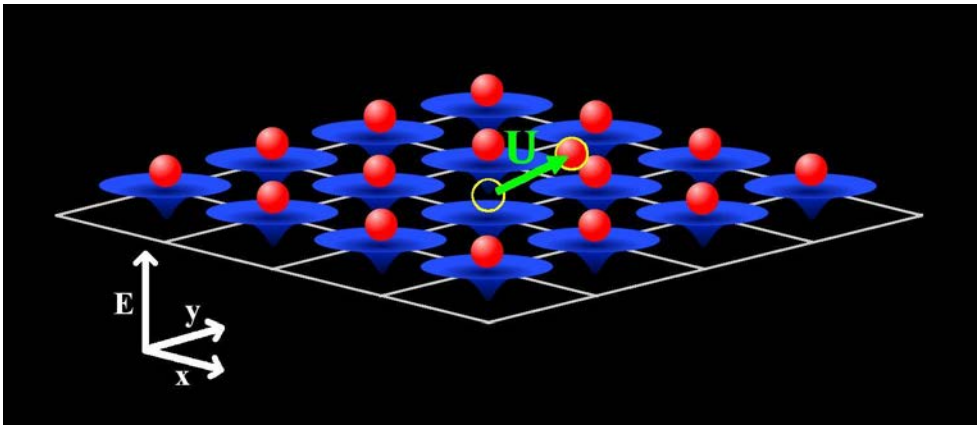

Figure 2.2. A simple picture of the gridlocked electrons in a Mott insulator. At an integer filling of electrons per site, conduction is blocked by the Coulomb repulsion energy U that must be provided for two electrons to occupy the same site. Fro, Ref [37].

3.2 The Mott-Hubbard Model

One of the models that can appropriately describe the behavior *d*-electrons in crystals is the so-called single-band Hubbard model [40][42]. The Hamiltonian in this model is given in equation:

$$H = \underbrace{-t\sum_{\langle i,j\rangle,\sigma} c_{i,\sigma}^{+}c_{j,\sigma} + V\sum_{i,\sigma} n_{i\sigma}}_{\text{n.n.tight binding}} + \underbrace{U\sum_{i} n_{i\uparrow}n_{i\downarrow}}_{\text{on-site repulsion}} \quad (1)$$

Where *H* is the system's Hamiltonian operator, *t* is the hopping integral, c^{+} and *c* are the creation and annihilation operators for a *d*-electron on site *i* with a spin σ, *U* is the Coulomb repulsion energy, and n_i is the number operator [42][43].

This Hamiltonian is in some sense the simplest possible description of an interacting system including the possibility of electron hopping as well as the effect of Coulomb integration between electrons. The first term describes the free electron lattice model, the simplest tight binding approximation with only nearest neighbor hopping. The second term is the possible interaction term, an on-site repulsion, only relevant when two electrons occupy the same site.

The kinetic term of the Hamiltonian is controlled by the hopping between neighboring ions and it is proportional to the hopping integral t, that is a perturbation of the state. The Pauli exclusion principle makes that the second order process, that implies the hopping of the electron to the neighbor orbital would just occur if the spins are antiparalel by supplying the energy U.

This non-degenerated Hubbard model ignores such complications as a possible orbital degeneracy, but it is sufficient for a description of both insulating and metallic states of our system.

As is well known, for weak interaction $U<<t$ the model describes the metallic state even for an exactly half-filled band with one electron per site, independent of the distance between corresponding sites.

It is clear however that for a large enough distance between sites, $t<<U$ which means small hopping matrix element *t*, the ground state should be insulating with electrons localized each at its site. In addition, it leads to an antiferromagnetic exchange interaction between its localized magnetic moments. This state is the so-called Mott insulator, with and energy gap $E_g \sim U - t$ and it is due to the second term in the Hamiltonian, the on-site Coulomb repulsion.

The Hubbard model predicts that when *U/t* is large enough, which will occur for large values of lattice spacing, the half-filled band will split into an Upper and Lower Hubbard Band shown in Figure 2.3(a). The lower band will be fully occupied and the upper band will be empty, which is characteristic of an insulator. As described in the previous section the physical picture corresponding to this mathematical description is that the electrons become gridlocked into a traffic jam, one per each atomic site. No electron can move to any other site because it would have to pay an extra energy *U* to accommodate the double occupation.

Reducing Coulomb repulsion *U* to a certain critical value could merge the two Hubbard Bands and induce an insulator to metal transition. The density of states with varying relative magnitude of Coulomb repulsion to bandwidth *W* is shown in Figure 2.3(b). Note that in the Hubbard model, a higher value of *U* leads to insulating behavior, and a higher value of *W* (or *t*) leads to metallic behavior.

For example, in transition metal oxides, the Coulomb repulsion energy *U* is usually a few eV (~1 to 10 eV) [44] whereas the bandwidth of *d* band are often quite small (~1 to 2 eV) because of the tight binding nature of *d* orbitals [45]. Notice that for conventional semiconductors such as Si and Ge, the bandwidth is usually much larger ~10 - 20 eV [46] with similar on-site Coulomb repulsion *U* to TMOs[47], which gives a hint on why correlation effect is not as important in conventional semiconductors.

While the above band closing picture of insulator-to-metal transition could reflect many aspects of the insulating side of the MIT because it starts from the limit of large *U*, it does not provide a good description of the metallic state [48].

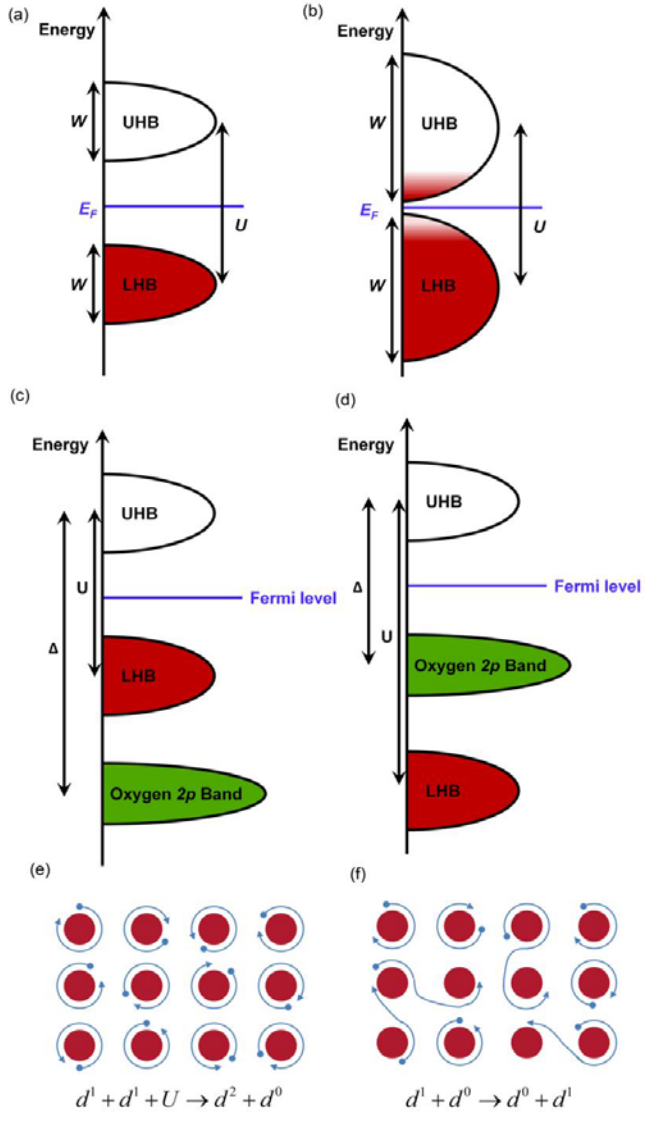

Figure 2.3. (a) Splitting of a normal band into upper and lower Hubbard band due to electron correlations. (b) Bandwidth controlled metal-insulator transition. Changing the bandwidth *W* could induce a metal-insulator transition. (c) and (d) Oxide Mott insulators could be categorized into two types based on the relative position of the oxygen band and Hubbard bands [49](c) Mott-Hubbard insulator where the oxygen p-band lies under the lower Hubbard band. (d) Charge-transfer insulator where oxygen p-band is in between the lower Hubbard band and upper Hubbard band. (e) and (f) Doping holes or electrons into a Mott insulator could lead to a phase transition from insulator to metal. (e) In an undoped Mott insulator (n=1), electron hopping leads to formation of a doubly

occupied site and increase in total energy because of the Coulomb repulsion between two electrons. (f) In a Mott insulator with hole doping (n<1), electron hopping does not create doubly occupied sites and system total energy does not change. Electrons could move freely in the matrix and the material becomes metallic. (Panels c and d adapted from Zaanen et al. [49]; panels e and f adapted from Fujimori. [50]).

It should be noted, however, that the precise details of any real system are vastly more complex than the simple Hubbard Model. Spin, orbital, and lattice interactions can all add additional degrees of freedom to the system that greatly complicate first-principles calculations. We direct the interested reader to [1]for an excellent discussion of this topic.

3.3 Two Routes across the Metal-Insulator Transition

In the Hubbard model, the electron filling and the ratio *U/W* between the Coulomb repulsion energy *U* and the electron band width *W* (or *t*) both turn out to be very critical parameters that can drive metal-insulator transitions.

The Mott metal-insulator transitions discussed heretofore are all induced by tuning relative magnitude of the Coulomb repulsion *U* to bandwidth *W* at fixed band-filling (half-filling), which is called *bandwidth controlled metal-insulator transition (BC-MIT).* One example of this is applying stress on a Mott insulator to change the atom spacing and consequently bandwidth to induce a metal-insulator transition without changing the carrier density.

The other way to induce a metal-insulator transition in a correlated electron system is to change the band-filling. This kind of transition controlled by carrier density is called *band-filling controlled metal-insulator transition (FC-MIT).* In other words, to dope the upper (lower) Hubbard band with holes (electrons). Figure 2.3(e) and (f) illustrates how carrier doping could induce metallic phase in a Mott insulator [50]. At exact half-filling, electrons cannot hop to another site due to Coulomb repulsion and all the sites are singly occupied. If holes are doped into the insulator, however, some atom sites become unoccupied and the nearby electrons could move freely onto this unoccupied site, because the total energy is the same before and after the hopping. The original insulator now becomes metallic. Similarly, doping electrons into the insulator also makes electrons to hop freely through those unoccupied atom sites.

These two different routes to a metal-insulator transition in a correlated electron system are depicted in Figure 2.4.

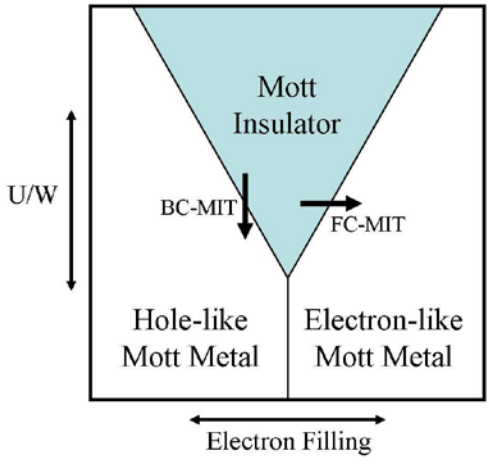

Figure 2.4. Reproduced from [1], the phase diagram of a Mott-Hubbard system as a function of electron filling and U/W. Two routes of transitioning across the metal-insulator boundary are depicted. The metallic state in the shaded region is highly sensitive to disorder-induced localization.

3.4 Mott-Hubbard vs. Charge-Transfer Insulators

In contrast to the idealized model (1), in real oxides, there are ligands (oxygen ions) between the Transition Metal (TM) ions. Consequently, hopping of d-electrons from site to site (first term in Hamiltonian) occurs not directly but via oxygen p-orbitals.

In many cases the oxygen p-states can be excluded and this reduces the description to the effective model (1); however, this is not always the case. Accordingly oxide Mott insulators could be categorized into two types [49]: *Mott-Hubbard insulators (MH)* for which the description given above applies without any restriction and *Charge-Transfer insulators (CT*) in which one should treat oxygen p-states.

The basic general Hamiltonian describing both the d-electrons of the TM and the p-electrons of oxygen assuming there is no hybridization between transition metal *3d* band and oxygen *2p* band, has the form

$$H = \sum \varepsilon_d d_{i\sigma}^{+} d_{i\sigma} + \varepsilon_p p_{j\sigma}^{+} p_{j\sigma} + t_{pd}\left(d_{i\sigma}^{+} p_{j\sigma} + h.c\right) + U n_{di\uparrow} n_{di\downarrow} \quad (2)$$

Depending on the ratio of the charge-transfer excitation energy $\Delta = \varepsilon_d - \varepsilon_p$ and the Coulomb repulsion U (Figure 2.5), a division into two groups can be made.

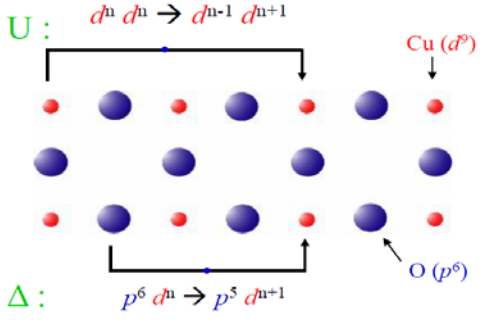

Figure 2.5. Description of the charge-transfer excitation energy and the Coulomb repulsion.

If the oxygen p-levels lie deep enough, $\Delta \gg U$, the lowest charged exited states are those corresponding to the transfer of a d-electron from one TM site to another:

$$d^n + d^n \rightarrow d^{n-1} + d^{n+1} \quad (3)$$

This process as described above costs and energy *U* and for $U \gg t$ gives the Mott-Hubbard insulating state. Still even in this case real hopping occurs via the oxygen p-states, but it can be excluded in the perturbation theory.

On the other hand there may be situations, where the charge-transfer energy $\Delta = \varepsilon_d - \varepsilon_p$ (the energy necessary to transfer an electron from the filled 2p-level of O^{2-} to a d-level of a neighboring TM) is less than *U*. In this case, $\Delta < U$, the lowest charge-carrying excitations will be just these excitations: the transfer of an electron from the oxygen to the TM, or the transfer of a hole to an oxygen:

$$d^n p^6 \rightarrow d^{n+1} p^5 \equiv d^{n+1}\underline{L} \quad (4)$$

(The notation $\underline{L}$ is very often used nowadays and means “ligand hole”-the state with one electron on a ligand-here oxygen-missing).

According to this division we may draw a general phase diagram, the so called Zaanen-Sawatzky-Allen (ZSA) [49] diagram, shown in the Figure 2.6.

The difference between these two situations is depicted in Figure 2.3 (c) and (d). When $U > \Delta$, we get the normal case of a Mott-Hubbard insulator where the partially filled *d* band is split by the Coulomb repulsion energy *U*. However, when $U < \Delta$, the resulting conduction gap is decreased to Δ, and lies between the Upper Hubbard Band and the filled *p* band.

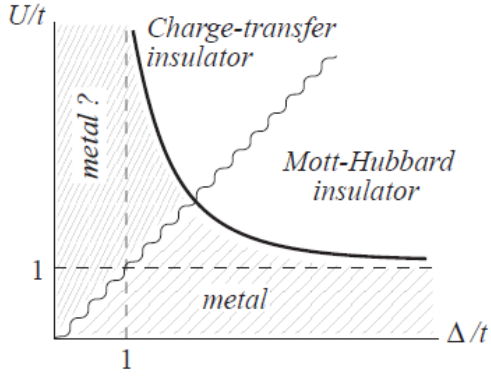

Figure 2.6. Zaanen-Sawatzky-Allen diagram plotting the boundary between Mott-Hubbard ($U > \Delta$) and charge-transfer ($U < \Delta$) insulators.

Most of the transition metal oxides belong to one of these two categories.

To conclude, the repulsive interaction between electrons of the same ion and the same orbital U, typically 6-8eV is the responsible of the antiferromagnetic alignment (AF) whereas the direct canje [51] that has a ferromagnetic nature has its origin in the exchange of electrons of the same orbital but from different neighbors. For electrons of the same ion but different orbital, the Hund rules introduce a ferromagnetic interaction between spins that is usually 1 eV.

Partially filled d-shells determine their magnetic properties, an exchange interaction is mostly due to a virtual hopping via intermediate oxygen (supercharge mechanism) [52]. A lot of metal transition oxides, particularly the parent compounds are AF insulators. Details of the resulting magnetic structure depend on the type of d-orbitals occupied on the geometrical arrangement of corresponding ions following the so called Goodenough-Kanamori-Anderson rules that determine the sign of the exchange depending of the orbital filling [52–54].

This strong interplay between magnetic structure and transport properties makes these systems so interesting and promising for possible applications in spin electronics.

4 Superconductivity

Superconductivity refers to perfect electrical conductivity in a material. That is, once an electrical current is established, it will flow indefinitely for given temperature range. It arises from the pairing of free electrons, which makes them immune to external disturbances such as scattering off by defects.

Superconductivity was discovered in 1911 by Heike Kamerlingh Onnes [55], three years after he had first liquefied ^{4}He. He observed that the electrical resistance of various metals such as mercury, lead, and tin disappeared completely over small temperature ranges below a critical temperature T_c. Furthermore, when a material is superconducting, it exhibits not only a zero electrical resistance, but bulk materials expel magnetic field lines below a critical value that is material dependent. This is called the Meissner-Ochsenfeld effect [56]. The microscopic nature of superconductivity in conventional superconductors was not well understood until the late 1950's. The first well-accepted theoretical model of superconductivity was proposed in 1957 by three collaborators John Bardeen, Leon Neil Cooper, and John Robert Schrieffer, commonly known as the BCS theory [57], for which they received the Nobel Prize in 1972.

BCS realized that superconductivity could not be explained purely in terms of electrons and their interactions, and that phonons (quantized lattice vibrations) needed to be included as well.

The BCS model describes as a macroscopic phenomenon induced by a microscopic effect caused by a "*condensation*" of pairs of electrons into boson-like states, called Copper pairs. Cooper pair consists of two *'free'* electrons with opposite momenta and spins near the Fermi level of the system [57]. At sufficiently low temperatures the electrons would experience an attractive interaction that would attract each other rather to repel. Electrons near the Fermi surface with an attractive interaction become unstable against the formation of "Cooper pairs", which leads to a lower energy state below certain temperature and would undergo a phase transition to a superfluid phase that explained the loss of resistance. They showed such a condensation will occur no matter how weak the attractive interaction. This result is a consequence of Fermi statistics and of the existence of the Fermi-sea background in a many-body quantum system. An important energy scale parameter is the "superconducting gap", Δ, for the breaking of an electron pair. All excitations of the system involve the breaking of superconductor pairs, so the minimum energy of any excitation is Δ. In this way, there is a gap in the spectrum of electronic excitations below this value. For more information on the BCS theory of superconductivity, I refer the reader to the book by Tinkham [58].

There is a phenomenological model describing the behavior of superconductivity, proposed by V. Ginzburg and L. Landau, which is known as the Ginzburg–Landau (GL) theory [58, 59]. It does not explain the microscopic mechanisms giving rise to superconductivity. Instead, it examines the macroscopic properties of a superconductor. The GL theory is called a phenomenological theory as it describes some of the phenomena of superconductivity without explaining the underlying microscopic mechanism. However, later Gor'kov [60] was able to show that the GL theory was, in fact, a limiting form of the microscopic theory of BCS valid near the transition temperature T_c.

The BCS theory and GL theories together explain most of the properties of classical superconductors, such as the penetration depth, the electronic heat capacity, single-particle tunneling, and the frequency-dependent electromagnetic absorption, with remarkable success. However, they are not completely successful

in explaining the properties of high temperature superconductors such as the gap size and its symmetry among many other properties.

3.1 High-T_c Superconductor. Cuprates.

Conventional superconductors usually have transition temperatures below 30 K, whereas High-T_c superconductors (HTSCs) have been observed with transition temperatures as high as 138 K [61].The first high-T_c superconductor, a barium-doped compound of lanthanum and copper oxide, was discovered in 1986 by IBM researchers Georg Bednorz and K. Alex Müller [32], who were awarded the 1987 Nobel Prize in Physics. Until 2008, only certain compounds of copper and oxygen, the so-called "cuprates" were believed to have HTS properties, and the term high-temperature superconductor was used interchangeably with cuprate superconductor for compounds such yttrium barium copper oxide (YBCO). However, several iron-based compounds (the iron pnictides) are also known now to be superconducting at high temperatures [62][63].

High-Tc superconductors (HTSCs), such as the cuprates, have been intensively studied for more than two decades gathering one of the strongest research efforts in the history of science in terms of number and impact of research articles and number of researchers involved. In spite of many efforts, there is currently no complete and agreed upon theoretical description of their behavior. The cuprate systems continues attracting interest, not only because they show high-T_c superconductivity, technologically tantalizing, but also show various unusual behaviors in the vicinity of the filling-control Mott metal-insulator transition.

3.1.1 Models of the electronic structure of cuprates

A first insight into the electronic structure of cuprates may be obtained from an independent-particle model of the electronic states of the CuO_6 octahedra. In an ionic picture, Cu is expected to be divalent, i.e. there is one hole in the 3d level. In a cubic environment of O ions, the crystal field will split the 3d level into e_g and t_{2g} states (see Figure 2.7). The crystal field of the distorted O octahedron further splits up the e_g level into $3d_{x^2-y2}$ and $3d_{3z^2}$-r^2 states and the t_{2g} level into $3d_{xy}$, $3d_{xz,}$ and $3d_{yz}$ states. Hybridization of the Cu states with 2p states from in-plane O atoms leads to the formation of bands as shown in the middle of Figure 2.7. The

hybridization is strongest for the σ bonds between in-plane $Cu3d_{x^2-y^2}$ and in-plane $O2p_{x,y}$, states. This leads to bonding σ and antibonding σ* $Cu3d_{x^2-y^2}$ - $O2p_{x,y}$ bands. Filling the bands with the appropriate number of electrons leads to a half-filled antibonding σ* band. This indicates that in this independent-particle model, the cuprate should be a metal and that the states at the Fermi level should have $Cu3d_{x^2-y2}$ and $O2p_{x,y}$ character. However, as it is well-known that the undoped cuprates are antiferromagnetic insulators.

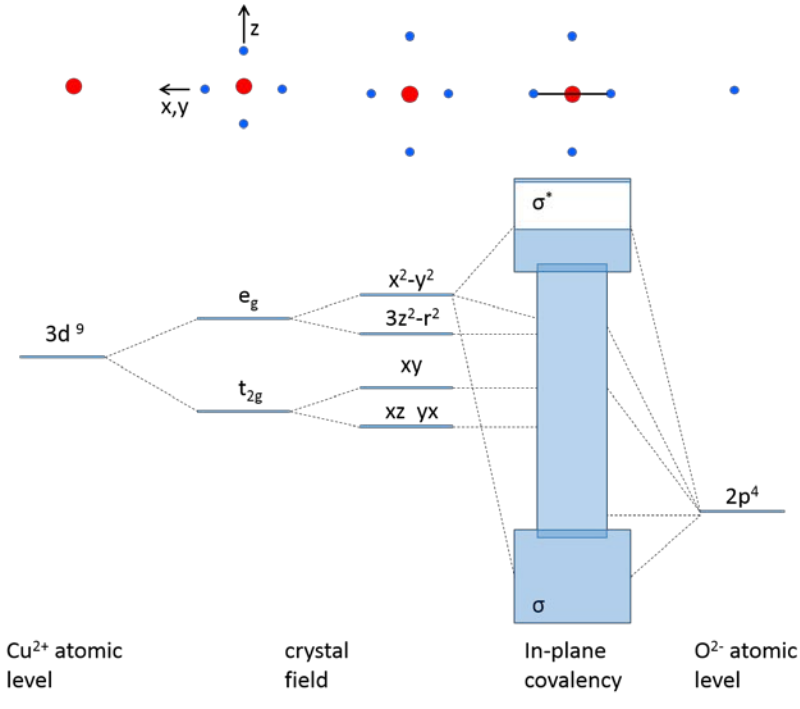

Figure 2.7. The formation of the electronic structure of the CuO_2 layers in La_2CuO_4. Left side: Crystal field splitting of a $Cu3d^9$ level in a regular and distorted octahedron of O ions. Right side: O2p6 level. Middle: Bands are formed by hybridization between Cu3d and O2p levels. In particular, the bonding and antibonding σ bands are shown.

Due to the strong on-site correlation effects on the Cu-sites, a lower (LHB) and an upper Hubbard band (UHB) are formed opening a gap. However, the Mott-Hubbard picture (eq.1) is not enough to explain the insulating behavior of undoped

CuO_2 planes. Already before the discovery of the HTSCs it was realized that the gap in the late transition-metal compounds is too small to be explained within a normal Mott-Hubbard picture[49, 64, 65].

Taking into account the two possible processes to understand the formation of a gap, holes jumping between Cu ions, and holes jumping from one Cu ion to a 2p oxygen orbital, the first one needs the energy scale U(≈8eV) and the second the need the charge transfer energy that in cuprates and niquelates is smaller than U[1]. The charge-transfer energy Δ, is estimated to be about 4eV [66–68]. It can be derived by the three-band extended Hubbard model (eq.2) [69] that includes the $Cu3d_{x^2-y^2}$ orbital and the two $O2p_{x,y}$ orbitals in the plane. Thus the parent compound of a cuprate is a Charge-Transfer-Insulator so that the energy gap is no longer determined by the Coulomb energy U as in the Mott-Hubbard insulator but by difference between the on-site energy of the Cu3d and O2p electrons, [49].

Different experiments were carried out in order to better understand the electronic properties of the cuprates. From the Reference[70] we will summarize the principal proposed models that have been considered to explain the superconductivity in this materials.

The charge-transfer model without considering the hybridization was found to have serious drawback when it was contrasted with angular resolved photoemission experiments [71–73] performed on p-type doped cuprates. Whereas in the charge transfer model without hybridization a small Fermi surface was expected, a large Fermi surface was experimentally observed in this studies. The hybridization could not be neglected.

When switching on the hybridization between O2p and Cu3d states in the charge transfer model it was found that the situation changed drastically [74, 75]. With increasing the hopping integral, t_{pd}, between $Cu3d_{x^2-y^2}$ and $O2p_{x,y}$ states, Cu3d states are mixed into the O2p valence band and O2p states are mixed into the UHB as well. Then, on a low energy scale the charge-transfer model transforms to an effective single-band Mott-Hubbard picture with an effective U of the order of Δ as was proposed by Anderson [76]and from the t-J model [77].

For p-type doping, the magnetic interaction between a hole on an O-site and a hole on a Cu-site was taken into account in the calculations leading to singlet and triplet states which were separated due to the exchange interaction. The proposed local singlet state, called Zhang-Rice singlet [77] allows to simplify the three-band model to an effective single band model. As can be seen in Figure 2.8(a) the hole in the ZRS state surrounds the Cu site and carries another 1/2 spin of the direction opposite to the spin of the *d* hole. That picture defines the lowest energy excitation from the occupied states (the singlet) to the Upper Hubbard band which is empty (Δ_{CT} =2eV) schematically illustrated in Figure 2.8 (b) and (d). The so-called Zhang-Rice singlet states were first detected as ionization states in photo-emission experiments. In this new model upon p-type or n-type doping, the Fermi level moves into the singlet band above the O2p band. Such studies in the *t-J* model [78] or using Monte Carlo data [79] predict a large Fermi surface in agreement with angular resolved photoemission measurements [71–73, 80]

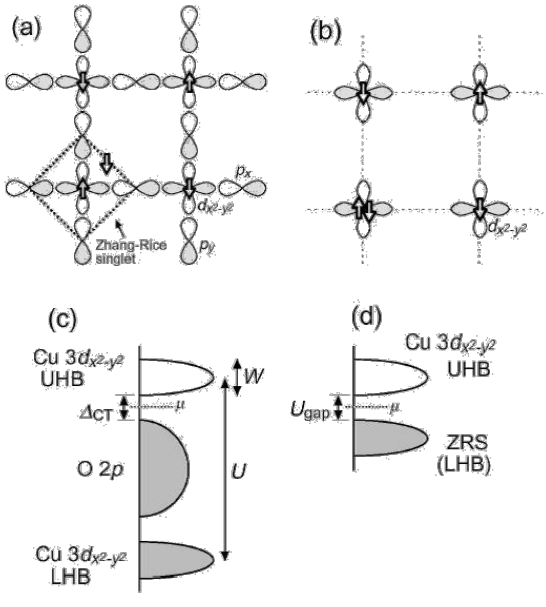

Figure 2.8: Schematic pictures for the electron orbitals (a)(b) and the electronic structure (c)(d) of the CuO_2 plane. Three bands, Cu 3 $d_{x^2-y^2}$, O $2p_x$ and $2p_y$, are considered in (a) and (c). Only the $d_{x^2-y^2}$ band at the Cu site is considered in (b) and (d).

The undoped cuprates are antiferromagnetic with a Neel temperature around 300K, however the AF correlations starts at higher temperatures as is shown in the ARPES experiments where the bands associated to the Zhang Rice singlet, are directly measured, showing similar results for the spectral density function.

Up to now, we have assumed that the low-energy properties of cuprates can be described by a three-band-model which uses only three in-plane orbitals, namely the $Cu3d_{x}^{2}$-y^2 and $O2p_{x,y}$ orbitals (σ-bonded to Cu3d). However there has been also lively debate as to whether a multi-band-model with other orbitals such as $Cu3d_{3z}^{2}$-r^2, $O2p_z$ orbitals from apical O sites above (and below) Cu sites, or in-plane $O2p_{x,y}$ (π-bonded to Cu3d) should be used to describe the transport properties and superconductivity in cuprates. An enhancement of T_c, by the anharmonicity of vibrations of apical oxygens was proposed by Müller [81]. A model of high-T, superconductivity based on d-d excitations was established by Weber [82] and Cox et al. [83] Kamimura and Eto [84] have proposed that the mobile holes in p-type doped high-T, superconductors are hybrids of $Cu3d_{3z}^{2}$-$r^2$and apical $O2p_z$, orbitals. In their model, in the superconducting state, these mobile holes are paired due to the interaction with localized hybrids of $Cu3d_{3z}^{2}$-$r^2$and $O2p_z$, orbitals. The importance of $Cu3d_{3z}^{2}$-r^2- $O2p_z$, hybrids and the formation of an "anti-Jahn-Teller" polaron has also been stressed by Anisimov et al. [85]. Their calculations predict an equal spectral weight of $Cu3d_{3z}^{2}$-r^2 states and $O2p_z$, states for the triplet polaron.

In contrast, other theories have predicted a suppression of superconductivity due to the influence of non-planar orbitals. Maekawa and co-workers [89] found a correlation between T_c, and the energy difference between apical $O2p_z$, states and planar $O2p_{x,y}$ states. From their analysis they conclude that in the high-T, compounds the Zhang-Rice singlet is stable. T_c, is reduced due to a destabilization of the singlets by a mixing with apical $O2p_z$, states. Similar work has been performed by Di Castro and co-workers [86, 87] analyzing a five-band extended Hubbard model in which the strong on-site Coulomb repulsion between holes on Cu sites is treated by means of a slave-boson approach in a mean-field approximation. Their main conclusion is that the highest critical temperature can be reached in the compounds where the interaction between apical oxygen(s) and the CuO_2 plane is weakest.

The question whether a multi-band approach is required has also been discussed by Eskes and Sawatzky [88]. In addition, Grant and McMahan [89] have stressed the importance of apical O2p, states in determining the nature and the dispersion of quasiparticle states of p-type doped cuprates.

To conclude, even though the electronic structure of the cuprates has been broadly studied, it is still nowadays a broad research topic to understand the fundamental physics behind the high T_c superconductors [90–92].

3.2. Physical properties of YBCO

3.2.1 Crystallographic structure

A structure feature common to most cuprates is the layered-perovskite crystal structure containing CuO2 planes separated by block layers. Usually the block layers are insulating and have almost no contributions to the low energy physics. On the other hand, CuO2 planes have energy states around the Fermi level (EF) and thus dominate the low energy physics. It is widely accepted that the superconducting properties are determined by carriers moving within the weakly coupled CuO_2 planes, while the other layers serve as reservoirs to dope electrons or holes onto the CuO_2 planes [32].

YBCO has an orthorhombic structure, which corresponds to the spatial group Pmmm, with lattice parameters; a=3.823A, b=3.886A, c=11.676A. The unit cell is a triple perovskite structure. The rare earth element Y is at the center of the unit cell, in the middle of two copper-oxide (CuO_2) planes which form two CuO_5 pyramids with apical oxygens. After that, there is a barium-oxide (BaO) plane (the oxygen is in the apical position of the octahedron centered in the Cu1 ion), and finally in the direction of the *b-axis*, the CuO chains. Frequently there is a deficiency of oxygen in that chain, explaining why the stoichiometry index of the oxygen is not an integer number, instead of that it can vary from 6 to 7.

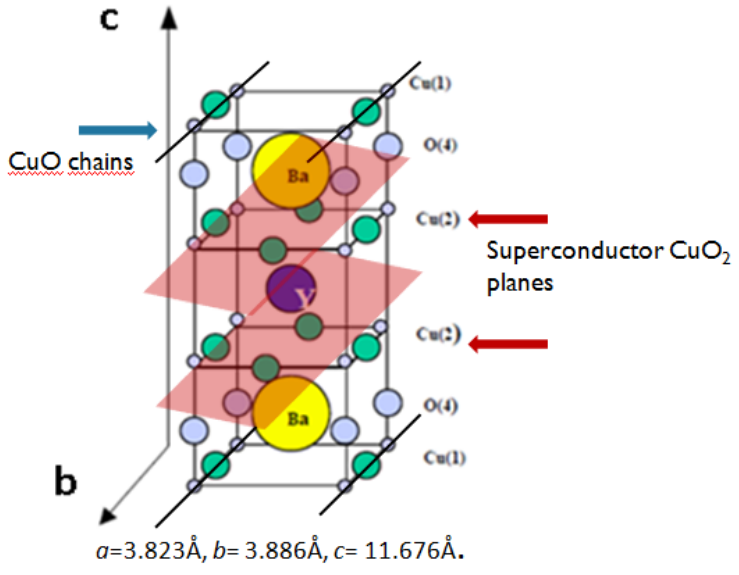

Figure 2.9. Unit cell of the superconductor YBCO.

The primary structural distinction between YBCO and other high-T_c cuprates is the presence of this one dimensional CuO chain aligned along *b*-axis. They play a role of a charge reservoir. Electrons are withdrawn from the CuO_2 planes by interexchanging electrons with the chains: there is a charge transfer from the CuO chains to the CuO_2 planes. In addition, YBCO, doping can be controlled by changing the oxygen content of the CuO chain. Therefore, in studying the electronic structure of YBCO, one should sort out the features related to the CuO chain and the influence of the chains on the electronic structure of the CuO_2 planes.

When O atoms are removed from the O(1) sites, the total system is reduced. In a first approximation, one can assume that until x = 6.5 mainly the CuO_2 planes are reduced leading to a filling of the holes in these planes. Ongoing from x = 6.5 to 6.0, a reduction of the divalent Cu(1) atoms to monovalent Cu(1) atoms is expected. For x = 6, the Cu(1) atoms are two-fold coordinated with O(4) atoms, i.e. there is an O(4)-Cu(l)-O(4) dumb-bell along the c-axis. Experimentally, the transition from a superconducting orthorhombic metal to an antiferromagnetic tetragonal insulator is observed around x = 6.35.

The Cu(2) atoms in the planes have strong covalent bonding to two O sites per unit cell, while the Cu(1) atoms in the chain have covalent bonding to three O sites. Therefore, the splitting between the bonding σ and the antibonding σ* Cu-O bands is larger in the chains than that in the planes. As in all cuprate superconductors, the σ* band of the plane in $YBa_2Cu_30_7$ is close to being half-filled. Therefore, it follows that the σ* band of the chains must be only slightly occupied. This view was supported by LDA band structure calculations of $YBa_2Cu_30_7$ [93–99].

3.2.2 The cuprate phase diagram

In the YBCO the so-called parent compound has an antiferromagnetic Mott insulating ground state in which Coulomb repulsion prevents electron hopping from Cu to Cu and the exchange correlation is antiferromagnetic. As it was said in the previous section cuprates can be viewed as doped Mott insulators [100].

When the system is doped with holes (removing electrons) the long distance AF order is destroyed and it shows metallic properties. The insulator to superconductor transition takes place at $\delta \sim 0.07$. Here, δ is the hole concentration per Cu in the CuO_2 plane. The region where the superconductivity is observed has an inverted bell shape reflecting that there is an optimal doping, from where above the critical temperature decreases again and can be approximately fitted to a parabolic curve [101, 102]. A schematic phase diagram of hole doped cuprates is shown in Figure 2.10 The maximum critical temperatures (T_c) of up to 92 K occur at an optimal hole-doping near $\delta \sim 0.16$. At zero doping, the antiferromagnetic Mott insulating state exists up to the Neél temperature. As the system is doped with holes the Neél temperature decreases, eventually vanishing.

Above the dome, there are three normal state regions: the pseudogap region, a non-Fermi-liquid (strange metal) region and a Fermi liquid region. For a small doping, the charge and spin properties shows the existence of a pseudogap where there is a suppression of the charge and spin excitations below a temperature T*>Tc [103, 104]. As holes are added, the anti-ferromagnetism prevents them from being mobile, as nearest neighbor hoping requires a spin flip. Below this optimal doping (underdoped area) anomalous metallic properties are found (strange metal) above Tc. For very high hole doping, there are only a few electrons left, and the chance

of double occupancy is small enough so that, in the overdoped area, a Fermi liquid picture is recovered.

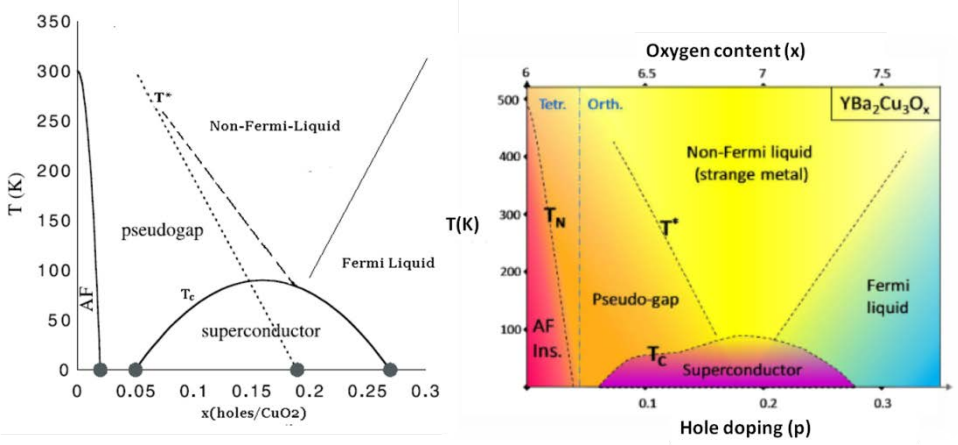

Figure 2.10 A schematic phase diagram for hole doped cuprates. The horizontal axis is the hole doping level (holes per copper atom), and the vertical axis is temperature. Adapted from Ref [105].

3.2.3 Transport properties

The transport properties of high-T_c cuprates are unusual in terms of standard Fermi-liquid theory. One of the most unusual properties is the temperature dependence of the resistivity. While Fermi-liquid theory predicts that the temperature dependence of the resistivity ρ is given by $\rho = \rho_0 + AT^2$, a nearly optimally doped y=6.90 sample shows a robust T-linear dependence, $\rho \sim \rho_0 + AT$, in a wide temperature range as shown in Figure 2.11. This T-linear behavior is widely observed around the optimum doping. In the underdoped region, ρ at low temperatures eventually shows insulating behavior in the way of logarithmic T dependence particularly when the superconductivity is suppressed by a magnetic field [106, 107].Recent study of the electrical resistivity and YBCO have indicated metallic ($d\rho/dT > 0$) behaviors at high temperatures even down to the extremely light doping limit ($y \sim 6.23$), where the electrical resistivity shows localization signatures of low temperatures [108].

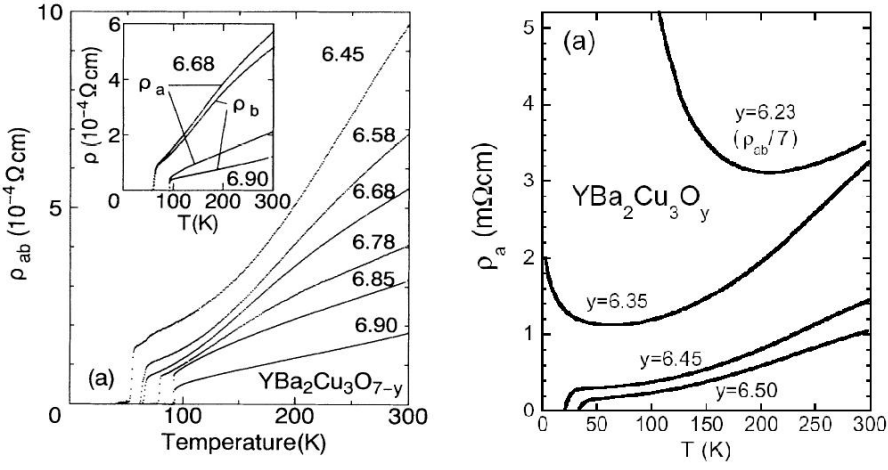

Figure 2.11: Temperature dependence of the in-plane resistivity for various doping concentrations in YBCO [108][109].

3.2.4 Pseudogap behavior

A lot of research has been done on the pseudogap region but there is not full agreement in the interpretation of the different experiments. One scenario suggests that the pseudogap is closely related to the superconducting gap and its onset temperature, T∗, will merge with the superconducting transition temperature Tc in the overdoped region. In this picture, the Cooper pairs are pre-formed at T∗, but due to large phase fluctuations the global superconducting state does not develop until at a temperature T_c where phase coherence is established. A clear evidence of the correlation between pseudogap and the superconducting gap was given by angle-resolved photoemission spectroscopy (ARPES) measurements [110, 111] showing that the symmetry of the pseudogap is the same as that of the superconducting state and the onset temperature T∗ approaches the superconducting transition temperature T_c at optimal doping. In addition, tunnelling spectroscopy [112] found the same scaling of both the pseudogap and the superconducting gap as the doping was changed showing a final merging of T∗ with Tc on the overdoped side.

In the second scenario the pseudogap state is considered an independent state or even as a state competing with the superconducting state. In this picture, T_{pair}

intersects the superconducting dome and drops to zero at a quantum critical point inside the dome as is shown in dash in Figure 2.10.

Experiment supporting this scenario found two different energy gaps in k-space, one in the nodal region at the Fermi surface corresponding to the superconducting gap and the other one in the antinodal regions due to the pseudogap [113–116]. As the doping decreases in the underdoped region it was found that the superconducting gap scales with T_c while the pseudogap increases significantly. In addition, this proposed model usually involves one or more distinct ordering phenomena such as charge density waves (CDWs), spin density waves (SDWs) or orbital current order [117, 118]. This scenario has also been supported by experimental results obtained with a variety of techniques including neutron scattering [119, 120], scanning tunnelling microscopy (STM) [121, 122] and Nernst effect measurements [123, 124].

Even though the nature of both scenarios is different, several theories combined both interpretations suggesting the existence of two pseudogaps: one opening up at a high temperature, $T*$, and the other opening at a lower temperature, T_{pair} [125, 126].

3.2.5 Quantum phase transition

An important are of research in the last years has been the study of the quantum critical points (QCPs) that might be present in the phase diagram of the cuprates (Figure 2.10) depending on the two possible scenarios described before in the pseudogap section. Assuming the second scenario, it has been predicted that the superconducting-insulator transition can be regarded as a quantum critical point, assuming that there is no gap between AF insulating state and the superconducting state at zero temperature although at high temperature there is a pseudogap state [127]. This quantum phase transition has been widely studied and it is believed it may be induced by varying a parameter of the Hamiltonian of the system [128, 129]. Possible parameters include film thickness [130, 131], magnetic field [132–134], carrier concentration [135], etc. A distinct feature of QPTs is the success of finite size scaling analysis of electrical transport data. In this context, different experiments have been recently carried out to identify this quantum critical points in YBCO [16, 19].

5 The Control of Carrier Density: Field Effect Transistors

The possibility to modify the physical properties of condensed matter systems by controlling the charge carrier density has become a crucial phenomenon in optimization the condensed matter based devices contributing to the revolution of the semiconductor industry.

The fast development of the semiconductor industry for electronic applications has enable cheaper and cheaper computers as well as more and more devices for broader ranges of applications [136]. Over years a mayor goal has been modify the carrier density to induce new states of the matter. As shown in Figure 2.12 apart from the semiconductors there are different families of new materials whose physical properties are to large extent determined by the carrier concentration. By varying the level of carrier concentrations new states of the matter can be induced by changing from the insulator state, to metals, or superconductors [2].

Different methods have been used to dope a solid material in order to modulate the charge carrier density.

On the one hand, chemical doping, is a direct, permanent and easy method. It can be substitutional (requires the replacement of one atom within the unit cell, for another one of different type) or interstitial doping, just adding atoms in an existing lattice unit, but not on the lattice sites [137]. However, this type of doping may introduce inevitable changes in the crystal structure and usually encompasses introducing chemical disorder, giving rise to a complex system in the physical properties of the doped material. On the other hand, there is electrostatic doping as in a field effect transistor (FET). This method uses and electric field to induce carrier density by charge accumulation or depletion at the material's surface and it is reversible, as long as electric field in FETs can be turned on and off, what makes from this novel device a unique tool to control carrier density without chemical or structural disorder [138].

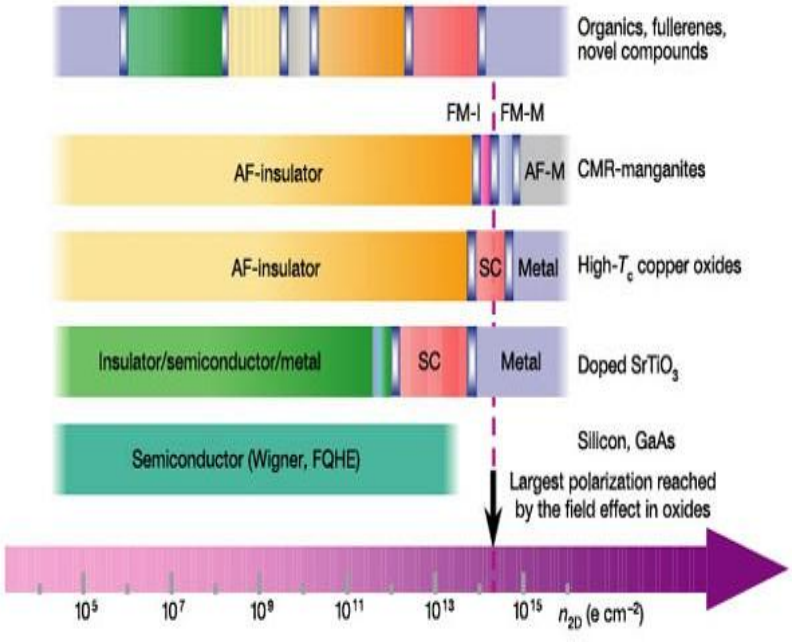

Figure 2.12 Phase diagram (at T=0) as function of the carrier density (2D). The silicon is shown as a reference. Superconductivity can be obtained from insulator state by introducing excess (free) charge of electrons (or holes) in many materials such as $SrTiO_3$, and high Tc copper oxides. The phases represented are AF, antiferromagnetic; FM, ferromagnetic; I, insulator; M, metal; SC, superconductor, FQHE, fractional quantum hall effect; Wigner crystal Adapted from Ref. [2].

The field effect transistor was first patented by Julius Edgar Lilienfeld [139].The patent was entitled “Method and Apparatus for Controlling Electric Currents”. In it, he proposed three-electrode amplifying device based on the semiconducting properties of copper sulfide. Though the principle of field effect transistors was first patented by Lilienfeld in 1926 and Oskar Heil in 1934, the practical semi-conducting devices such as the junction gate field effect transistor (JFET) were developed years later after the transistor effect was observed, explained and demonstrated by William Shockley and his team at Bell Labs in the year 1947. Shockley’s effort on commercializing the transistor was a path breaking contribution in the scientific society. However, the transistors that are currently employed in electrical devices are all, metal oxide semiconductor field effect transistors (MOSFETS) that were first proposed by Dawon Kahng in 1960 and this

transistor largely superseded the JFET and had a much more profound effect on electronic development.

4.1 Operation Mechanism of MOSfets

Nowadays semiconductor FETs are the basis and workhorse of many modern electronics. An external applied electric field (applied through an insulator o dielectric) is able to attract or repel charges, creating an accumulation or depletion of charge in the surface of the semiconductor, changing the electrical conductivity between two electrodes, the source (S) and the drain(D), and creating a current flow. The third electrode, at the top of the dielectric layer is called gate (G) and allows to switch the device 'ON' or 'OFF' when a particular gate voltage is applied to it.

The characteristic width of the accumulation and depletion layer form in the surface, is the so called screening length λ_e, that in the semiclasical limit correspond to the Tomas-Fermi screening distance. Systems with low carrier density, like semiconductors, have larger λ_e, and therefore it is possible to observe the field-effect. That is the reason to use semiconductor materials in those devices, instead of metallic ones, where λ_e is really small.

The challenge of increasing the charge carrier density in the semiconductor surface can be encompassed following two different directions. A key aspect is the geometric scaling of the channel length which allows performance improvement at the circuit level while keeping power dissipation manageable. However, as the size of a single FET shrinks to the nanometer dimensions, it has become more and more difficult to reliably control the channel region conductance by the gate due to leakage currents. Another approach is to induce high electric fields, which will also increase the carrier accumulation. It has been possible to reduce the operating voltages, keeping high electric fields, what has required high-K dielectric gate oxides to reduce leakage currents. However, when the electric field reaches values as high as $1{\cdot}10$ $MVcm^{-1}$, occurs the electrical breakdown of the insulator of the gate, which correspond approximately to a carrier concentration of $n_{2D}=1{\cdot}10^{13}cm^{-2}$ [57, 140] being impossible to go to high carrier accumulation using this kind of FETs.

A schematic diagram of a conventional FET is shown in Figure 2.13.

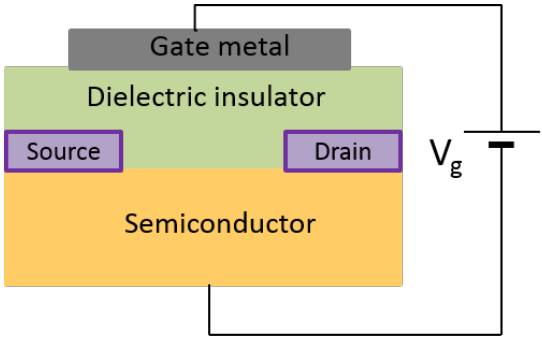

Figure 2.13. Schematic diagram of a typical semiconductor FET. The source and drains are metal electrodes for electron flows and controlled by the top electrodes called the gate, separated by an insulating layer of oxides.

Some relevant concepts of the operation of modern FETs [136] can be explained considering the metal-oxide-semiconductor (MOS) capacitor model. A MOS capacitor is a two-terminal device that is in essence the central part of MOS-FETs. Figure 2.14 shows the energy band structure of a MOS capacitor, with metal on the left and the semiconductor on the right side separated by a thin oxide (insulator) layer between them. The energy band diagram provides a wealth of information including carrier concentration, electric filed, and other parameters as function of position. Here all the energy levels are measured from the vacuum state and Φ_m represents the work function of the metal electrodes. The symbols E_c, E_F, E_v, and E_i represent the energy levels of the conduction band, the Fermi level, the valence band, and the middle line of the energy gap respectively.

In Figure 2.14 the center panel correspond to the case where there is not bias voltage applied between the metal and semiconductor, $V_g = 0$, showing the flat band diagram of the semiconductor. In the presence of a negative gate voltage ($V_g < 0$), the metal Fermi level F_m is pushed up by $|qV_g|$, where q is the charge of an electron. An electric field is created in both the insulating and semiconducting regions due to the voltage gradient and hence it induces a *band-bending* effect that brings the valence band closer to the Fermi level as illustrated on the left panel of Figure 2.14. Therefore, the hole concentration Qp must be raised above its equilibrium value within the system inducing on the semiconductor surface a net

positive (free) charge. These induced free holes are controlled by the gate electrode and will allow the semiconductor to carry current (ON state).

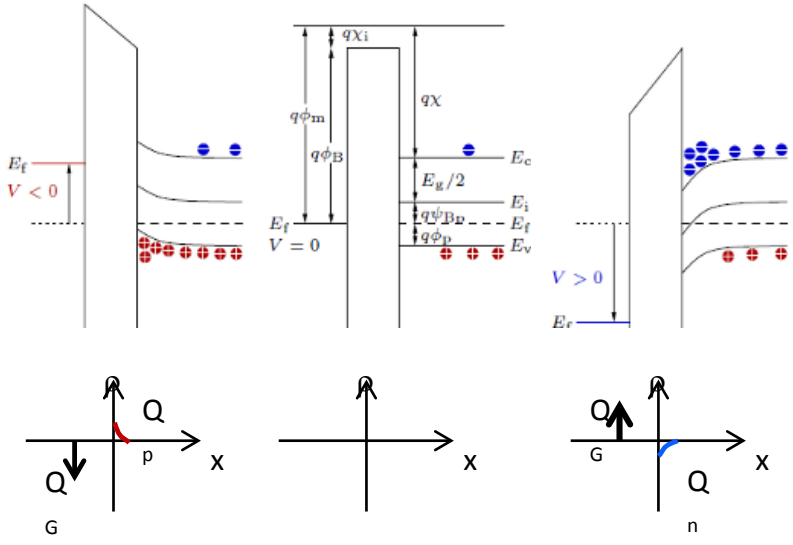

Figure 2.14. Band diagram of MOS capacitor with $V_g = 0$ (center), $V_g < 0$ (left) and $V_g > 0$ (right). Negative gating ($V_g < 0$) induces free holes Q_p in valence band and accumulated near the surface whereas positive gating ($V_g > 0$) introduces free electrons Q_n in the conduction band.

Conversely when a positive gate voltage is applied on the metal side ($V_g > 0$) the metal Fermi level is pushed down by $|qV_g|$, and the energy band bends down in the semiconductor. As the gate voltage is increased, the *band-bending* in the semiconductor increases, and the conduction band is steadily brought closer to the Fermi level. Thus the (free) electron concentration Q_n increases. In the right panel of the figure 2.14 is illustrated such energy bending by a positive gate voltage ($V_g > 0$) inducing free electrons onto the surface of the semiconductor, enabling free current flow in the system.

The total charge transfer per unit area, Q_{2D}, in a FET device can be calculated using the parallel-plate capacitor equation given by

$$Q_{2D} = C_{2D} \cdot V_g \qquad C_{2D} = \kappa \frac{\epsilon_0}{d} \tag{5}$$

Here C_{2D} is the areal capacitance (capacitance per unit area), κ is the dielectric constant of the insulator (dielectric material) between the gate electrode and the semiconductor, ϵ_0 is the free-space permittivity, and d is the thickness of the dielectric material used. While the choice of material for the gate dielectrics depends critically on cost, durability, operational speed, impedance and transconductance, the most important figure of merit for prospective gate dielectrics is the value of κ, which determines the quantity of free charge that can be induced in the semiconductor channels of FETs at a given gate voltage.

The current flow I_{SD} between the source and the drain electrodes can be given by

$$I_{SD} = \frac{W}{L}\mu_{FET}C_{2D}\left[\left(V_g - V_{th}\right)V_{SD} - \frac{V_{SD}^2}{2}\right] \quad (6)$$

where W is the width of the semiconductor channel, L is the channel length, μ_{FET} is the channel carrier mobility called the FET mobility, C_{2D} is the areal capacitance density associated with the gate dielectric, V_g and V_{SD} are the voltages applied to the device gate and drain electrodes respectively. V_{th} is a threshold voltage, that is the minimum value of the V_g when the conducting channel just begins to connect the source and drain contacts of the transistor, allowing significant current I_{SD} to flow. In this equation, I_{SD} is approximately proportional to the average charge across the channel and the average electric field along the channel direction. For low applied fields, I_{SD} increases linearly with V_{SD} and then eventually saturates to a state of constant I_{SD} values regardless of V_{SD}, which is known as 'pinch-off'. The derivation of the equation (6) assumes the gradual channel approximation, which neglects the lateral components of the electric field within the channel. So the current only flows between the source and drain, but not laterally (side-ways)[136].

The channel/gate interface properties such as interface states are crucial in the operation of conventional MOSFET. Several efforts are on-going to critically evaluate prospects of alternate approaches for realizing the next generation switching devices for information processing.

Utilizing phase transitions in correlated oxides is another approach to explore switching action under gate bias in three-terminal geometry. Their complex electronic phase diagram coupled with the carrier densities leads to a dramatic

modulation of the material resistance compared with conventional FET. The subthreshold swing could potentially be smaller because of the enhanced conductance modulation. What is more, the phase transition could also give rise to new functionality that is not expected from conventional FETs. For example, carrier-mediated ferromagnetic or antiferromagnetic phases might be interesting for magnetic logic.

4.2 Field-Effect Switching in Correlated Insulators: Mott FETs

In Mott FET, interfacial properties could be of even greater importance and complexity because the rich phases of Mott insulators coupled with their electron density. It is important to understand what happens when the gate dielectric (often a band insulator) and the Mott insulating channel are brought into contact. This is a non-trivial problem. The different work function will create an electron redistribution building up a potential at the dielectric/channel interface. The carriers transferred to Mott insulators may induce a change in the electric structure or a phase transition in the channel [28, 29].

Figure 2.15(a) shows schematic structure of proposed Mott field-effect transistor (Mott FET). Unlike conventional MOSFET devices with n-p-n or p-n-p doping in source, channel and drain area, Mott field-effect transistors could be fabricated on a homogeneous material without spatially varying dopant profiles.

The operation of Mott-FET is based on electrostatic control of carrier densities in the channel area with the aim of inducing electronic phase transitions of Mott insulators [41]. A Mott type insulator to metal transition triggered by the electrostatic modification of charge density will yield large changes in the channel conductance when the device is turned ON at the threshold voltage.

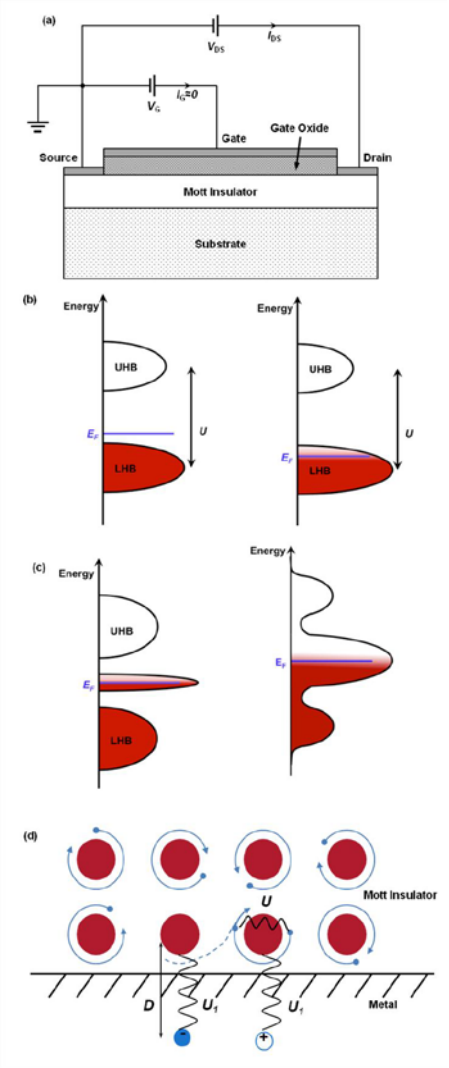

Figure 2.15 (a) Schematics of the proposed Mott field-effect transistor. Channel, source and drain are fabricated from a uniformly doped/undoped Mott insulator. A gate insulator could inject electrons/holes into the channel. When the injected carrier density is large enough to induce an insulator to metal transition, there is an increase in the source-drain current. (b)-(c) How the carrier density changes with surface potential in correlated systems is crucial to understand the subthreshold behavior of Mott FET. The evolution of band structure upon doping is not well understood in these systems and two possible ways are shown. (b) Fermi level is fixed while 'mid-gap' states developed upon doping. (c) A spectral weight transfer happens accompanied by a shift in the chemical potential upon doping. The transferred weight is directly proportional to the doped carrier density. (d) When a

Mott insulator is brought into contact with a metal, the hopping of electrons from one site to another will create image charges in the metal. The attraction between net charges in Mott insulator and image charges in the metal could lead to a decrease in the total hopping energy cost and effectively reduce the Hubbard *U*. From reference [141].

In the OFF state, the density of states is zero around the Fermi level of the Mott insulator, while it becomes finite in the ON state above threshold voltage. However, it is not very well understood how the band structures or the density of states evolves with the varying doping concentrations and two possible ways have been proposed to explain gating of Mott insulators.

In the first one, as shown in Figure 2.15(b), a finite density of states, called "midgap states" [142], is developed at the Fermi level while the Fermi level remains fixed [143]. In the second way a spectral weight transfer from lower (upper) Hubbard band to upper (lower) Hubbard band has been proposed due to a chemical potential shifts towards conduction (valence) band upon electron (hole) doping as shown in Figure 2.15(c) [144]. This spectral weight transfer could be understood as summarized S. Ramanathan [141] with the following picture: considering an undoped half-filled Mott insulator composed of N sites and one electron per site, when we dope the material with m holes, the number of singly occupied states becomes N-m. There are now N-m ways to add an electron to make a doubly occupied site, and therefore the total density of states of upper Hubbard band (related to the doubly occupied states) would be N-m. On the other hand, the total density of states of lower Hubbard band becomes N+m, because 2m states from the m unoccupied sites now have the energy scales of lower Hubbard band and contributes to the density of states. On the contrary, in a normal semiconductor, the conduction band and valence band is rigid against doping and thus the total density of states of each band does not change. The spectral weight transfer phenomenon in correlated electron systems is distinct from uncorrelated systems [74, 75] and therefore is an experimental signature of electron correlation [145–147].

As a result, electrostatic doping using a Mott insulator FET structure promotes to study strongly correlated electron systems and emerges as a powerful tool to understand the doping mechanism without introducing disorder. A summary of the most important discoveries regarding Mott-FET devices following Ramanathan [141] is reported below.

The first researches on electric field-induced switching in correlated insulators was done on VO_2 around 1970 [148–151]. The phenomena was associated with a thermally provoked process and it was not until the 1980 when subsequent authors [152, 153] claim to find experimental data inconsistent with a simple thermal model. These authors report that threshold power needed to obtain VO_2's conducting state was independent of the ambient device temperature in the range between 220 K and 320 K. In addition, they postulate that either channel inhomogeneities or an additional electronic effect were essential to explain tendency. Roughly at the same time a discussion regarding threshold switching in amorphous chalcogenide semiconducting films [154] was taken place. Researcher's assumptions were divided looking for an explanation either by an inhomogeneous thermal mechanism [155] or by an electronic mechanism [156] that involves injection of charge carriers from the electrodes which then fill all the available trapping sites. The controversy was never solved definitely, and the interest in the phenomenon decreased during the later 1980's and 1990's.

In 2000, the work on electric field-induced switching in VO_2 reemerged and a report [157] based on the speed of the process confirmed its Mott-Hubbard origin. These authors reported that at sufficiently large driving voltage, the VO_2 can switch in 1.5 ns, whereas the simple thermal model was predicting a much slower process 900 ns. Concurrently, electrical switching experiments in other materials started to appear in literature, including V_2O_3[158], $Pr_{1-x}Ca_xMnO_3$[159], $La_{2-x}Sr_xNiO_4$[160], and Sr_nCuO_{n+1}[161]. These reports were then succeed by many research studies on VO_2 [162–166] that claimed to corroborate the electronic nature of the voltage-induced switching. Recently the phenomenon has been reported in the metal-insulator transition material Fe_3O_4 as well[167]. Nearly all of these studies, however, disregard the possibility of both channel inhomogeneities and feedback effects. Indeed, a more recent calculation [168]of switching times in microscale, single-crystal VO_2 devices has found that nanosecond-scale switching times are possible solely due of thermal effects, once self-accelerating effects are taken into account.

From the theoretical point of view, recently the phenomenon of electric field-induced breakdowns in Mott insulators has attracted the attention of the scientific community. It is thought that in a strong enough electric field, electrons localized within a correlated insulator can tunnel across an energy barrier to doubly occupy

a nearby site[169–171]. The required Coulomb repulsion energy for this double occupation is gained directly from the electric field. In this model due to the generation of mobile electrons and holes within the system, it has been proposed at a sufficient density, a screening of the intersite Coulomb repulsion that cause an abrupt insulator-to-metal transition [172, 173]. Even though there is an agreement on the idea that a strong enough electric field should create dielectric breakdown in an ideal Mott insulator, it is still under debate the required strength of this field and the nonequilbrium charge transport dynamics that lead to the phase transformation.The required field strength is an important parameter to characterize the breakdown, the process will only be observable if a competing switching process does not occur first, as it happens with the ionic breakdown, Zener breakdown, and a thermally triggered MIT.

The discovery of a high-mobility two-dimensional electron gas at the interface between the transition metal oxides $SrTiO_3$ and LaAlO in 2004 [174] constitutes novel example of an electric field effect in a strongly correlated material. A full understanding of the system is still under discussion, but it is generally believed that an internal electric field, arising from a discontinuity in crystalline charge polarity, draws charges to the interface where they become mobile. In 2006 by applying a gate voltage, the conductivity of the electron gas was modulated through a quantum phase transition from an insulating to metallic state opening a full new trend of promising devices in epitaxial heterostructures grown from insulating oxides [175].

4.3 Electric Double Layer Transistors

The highest carrier density that conventional gate oxides are able to induce before dielectric breakdown (1-10 MV cm^{-1}) is around ~10^{13} cm^{-2},[176] which corresponds to ~10^{19}-10^{21} cm^{-3} bulk density when integrated over the screening length. This limit in the bulk density makes impossible to induce a phase transition in materials like high T_c cuprates. However, a new kind of transistors that uses an ionic liquid (IL) as the gate electrode instead of the dielectric is able to achieve a carrier density change of 10^{14}-10^{15} cm^{-2} what has allowed to explore the phase diagrams in a broader range opening the possibility to study phase transitions in a FET structure.

4.3.1 Ionic Liquids and Electrochemical Capacitors

Ionic liquid (IL) is an ionic compound typically a molten salt formed only by organic cations and inorganic anion and it does not contain any solvent, making it completely different form ionic solution. Any salt that melts without decomposing or vaporizing will usually yield an ionic liquid. There can be found liquefied or in glass state in the operation temperature of FET.

Those which are in a liquid state at room temperature are called room temperature ionic liquids (RTILs), and generally the use of the term ionic liquids (IL) usually refers to RTILs. The ionic nature of the liquid and its weak interactions between ions guarantee unique properties like very low vapor pressures, relatively small electronic conductivity and comparatively large ionic conductivity at room temperature. For the fact of being conducting fluids and powerful solvents, the ionic liquids have many important applications like storing energy when they are used as electrochemical capacitors.

Electrochemical capacitors, also called supercapacitors, store energy using ion adsorption by means of a static charge and are able to obtain a very high capacitance up to 500μF/cm^2 [177]. An electrochemical capacitor consists of two electrodes in an electrochemical cell (IL or a liquid electrolyte in some other applications). When a voltage is applied, charged ions in the IL will move towards to both electrodes according to their charge polarities creating a sub-nanometer gap capacitor at each electrode interface [178]. So, electrochemical capacitor can be described as two capacitors connected in series through an IL which forms two layers of opposite charges, called an *electric double layer* (EDL),. In Figure 2.16 a representation of an electrochemical capacitor using an IL as its dielectric is shown.

The term '*electrical double layer*' was first utilized by Hermann von Helmholtz [179] as shown in the Figure 2.17. In this work he assumed that no electron transfer reactions occur at the electrode and the solution. The net charges in the metal electrodes induced by the applied external potential (either positive or negative) are electrically screened with ions from the bulk IL being radius of the ion the limiting approaching distance. The overall result is two layers of opposite charge (the double layer) and a potential drop which is confined to only this region.

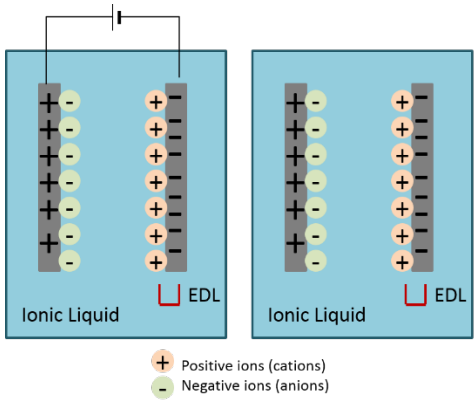

Figure 2.16 Electrochemical capacitor formed by placing two electrical conductors in an ionic liquid container and applying a voltage (left). An electric double layer (EDL) is formed between the metal surface and IL. Charge separation occurs at the solid-liquid interface of both electrodes and persists after the voltage source is removed (right image), which creates two capacitors in series across the IL.

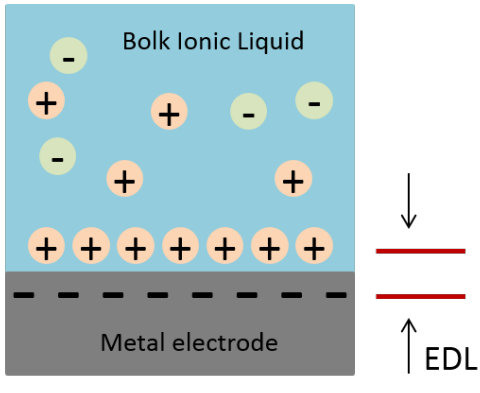

Figure 2.17 An electric double layer viewed by Helmholtz. The negative charges (electrons) in the metal electrode and the positive charges (cations) from the bulk IL form two layers of opposite charges at the interface, typically in the size of 1~2nm separation.

4.3.2 EDLT Gating mechanism

An EDLT works and operates the same way as a conventional FET, only with the difference of the IL as the gate dielectric. A typical structure of ionic liquid gated field effect transistor is shown in Figure 2.18. The channel surface, source and drain are covered by IL and a gate electrode isolated from channel is also in contact with IL. When a positive (negative) bias is applied to the gate electrode with respect to source/drain, cations (anions) will accumulate at the liquid/solid surface and correspondingly electrons (holes) will be electrostatically doped into the channel, forming the electric double layer (EDL). Therefore, the IL-gated FET is often referred to as electric double layer transistor (EDLT). The EDL is in the limit of high ion density and one can roughly estimate its areal capacitance from a simple formula only considering the Helmholtz layer:

$$\frac{1}{C} = \frac{d}{\varepsilon_{II}\varepsilon_0} + \frac{\lambda}{\varepsilon_{ch}\varepsilon_0} \tag{7}$$

where d is the spacing between cations and anions in the Helmholtz layer, which is typically a few nanometers, ε_{IL} is the dielectric constant of the ionic liquid, λ and ε_{Ch} are the screening length and dielectric constant of the channel material, respectively. The estimated capacitance is about 10 μF/cm^2 and would induce electric fields as high as 50 MV/cm [140]. Due to comparatively small Debye screening length in many Mott materials, the corresponding bulk density would be one order of magnitude higher than the values achievable by chemical doping [14]. Ultrahigh density carrier accumulation up to 8 x 10^{14} cm^{-2} at 220 K and 5.5 x 10^{14} cm^{-2} at 1.8 K has been reported by Hongtao Yuan *et al.*, in a ZnO field-effect transistor [10].

Just as in conventional solid gated FET, it is impossible to freely increase the large gate bias in IL gated FET. Electrochemical reactions would happen at a certain voltage and the electrochemical window (usually a few Volts, depending on the oxidization/reduction potential between ionic liquid and channel material) will limit the maximum gate voltage and hence maximum carrier accumulation in the device.

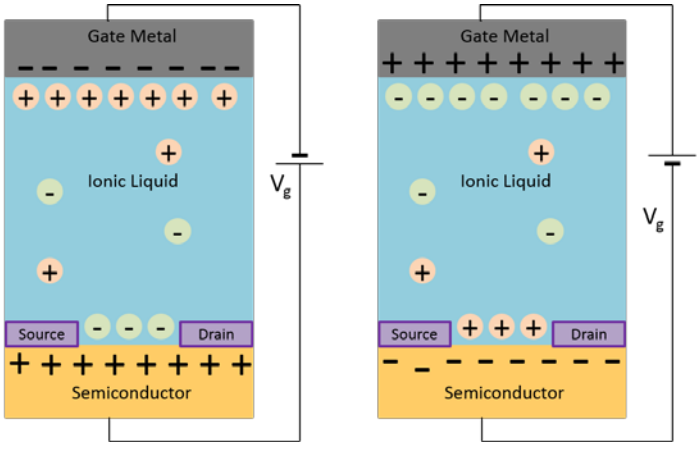

Figure 2.18 Schematic diagrams of the EDLT, showing the hole (left, p-type) and electron (right, n-type) accumulation in response to a gate voltage bias.

4.3.3 The Applications of Electric Double Layer Transistors

The possibility to achieve high levels of charge injection makes from the EDLT an unique and excellent technique for many areas of fundamental research [180]; such as superconductivity, ferromagnetism, ferroelectricity, spintronics, or the study of quantum phase transitions. Examples of discoveries of gate voltage-induced metallicity in ZnO[9], superconductivity in STO[12] and ZrNCl[13], and ferromagnetism in Co-doped TiO_2[11], prove the importance of this tool.

Gate voltage dependent sheet conductance and carrier density modulation was first achieved in a semiconducting amorphous InO_x channel at the beginning of 2007,obtaining resistance change of nearly 4 orders of magnitude in an EDLT device under different gate voltages [181].

In the same year, the group of Iwasa was able to modify ZnO thin films from the semiconducting into a metallic state [9]. Applying a positive bias and using an $KClO_4$/polyeltheleneoxide (PEO) electrolyte (ionic solution with smaller areal capacitance than ILs, but same functionality) an accumulation of electrons up to ~3×10^{13} cm^{-2} was deduced from the experiment. Similar temperature dependent resistance in ZnO were observed in later experiments (2009) using ionic liquid DEME-TFSI [10], achieving much higher density accumulation 4.5×10^{14} cm^{-2} and 5.5×10^{14} cm^{-2} at room temperature and down to 1.8K, respectively.

a) Superconductor-Insulator Transition (SIT)

The possibility to induce a superconductivity phase, just by applying and electric field was without doubt one of the most expected discoveries with a full range of broader applications in contemporary science and technology. Superconductor-insulator transition (SIT) is a key open question and has been studied intensively. Especially in the high-T_c superconducting cuprates, such as yttrium barium copper oxide (YBCO) and lanthanum copper oxide (LCO), the field effect is expected to be strong, since their low carrier density leads to larger electric-field penetration depths of a few nanometers.

One of the first reports of a SIT using the EDLT technique was published in 2008 by the group of Iwasa, reporting the electrostatic doping of a pristine strontium titanate (STO) single crystals. Using an $KClO_4$/PEO they were able to induce a two-dimensional superconducting state below a critical temperature T_c of 0.4 K [12]. Applying an external voltage up to 3.5 V the sheet carrier density was enhanced to 10^{14} cm^{-2}, comparable to the maximum value obtained for chemically doped bulk crystals, pointing this method as a promising route for the search for new superconducting materials**.**

Year later in 2009 the same group reported the observation of field-induced superconductivity using an EDLT configuration and an IL showing a transition temperature of Tc=15.2K on an atomically flat film of ZrNCl [13].

$KTaO_3$ FET gated by conventional oxide only shows insulator to metal transition. Due to the difficulty to chemically dope $KTaO_3$, no superconductivity was seen down to 10 mK and whether $KTaO_3$ could be doped into a superconductor remained unsettled [182]. By utilizing ionic liquid as gate electrolyte in EDLT, the accumulated electron density is around 10^{21} cm^{-3} (~ 1 order of magnitude larger than maximum chemical doping concentration) and superconductivity was observed in $KTaO_3$ by the group of Iwasa [14] in 2011. These results demonstrate the possibility of using FET structure to induce phase transitions in materials where chemical doping concentration is inadequate.

Bollinger *et al*. in 2011 also demonstrated SIT on lanthanum strontium copper oxide ($La_{2-x}Sr_xCuO_4$ or LSCO), a high T_c superconductor, using the EDLT technique [17].They recorded a nearly continuous modulation of the carrier density

measuring many curves of resistance versus temperature giving rise to a reported change of the critical temperature up to 30 K. Furthermore, the curves seem to collapse onto a single functional form, as expected for a direct two dimensional SIT using a finite size scaling analysis. They reported the critical resistance to be precisely the quantum resistance for electron pairs $h/4e^2$, suggestive of a phase transition driven by quantum phase fluctuations, and Cooper pair (de)localization.

In the same year, Xiang Leng *et al.* also reported a carrier-driven SIT transition using an EDLT of the high T_c superconductor $YBa_2Cu_3O_{7-x}$ (YBCO) [16]. Resistance versus temperature measurements were done to study the evolution from superconductor to insulator state in ultrathin films. Using a finite size scaling analysis, the curves were found to collapse onto a single scaling function, suggesting the presence of a quantum critical point.

b) Metal-Insulator Transitions

Several experiments have been carried out with the EDLT in order to broadly study the electrostatic control of metal-to-insulator transitions (MIT) with a modulation of carrier concentrations using EDLTs.

Menyoung Lee *et al.* have reported low-temperature, high-field magneto-transport measurements of $SrTiO_3$ gated by an ion gel electrolyte [183]. Metallic states of undoped STO were induced and it was observed a saturating resistance upturn and negative magnetoresistance that signal the emergence of Kondo effect as function of the applied voltage. The temperature-carrier density phase diagram has been determined by conducting Hall measurements under a series of gate voltages in undoped $SrTiO_3$ at the group of A .M. Goldman [184]. A regime of the anomalous Hall effect has been obtained suggesting magnetic ordering that is reminiscent of effects associated with quantum critical behaviors in some complex compounds. The role of percolation in conductance of electrolyte-gated STO has been studied by the group of Parkin, differentiating two different transport regimes as a function of the voltage. At high carrier densities a percolative metallic state is induced in which, at low temperatures, clear signatures of a Kondo effect are observed. At lower carrier densities, the resistance diverges at low temperatures and can be described by a variable range hopping model. They postulate that this derives from nonpercolative transport due to inhomogeneous electric fields from imperfectly

ordered ions at the electrolyte-oxide and concluded that the effect of disorder resulting from imperfect order in IL cannot be neglected in these studies.

Furthermore one of the most studied materials in the vanadium oxide (VO_2). M. Nakano *et al.* have demonstrated EDLT operation with VO_2, with a thermally driven, first-order MIT at around a temperature of 340K, and found that electrostatic charging at a surface drives all the previously localized charge carriers in the bulk material into motion, leading to the emergence of a three-dimensional metallic ground state [185]. They claimed that these results demonstrate a conceptually new field-effect device, extending the concept of electric-field control to macroscopic phase control. [185, 186].

Considerable effort has been devoted to study the effect of electron and hole doping on the electronic properties of niquelates. In this context, the electrostatic approach has several advantages as it enables the material to be doped purely through reversible electrostatic accumulation Reversible electric-field control of the MI transition in $NdNiO_3$, a member of orthorhombic distorted perovskite structure rare earth nickelates $RNiO_3$ (R = rare earth), has been demonstrated using EDL configuration [187][188]. The transition temperatures T_{MI} are related to the radius of R atoms [189] which control the tilting of NiO_6 octahedral. The results indicate that the electrostatic doping behaves in a similar way as chemical doping in $NdNiO_3$.The metallic conductance is unaltered by electrostatic doping, which is similar to the results of chemical doping) [190][191], while the insulating resistance could be modulated by 3 orders of magnitude and down to metallic state with negative gate voltages. [188]. Furthermore, charge order effect observed in $NdNiO_3$ may be important for understanding the nature of insulating state as well as interpreting the field effect results, [192][193] because the gate-induced charges may distribute inhomogenously in charge ordered insulators.

(c) Further Applications: Spintronics

The word spintronics-short for spin electronics-was coined in the 1990s to describe emerging technology exploiting both the intrinsic spin of the electron and its associated magnetic moment, in addition to its fundamental electronic charge. Parkin discovered the fundamental underlying spintronics phenomena and made the spin valve reality. A “spin-polarized” electrical current composed of all the

electrons' spins oriented either "up" or "down depending on the magnetic orientation of the ferromagnetic layers. Recently special attention has been focused on aspects of spin-polarized electron injection from a ferromagnetic metal to a normal metal or a semiconductor. Right after, some reports of electric-field-induced ferromagnetism employing EDLTs are described, which results from the carrier mediated exchange interactions.

Yamada et al. demonstrated electric field induced ferromagnetism at room temperature in a magnetic oxide semiconductor, (Ti, Co)O_2, by means of electric double-layer gating with high-density electron accumulation greater than 10^{14} cm^{-2} [11]. By applying a gate voltage of only a few volts, a low-carrier paramagnetic state was transformed into a high-carrier ferromagnetic state, thereby revealing the considerable role of electron carriers in high-temperature ferromagnetism and demonstrating a route to room-temperature semiconductor spintronics.

Moreover, Shimamura *et al*. have studied the electric field effect on magnetic properties and Curie temperature of Co ultra-thin films. In their approach an electric field is applied to a cobalt thin film using an EDLT configuration [194] formed in a polymer film containing an ionic liquid. The change in the Curie temperature is about 100K, suggesting that the observed large modifications of magnetic properties can be attributed to the significant change in the Curie temperature, which is brought about by the large charge transfer due to the formation of an electric double layer at the interface.

To summarize, ionic liquid gated EDLTs have broken the bottleneck of the maximum accumulated carrier concentration limited by gate breakdown in conventional FET. They have proven to be promising candidates to be utilized to investigate electric field induced phenomena in a broad range of materials and probe correlated electron physics.

CHAPTER 3

Experimental techniques

This chapter gives an overview of the most relevant experimental techniques used during this thesis. A brief introduction of the growth systems and the different procedures to characterize the samples is given to explore the topology, the structural quality, the transport measurements and the electronic properties of the thin films, as well as its structure distribution in the real space with atomic resolution. In addition, a detail explanation of the X-ray absorption spectroscopy (XAS) technique is provided, the correct understanding of the physical mechanisms involved in the X-ray measurements is essential as well as the analysis tools used to extract the data presented in this thesis.

1 Thin film deposition: Sputtering system

Samples of YBCO and PBCO are grown using a high O_2 pressure sputtering system in the chamber shown in figure 3.1. This method is based on the ballistic impact of atoms against a substrate after being removed from a material source. The oxygen plays the role of the sputtering element and through the application of a high electric field a plasma is created at the material source so the accelerated ionized atoms remove material from the target. The ejected atoms impact against a substrate placed nearby in such a way that some of the ejected material is deposited on the surface of the substrate forming a thin film. In our case the substrates are placed on a heater plate below the targets. In the case of oxides, this process involves solid state chemical reactions of the elemental oxides, which requires high temperature, to allow surface diffusion, and high oxygen pressures to ensure the fully oxidization of the material.

Depending upon the target's electrical conductivity the electric field supply must have different specificities. For electrical conductors, a DC power supply is sufficient between the target (cathode) and the substrate holder to have a net flow

of ions toward the target guarantying the atomic ablation. However, to avoid positive charge accumulation on the target surface, for insulators a radiofrequency (RF) generator is needed (see Figure3.1), which consist on a AC signal added to the DC voltage; on the positive cycle, electrons are attracted to the cathode, creating a negative bias, on the negative cycle ion bombardment continues. By avoiding a constant negative voltage on the cathode, ion buildup is prevented for insulating targets.

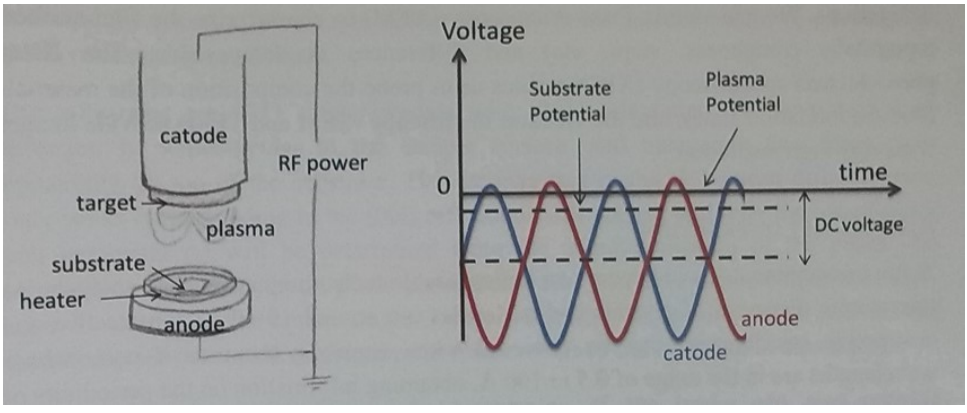

Figure 3.1 Sketch of sputtering system and voltage vs. time graph to show how the radiofrequency sputtering works.

The growth takes place inside a chamber in which a high vacuum of about 10^{-6} mbar is previously obtained. The chamber, shown in Figure 3.2, is connected to a turbo-molecular pump supported by a membrane pump. A constant oxygen flow is injected and controlled by a system of needle valves.

All the samples studied in this work have been grown on $SrTiO_3$ substrate (100)-oriented. The high oxygen pressure (3.4mbar) applied during the deposition, favors a complete thermalization of the extracted species and at the same time prevents them from back-sputtering and loss of oxygen in the final crystal structure. The substrate temperature during the growth process is kept at 900ºC. Under these conditions the deposition rate is 1nm/min and ensures the epitaxial growth of the sample. To preserve the optimal oxygen content of the structure an *in-situ*

annealing at 800 mbar O_2 pressure is necessary. The chamber is oxygenated at 600ºC and the annealing is made at 500ºC during 5 minutes.

Figure 3.2. View of the sputtering chamber. The targets are mounted on a remote controlled arm to switch between the different materials.

Amorphous Al_2O_3 have been grown to define the device pattern in a DC magnetron sputtering which has been bought, built up, and assembled during this PHD project. The plasma is confined close to the target by the magnetron, which is formed of two concentric magnets that create a magnetic field whose lines close in on the target. By the Lorentz force, the electrons are forced to a helicoidal trajectory around the magnetic field lines, causing higher electron density close to the target. This results in an increases of the ionizations of the gas atoms and so more collisions with the target, thus enhancing the sputtering deposition process. This system shown in figure 3.3 has been prepared to sputter non epitaxial metals and insulators at room temperature. Targets of aluminum, titanium, silver, iron and graphite are available with Ar as sputtering gas. In particular, it has been used for deposition of amorphous aluminum oxide through reactive sputtering combing the reactive gas, O_2, with the inert Ar gas flow with different rates. Thus it is a combination of physical and chemical deposition. The reactive gas goes in to a chemical reaction with the sputtered atoms. If the sputtering rate is faster than the

chemical reaction rate, then the reaction will take place on the substrate. As more and more reactive gas is introduced into the system, target oxidation can occur. This leads to drastically reduced sputter yields and deposition rates. The oxidation is a runaway process. Beyond a critical gas pressure, it progresses rapidly. Best oxide films are obtained just below this critical point.

Figure 3.3. Magnetron sputtering system.

2 Structural characterization

X-ray reflectivity (XRR) and diffraction (XRD) patterns have become an indispensable technique to determine the thickness and the structural quality of our samples. XRR and XRD measurements have been carried out at CAI de Difracción de Rayos-X (UCM), with a Philips X'pert MRD diffractometer, using a Cu tube as X-ray source (λ_X= 0.15418nm) operating at 45kV and 40mA.

2.1 X ray diffraction (XRD)

Atomic layers in a crystal are separated by a distance d_{hkl} located in parallel (hkl) planes. Specular reflected X-rays will travel different distances due to this separation and will yield constructive interference if the difference in path is an

integer multiple of the X-ray wavelength. Thus the diffraction condition described by the Bragg law:

$$2d_{hkl}sin\theta = n\lambda_x \tag{3.1}$$

where θ is the incidence angle of the X-ray beam, λ_x is the wavelength of the incident radiation and n the diffraction peak order.

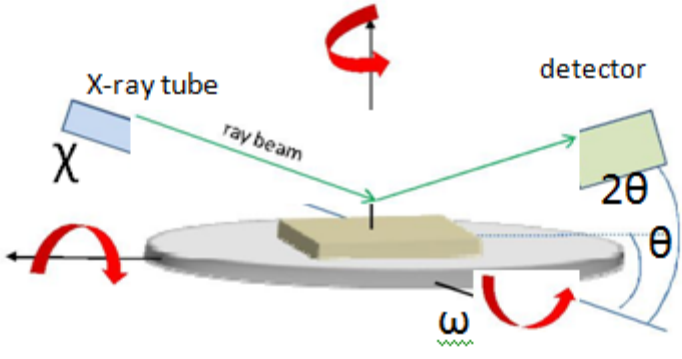

Figure 3.4: Schematic diagram of the θ-2θ geometry

For incident X-rays forming an angle θ with certain plane, the diffracted beam emerges forming an angle 2θ with respect to the incident beam. The diffraction scan carried out in θ-2θ geometry has the sample surface and the detector positioned at angles of θ and 2θ respectively from the incident X-ray beam (see figure 3.4)

The diffraction pattern shows the scattered intensity as a function of the angle θ, collected by rotating the sample holder and the point detector while conserving the θ-2θ relationship all the time. For epitaxial structure of different materials, a diffraction scan measured in θ-2θ geometry, after optimizing around one of the (00l) diffraction peaks of the substrate will show only the Bragg peaks of the same family [195]. Thus the equation 3.1 can be used for determine the lattice spacing of a set of crystallographic planes, parallel to the film plane, what has been usually called the lattice parameter c.

In case of multilayers the characteristic length scales are: the lattice spacing of the constituent material and the modulation wavelength Λ defined as the thickness of the bilayer that is repeated to form the superlattice. This additional periodicity will cause new diffraction peaks to appear which can be about the average lattice constant $\bar{d}$ following [196]:

$$2\frac{sin\,\theta}{\lambda_x} = \frac{1}{\bar{d}} \pm \frac{m}{\Lambda} \tag{3.2}$$

where m is an integer that labels the order of the satellite around the main Bragg peak and $\bar{d} = \Lambda/(N_A + N_B)$, where N_A and N_B are the number of atomic planes of material A and B in one bilayer.

2.2 X-ray reflectivity (XRR)

X-Rays are reflected at the interface between layers with different electronic densities at angles smaller than a critical angle. Using a coherent and collimated radiation to irradiate a thin film, the different refractive indexes (substrate, film and air) induce a change in the path length of the X-ray and consequently a constructive/destructive interference of the different reflected beams. In an analogous way, the interference resulting from a layered structure produces oscillation in the reflectivity pattern. This pattern is obtained by measuring the reflected intensity as a function of the incident angle θ through a detector in a θ-2θ geometry for very low incident angles.

Reflectivity scans show finite size oscillations (2θ <10º), related to the total thickness of the sample. The period of the finite size oscillations is inversely related to the thickness d of the whole sample. By indexing the position of the maxima and minima (n=1,2..) we can calculate the total thickness using:

$$sin\theta^2 = \left[\frac{(n-K)\lambda_x}{2d}\right]^2 + 2\delta \tag{3.2}$$

where k=0 correspond to a minimum and k=1/2 to a maximum, λ_x is the X-rays wavelenght and δ is the real part of the refraction index *n* given by:

$$n = 1 - \frac{\rho_n r_e \lambda_x}{2\pi}\left(f_0 + \Delta f' - i\Delta f''\right) = 1 - \delta + i\beta \qquad (3.3)$$

where ρ_n is the electronic density, r_e is the classical radius of the electron, f_0 is the atomic dispersion factor, $\Delta f'$and $\Delta f''$ are corrections due to the anomalous dispersion [197, 198]. The value of δ is in the order of 10^{-5} for complex oxides thin films.

3 Atomic Force Microscopy. Topography

Atomic force microscopy AFM is currently broadly employed to characterized sample surfaces (surface topography, phase, resistivity…). The measurements are performed at ambient temperature and pressure, thus not requiring special environmental conditions. Its resolution in the vertical direction is of the order of subnanometer, while the lateral is limited by the tip radius of curvature, in the order of few tens of nanometers.

AFM images of this thesis have been obtained with a Veeco multimode Scanning Probe Microscope equipped with Veeco RTESP tip at Microscopy Center of Complutense University.

AFM is based on a probe, constituted by a sharp tip at the end of a flexible cantilever. The tip has the height of the order of micrometers and a radius of curvature of generally 10-20 nm. Upon proximity to a surface, the cantilever reacts to the forces between the tip and the investigated surface, deflecting in first approximation according to Hooke's law. Various kinds of atomic forces are involved in such interaction, among which the Van der Waals force is the dominant one. By scanning the tip over the surface under investigation, the cantilever reacts to the topography of the sample. A feedback loop monitoring the cantilever's deflection keeps either the tip at a constant distance to the surface or the contact force constant (depending by the scanning mode employed) by moving the probe downwards or upwards. Such movement gives the topography of the scanned surface. The deflection of the cantilever is measured by the so-called optical lever mode. A laser light form a solid state diode is reflected off the back of the cantilever and collected by a photodetector. This consists of closely spaced photodiodes whose output signal is collected by a differential amplifier. Angular

displacement of cantilever results in one photodiode collecting more light than the other photodiode, producing an output signal. Therefore, the detector keeps track of the cantilever's deflection.

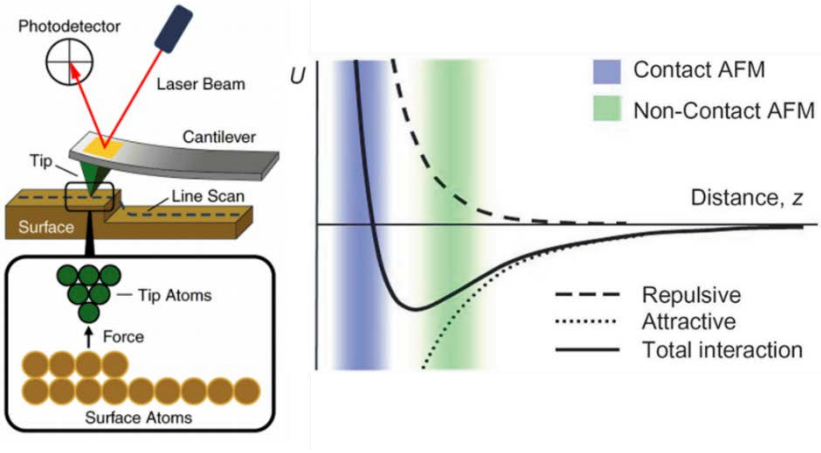

Figure 3.5. Sketch of sputtering of working principle of Atomic Force Microscopy, sketch of van del Waals Force dependence on tip-to-sample separation distance.

The distant dependence of the forces between tip and sample can be approximated by a Lennard-Jones potential. At short distances (<10Å) the force is repulsive, due to ionic charges in both materials. For bigger distances (from 10Å ~to 200 Å) the force changes of direction due to the predominance of Van der Waals attractive forces emerging from the nuclei electron clouds polarization. Based on the forces acting and on the distance between tip and surface one can define the typical modes of works of AFM:

Contact mode (also called static mode). In contact mode, the tip is "dragged" across the surface of the sample and the topography of the surface is measured either using the deflection of the cantilever directly or, more commonly, using the feedback signal required to keep the cantilever at a constant position. Close to the surface of the sample, attractive forces can be quite strong, causing the tip to "snap-in" to the surface. Thus, contact mode AFM is almost always done at a depth where the overall force is repulsive

Dynamic contact mode (also called intermittent contact or tapping). It is the most widely employed AFM mode for topography imaging. Approaching the tip probe at small distances of the sample while prevent it from sticking to the surface is a major problem to contact mode. In this method the tip oscillates at a frequency near the cantilever resonance frequency with amplitude ranging typically from 10 nm to 100nm. Variations in the tip-surface average distance make the oscillation amplitude to change. This vibration amplitude reduces when the tip approximates the sample surface due to repulsive forces. The feedback loop monitors the root mean square (RMS) of the oscillation, acquired by the photodetector and keeps it constant at the setpoint value by vertical movements of the scanner.

4 Scanning Transmission Electron Microscopy

A scanning transmission electron microscope (STEM) is a powerful technique to provide two-dimensional maps revealing atomic and electronic structure of complex oxide with sub-Ångstrom spatial resolution and sub-eV energy resolution. All the STEM measurements in this thesis were done at the Microscopy Center of Complutense University by Mariona Cabero and Maria Varela.

In the scanning-transmission electron microscope (see Figure 3.4), a field-emission source and strong electromagnetic lenses are used to form a small probe that can be raster-scanned across the sample [199]. Images are obtained serially as the probe is scanned pixel-by-pixel using a number of detectors with different geometries. The key advantage of STEM is the ability to detect multiple signals simultaneously.

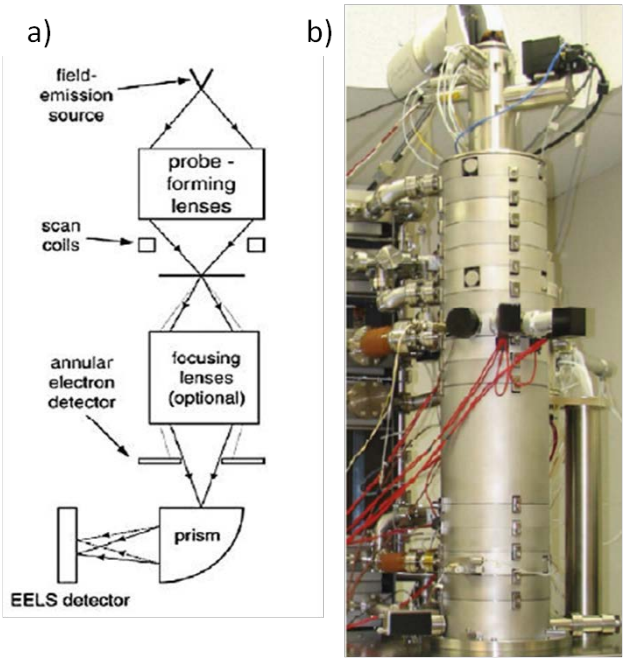

Figure 3.6. a) Schematic of a scanning-transmission electron microscopy system. From ref [199]**.** b) Photograph of a NION ULTRASTEM column [200].

The high angle annular dark field (HAADF) detector is normally used for Z-contrast imaging. A dark-field image, representing transmitted electrons scattered through relatively large angles, is formed by feeding the signal from a ring-shaped (annular) detector to a display device scanned in synchronism with the probe scan. Alternatively, the whole spectrum is read out at each probe position (pixel), resulting in a large spectrum-image data set that can be processed off-line [201]. The dark field image was collected over a wide range of scattering angles and showed strong atomic number contrast. The fact that the Z-contrast images are directly interpretable makes this technique very appealing. For higher collection efficiency a lower angle ADF detector can be used to improve signal-to-noise ratio.

Bright field image shows the usual characteristics of an interference or phase contrast image [202–204]. Light atoms scatter much less than heavy atoms and have usually been invisible in a Z-contrast image until aberration corrected. Recently an annular bright field mode has been shown to give less Z-contrast

image [205, 206]. The reduced Z dependence means light elements are easier to see in the image.

The Z- contrast image also enabled atomic resolution EELS [207, 208] by providing an unambiguous signal that allowed the probe to be located over a specific atomic column or plane. EELS is formally equivalent to X-ray absorption spectroscopy. Electrons scattered through smaller angles enter a single prism spectrometer, which produces an energy-loss spectrum (EELS spectrum) for a given position of the probe on the specimen [209]. With modern microscopes it is possible to obtain an EELS spectrum in each atomic column; this makes this technique a powerful tool to investigate the chemical composition of interfaces.

The high energy resolution of this technique also allows the study of the fine structure in the absorption edges which permits study electronic properties as oxidation state in transition metals. EELS edges are a result of the excitations of inner shell electrons into occupied levels above the Fermi level. Therefore, the EELS fine structure ensues directly as a result of the material's unoccupied density of states and they can be used to probe electronic properties when core electrons are excited. In complex oxides, properties such as the transition metal oxidation state can be measured from the EELS fine structure of the transition metal $L_{2,3}$ edge and the O K edge [210, 211].

5 Four-Point resistivity measurement

For our low temperature resistance measurements, we used a closed-cycle Cryophysics helium refrigerator which works with the expansion of highly-pure He-gas compressed in a Gifford McMahon cycle. The expansion through the capillaries undergoes two steps at 50K and at 8.5K. The sample is mounted onto a cooled copper piece in contact with the second cooling step. The system is evacuated by a rotary pump capable of a pressure down to 10mTorr, measured with a Pirani vacuum sensor. A silicon diode thermometer is in contact with the sample holder calibrated for measuring between 15 and 325K. The system is also equipped with a heater controlled by a Lake Shore 330-11 temperature controller which permits to control the sample's temperature between room temperature and

15K with 10-mK accuracy. Micro-coaxial wires connect the different parts for low noise measurements.

The resistance of thin layer was measured using the Van der Pauw four-point method [212] to eliminate any contribution given by the in-series contact resistance. Four electrical contacts were made on the surface of the sample by evaporation of silver and then connected to the low-noise wiring by indium.

The instruments used were a Keithley 2611 current source, capable of stabilizing a current supplied between 5nA and 100mA and a Keithley 2182A nanovoltimeter. For our low resistance measurements, we used the conventional method of reversing the current sign and averaging the voltage measurements $V = [V(I^+) - V(I^-)]/2$ in order to avoid the thermoelectric effect influence on the measured resistance.

6 Electrochemical impedance spectroscopy. Capacitance Measurements

Impedance spectroscopy (IS) measurements were mainly used to characterize liquid phase electrochemical cells, but its power to analyze resistive and capacitive properties of solid matter has opened broader areas of research during the last [213, 214].

Macroscopic bulk samples are most conveniently characterized by IS in a parallel-plate capacitor measurement geometry, where the measured resistance R and capacitance C allow a quick and easy characterization of the resistive and capacitive properties respectively of the different contributions arising from electronically distinct areas in the sample. The specific parameters of resistivity ρ and dielectric permittivity ε_r can be calculated readily by the well-known equations:

$$\rho = R\frac{A}{d} = R\ g; \quad \varepsilon_r = \frac{C}{\varepsilon_0}\frac{d}{A} = \frac{C}{\varepsilon_0 g}; \tag{3.4}$$

where A is the effective current cross section, d the electrode distance, g is the geometrical factor (g = A/d) that should be large enough to be under the consideration of plano-paralell condensator geometry, and ε_0 the dielectric permittivity of vacuum.

The standard frequency IS measurement consists effectively of an electric stimulus in terms of an alternating voltage signal *V* of sinus or cosine shape, with angular frequency ω and amplitude *Vo* applied to the sample. In this condition, an effectively the amplitude I_0 and phase shift δ of the current response signal *I* are measured. It is assumed that the dielectric response is linear, so the applied voltage and the current response signals have both the same shape and frequency but with a phase shift δ.

The impedance can therefore be defined as a time-independent complex number Z^* (= Z' + iZ''). The relationships of |Z| (modulus of the impedance), Z', Z'', V_0, I_0 and the phase angle δ can be expressed as:

$$|Z| = \frac{V_0}{I_o} = (z'^2 + z''^2)^{\frac{1}{2}}; \tag{3.5}$$

$$Z' = |Z|cos\delta; \;\; Z'' = |Z|sin\delta; \qquad \frac{Z''}{Z'} = tan\delta \tag{3.6}$$

In the simplest case, a liquid phase electrochemical cell is shown in Figure 3.7 for an IS experiment. It consists of a cell with two electrodes, one at the base and the other over the crystal window, connected to the impedance analyzer, in this case the 4192A Hewlett Packard Impedance Analyzer. The cell has been specially designed for ionic liquid measurements guarantying large high quality ε_r data due to its reduced capacitor distance, *d*, obtained in this particularly set up combining a window crystal pane and a series of screws that allow us to confine the IL in a 50μm distance. The sample may be placed in a cryostat or/and in a magnetic field for temperature dependent or/and magnetic field dependent measurements. Impedance spectroscopy data are usually reliable up to ≈ 1 MHz and usually unreliable above ≈ 10 MHz.

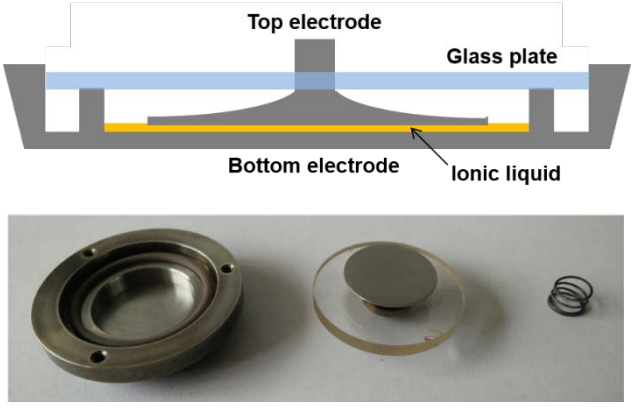

Figure 3.7 Electrochemical cells to measure the impedance spectroscopy designed for ionic liquid measurements that confine the IL in a 50µm distance capacitor.

From the measured parameters it is advantageous to obtain the real and imaginary parts of the impedance *Z*'-*Z*'', capacitance (*C*'-*C*'') or dielectric permittivity (ε'-ε''), the complex conductivity (σ'-σ''), and the imaginary part of the dielectric modulus (*M*''), which is the inverse of the permitivity. Plotting the data in different notations often gives access to additional information on the resistance and permittivity of a specific dielectric contribution. In a regular scenario, one dielectric contribution may originate from the extrinsic electrode – sample interface (electrode), and one from the intrinsic sample (ionic liquid).

$$\varepsilon^* = \frac{\sigma^*}{i\omega\varepsilon_0};\ \ \varepsilon' = \frac{\sigma''}{\omega\varepsilon_0};\ \ \varepsilon'' = \frac{\sigma'}{\omega\varepsilon_0}; \tag{3.7}$$

$$\sigma^* = i\omega\varepsilon_0\varepsilon^*;\ \ \sigma' = \omega\varepsilon_0\varepsilon'';\ \ \sigma' = \omega\varepsilon_0\varepsilon''; \tag{3.8}$$

$$M^* = \frac{1}{\varepsilon^*};\ M^* = \frac{i\omega\varepsilon_0}{\sigma^*}; \tag{3.9}$$

7 X-ray absorption spectroscopy (XAS)

The term XAFS (X-ray absorption fine structure) is currently used as a reference to the entire x-ray absorption region. XAFS give us information of how x-rays are

absorbed by an atom at energies near and above the core-level binding energies of the studied atom.

XAFS spectra are especially sensitive to different chemical and physical states of the atom and thus it provides a practical, and relatively simple, way to determine the formal oxidation state and local atomic structure for a selected atomic species.

In this thesis an important set of experiments and the key role measurements in this project have been done with the XAFS technique in a synchrotron. In this section the main fundamental principles of XAFS are described in detail below adapted from [215][216]. A fully description of how the data have been analyzed is also described.

7.1 XANES and EXFAS techniques

X-rays are ionizing radiation with energies ranging from ~ 500 eV to 500 keV, or wavelengths from ~25Å to 0.25Å and thus, by definition, have sufficient energy to eject a core electron from an atom, described by the well-known photoelectric effect. This phenomenon has been well understood for nearly a century and Einstein was awarded with the Nobel Prize for describing this effect. In this process, an X-ray photon is absorbed by an electron in a tightly bound quantum core level (such as the 1s or 2p level) of an atom with a particular binding energy, and a photo-electron with wave number k is created and propagates away from the atom.

When the X-ray energy is scanned through the binding energy of a core shell, there is an abrupt increase in absorption cross-section. This gives rise to a so-called absorption edge, with each edge representing a different core–electron binding energy as is shown in the Figure 3.8 [217, 218].The edges are named according to the principle quantum number of the electron that is excited: K for n ¼ 1, L for n ¼ 2, M for n ¼ 3, etc. The core–electron binding energy increases with increasing atomic number, ranging from 284 eV for the C K edge to 115,606 eV for the U K edge.

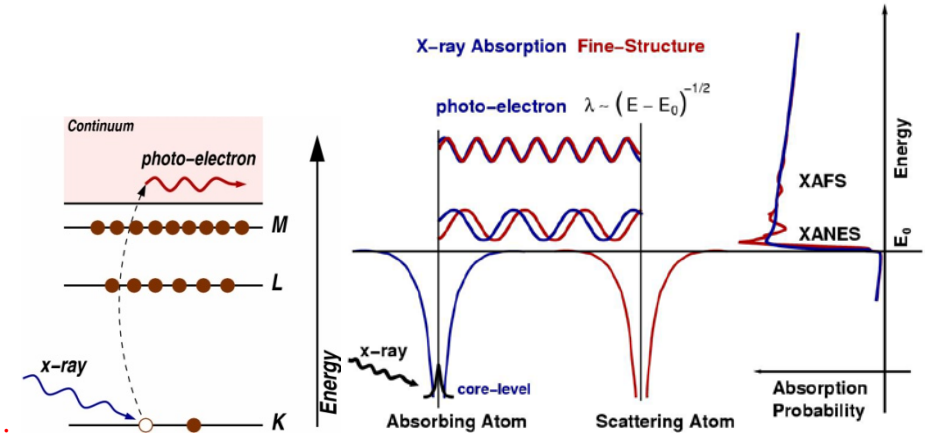

Figure 3.8: Sketch of x-ray absorption through the photoelectric process. The sharp rise, E_0, comes from the destruction of a tightly bound core-level and the creation of a photo-electron. XAFS occurs because the photo-electron can scatter from a neigh-boring atom modulating the amplitude of the photo-electron wave-function at the absorbing atom. From Ref [216].

The absorption edge is not simply a discontinuous increase in absorption, but in fact shows significant structure both in the immediate vicinity of the edge jump and well above the edge as suggested. The structure in the vicinity of the edge is sometimes referred to as X-ray absorption near-edge structure (XANES). The oscillations above the edge, which can extend for 1,000 eV or more, are often referred to as extended X-ray absorption fine structure (EXAFS). The distinction between XANES and EXAFS is arbitrary, since the same fundamental physical principles govern photoabsorption over the entire XAS region. Nevertheless, the difference between both terms remains with some justification, since the XANES and EXAFS regions are generally analyzed differently. As described in detail below, the XANES region is sensitive to formal oxidation state and coordination chemistry geometry (e.g., octahedral, tetrahedral coordination) of the absorbing atom, but is not, in most cases, analyzed quantitatively. The EXAFS region is sensitive to the radial distribution of electron density around the absorbing atom and is used for quantitative determination of bond length, coordination number and species of the neighbors of the absorbing atom.

The EXAFS region is typically taken as starting 20–30 eV above the edge jump. At these energies, the X-ray excited photoelectron has significant energy, and thus has a de Broglie wavelength that is comparable to the interatomic distances. The

EXAFS photoexcitation cross-section is modulated by the interference between the outgoing and the back-scattered photoelectron waves as illustrated schematically in Figure 3.9. At energy E_1, the outgoing and the back-scattered X-rays are in phase, resulting in constructive interference and a local maximum in the X-ray photoabsorption cross-section. At higher X-ray energy, the photoelectron has greater kinetic energy and thus a shorter wavelength, resulting in destructive interference and a local minimum in photoabsorption cross-section (energy E_2). The physical origin of EXAFS is thus electron scattering, and EXAFS can be thought of as a spectroscopically detected scattering method, rather than as a more conventional spectroscopy.

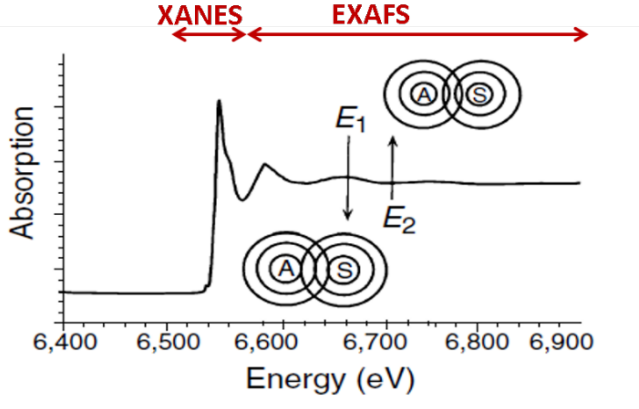

Figure 3.9 Sketch of the XAFS spectra, the photo-electron of the absorbing atom (A) is scattered by surrounding atoms (S). At energy E_1, the out-going and back-scattered waves are in phase, resulting in constructive interference and a local maximum in photoabsorption cross-section. At a slightly higher energy E_2 (shorter photoelectron wavelength) the absorber–scatterer distance gives destructive interference and a local minimum in absorbance. Ref[215].

7.1.1 Fluorescence and Auger mechanism

Absorption of an ionizing X-ray results in photoelectron ejection, leaving behind a highly excited core-hole state. There are two main mechanisms for the decay of the excited atomic state following an X-ray absorption event. In fluorescence (see Figure 3.10) a higher energy electron core-level electron fills the deeper core hole, ejecting an x-ray of well-defined energy. The fluorescence energies emitted in this way are characteristic of the atom, and can be used to identify the atoms in a

system, and to quantify their concentrations. For example, an L shell electron dropping into the K level gives the K_α fluorescence line.

The second process for de-excitation of the core hole is the Auger Effect, in which an electron drops from a higher electron level and a second electron is emitted into the continuum (and possibly even out of the sample). For lower-energy excitation, Auger emission can be the dominant relaxation process. For higher-energy excitation (e.g., for the K edges of elements with atomic numbers greater than 40), X-ray fluorescence is the primary relaxation process. For light elements, the X-ray fluorescence spectrum is quite simple. However, for heavy elements, a large number of X-ray emission lines are observed. The nomenclature associated with X-ray fluorescence lines predates a modern, quantum understanding of the origins of X-ray fluorescence and consequently there is not a simple relation-ship between the names of different emission lines and the origin of the line [219–221]. Like all emission spectroscopy, X-ray fluorescence is governed by a series of selection rules. Consequently, only certain transitions, referred to as ‘‘diagram lines,’’ are allowed. As with other spectroscopies, a variety of forbidden transitions (nondiagram lines) are also observed, and can yield important information. Each element has unique ‘‘characteristic’’ X-ray emission energies which are, in most cases, well resolved from neighboring emission lines [222, 223].

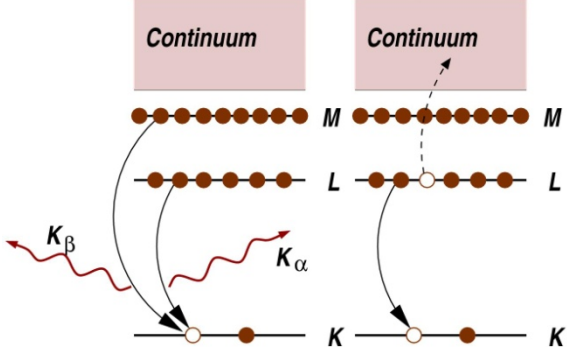

Figure 3.10: Decay of the excited state: x-ray fluorescence (left) and the Auger effect (right). In both cases, the probability of emission (x-ray or electron) is directly proportional to the absorption probability. Ref [216].

Either of these processes can be used to measure the absorption coefficient μ, though the use of fluorescence is somewhat more common. At most X-ray

energies, the absorption coefficient μ is a smooth function of energy, with a value that depends on the sample density ρ, the atomic number Z, atomic mass A, and the x-ray energy E roughly as

$$\mu \approx \frac{\rho Z^4}{AE^3} \tag{3.10}$$

The strong dependence of μ on both Z and E is a fundamental property of X-rays, and is the key to x-ray absorption Due to the Z^4 dependence, the absorption coefficient for O, Ca, Fe, and Pb are very different – spanning several orders of magnitude – so that good contrast between different materials can be achieved for nearly any sample thickness and concentrations by adjusting the x-ray energy.

7.2 XAFS Synchrotron Measurements

The development that allowed XAS to become a routine analytical tool was the recognition that the electron storage rings that are used in high-energy physics can serve as an extremely intense X-ray source. When an electron beam is accelerated, for example by using a magnetic field to cause the beam to follow the curvature of a storage ring, the electron beam radiates a broad spectrum of ‘‘synchrotron’’ radiation providing a full range of x-ray wavelengths. The spectral brightness of the most powerful sources is more than 10 orders of magnitude greater than that available from X-ray tubes. Another advantage of synchrotron sources is that the synchrotron X-ray beam is polarized, thus permitting orientation-dependent measurements for ordered samples.

A monochromator made from silicon is used to select a particular energy considering Bragg diffraction law. High energy resolution (1 eV at 10 keV), reproducibility, and stability are needed in the monochromator. A simple ion chamber [224] (a parallel plate capacitor filled with an inert gas, and with a high voltage across it through which the x-ray beam passes) is used as a detector to measure I_0 and the final intensity, I, in transmission mode (see Figure 3.13). However, to avoid the limitations of absorption, XAS spectra are frequently measured as fluorescence excitation spectra [225]. In most cases, the sample will emit a variety of X-rays, both the fluorescence X-rays of interest and a background of scattered X-rays. In order to have good sensitivity, the fluorescence detector needs some kind of energy resolution to distinguish between the signal and

background X-rays. This is typically obtained by an energy-resolving solid-state fluorescence detector [226].

In addition to X-ray fluorescence, properties that have been used include photoconductivity, optical luminescence, and electron yield, although only the latter is widely used. Electron yield detection of XAS is particularly important for studies of surfaces. Since the penetration depth of an electron through matter is quite small, electron yield can be used to make XAS measurements surface sensitive [227].

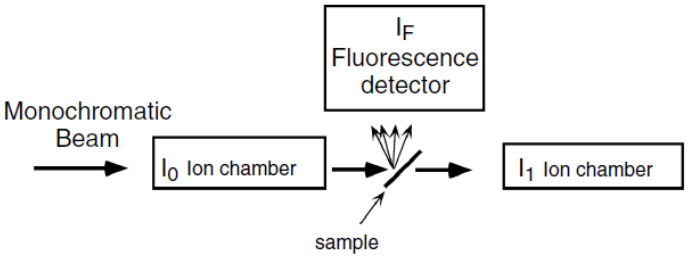

$$\mu_{transmision} = log\left(\frac{I_0}{I_1}\right) \quad \mu_{Fluorescence} \propto \left(\frac{I_F}{I_0}\right)$$

Figure 3.11 Typical experimental apparatus for XAS measurements. Incident and transmitted intensities are typically measured using an ion chamber; a variety of detectors can be used to measure

7.3 XANES Interpretation

Though the lack of a simple analytic expression, XANES interpretation can be described qualitatively in terms of coordination chemistry (regular, distorted octahedral, tetrahedral coordination), molecular orbitals (p−d orbital hybridization, crystal-field theory…), band-structure (the density of available electronic states), multiple-scattering (multiple bounces of the photo-electron), etc.

The heights and positions of pre-edge peaks are reliably used to empirically determine oxidation states and coordination chemistry as well as the shift of the peaks in energy. These approaches of assigning formal valence state based on edge

features make XANES a fingerprinting technique easier to interpret than EXAFS, even if a complete physical understanding of all spectral features is not available.

7.3.1 XANES to Oxidation State

XANES has been extremely useful in determining the oxidation state of the absorber. It is widely accepted that the energy of an edge increases as the oxidation state of the absorber increases [228]. An electrostatic model based on the requirement of a higher energy to eject a core electron in an atom with a higher charge, was proposed to explain it. An alternative interpretation of edge energies treats the edge features as ‘‘continuum resonances.’’. A continuum resonance involves excitation of a core electron into a high-energy state (above the continuum) that has a finite lifetime. An example is the potential well created by the absorbing and scattering (nearest neighbor) atoms. The absorber–scatterer distance gets shorter, the energy of the continuum state increases as $1/R^2$**.** Since higher-oxidation-state metals have shorter bond lengths, both models predict an increase in edge energetic with increasing oxidation state. Regardless of which explanation is most appropriate, the phenomenological correlation between edge energy and oxidation state is well established, and is widely used in coordination chemistry.

Empirically, the XANES region is quite sensitive to small variations in structure. Although there has been progress in the interpretation of XANES spectra [229], lot of work has been done looking for the agreement between calculated and observed spectra with the development of novel theoretical and computational methods permitting a detailer interpretation of XANES spectra .

7.3.2Bound State Transitions in XANES

For the K edge of a first row transition metal, the pre-edge transitions arise from bound state 1s→3d transitions, and are observed for every metal that has an open 3d shell. Although the 1s→3d transition is forbidden by dipole selection rules, it is never-theless observed due both to 3d + 4p mixing and to direct quadrupolar coupling. The sensitivity to 3d + 4p mixing means that the intensity of the 1s→3d transition can be used as a probe of geometry, with the intensity increasing as the site is progressively distorted from a centrosymmetric environment (i.e., octahedral < square–pyramidal < tetrahedral) or to distinguish between square–

planar (i.e., centrosymmetric) and tetrahedral sites. With careful analysis, the details of the 1s→3d transitions can be used to explore the electronic structure of the absorbing atom [215].

The analogous 1s→4d transition for second transition series metals is generally not observed. These edges occur at higher energy, where monochromator resolution is worse and core-hole lifetimes, which determine the intrinsic line width of a transition, are much shorter.[11] This results in broad edges for which the weak 1s→4d transitions are undetectable.

In addition to excitations into the 3d (or 4d) shells, XANES can also be used to probe higher-lying excited states. For atomic spectra, a complete series of ‘‘Rydberg’’ transitions can be seen [230]. For first transition series metals, the allowed 1s→4p transition is sometimes observed.

From studies of model compounds, it is found that the ‘‘1s→4p’’ transition is intense for square–planar complexes but weak for tetrahedral complexes, and can be used to deduce geometry. The greater intensity for square–planar complexes may be due to decreased mixing between the empty 4p orbital ($4p_z$) and the ligand orbitals. This intensity of the 1s→4p transition is even more dramatic for 2-coordinate Cu^{I} [231].

An alternative, complementary, approach to electronic structure information is to use ligand XANES rather than metal XANES. This is particularly promising as a tool for investigating oxygen ligands and has been used to quantitate the amount of metal–ligand orbital mixing (i.e., the covalency) of different complexes. Ligand XANES can be more useful than metal XANES due to the fact that the transitions of interest from a bonding perspective are 1s- 3p for O ligands and 1s-3d for a metal from the first transition series. The former is an allowed transition while the latter is forbidden by dipole selection rules, and consequently much weaker and harder to detect.

7.4 Theoretical Description of EXAFS Spectra

For the EXAFS, we are interested in the oscillations well above the absorption edge. For a single absorber–scatterer pair (for example, in a diatomic gas) this

alternating interference will give rise to sinusoidal oscillations in the absorption coefficient and we can be define the EXAFS fine-structure function $\chi(E)$ as

$$\chi(E) = \frac{\mu(E) - \mu_0(E)}{\mu_0(E)} \tag{3.13}$$

where μ(E) is the measured absorption coefficient, μ_0(E) is a smooth background function representing the absorption of an isolated atom, and μ_0 is the measured jump in the absorption μ(E) at the threshold energy E_0 (Fig 3.11 bottom).

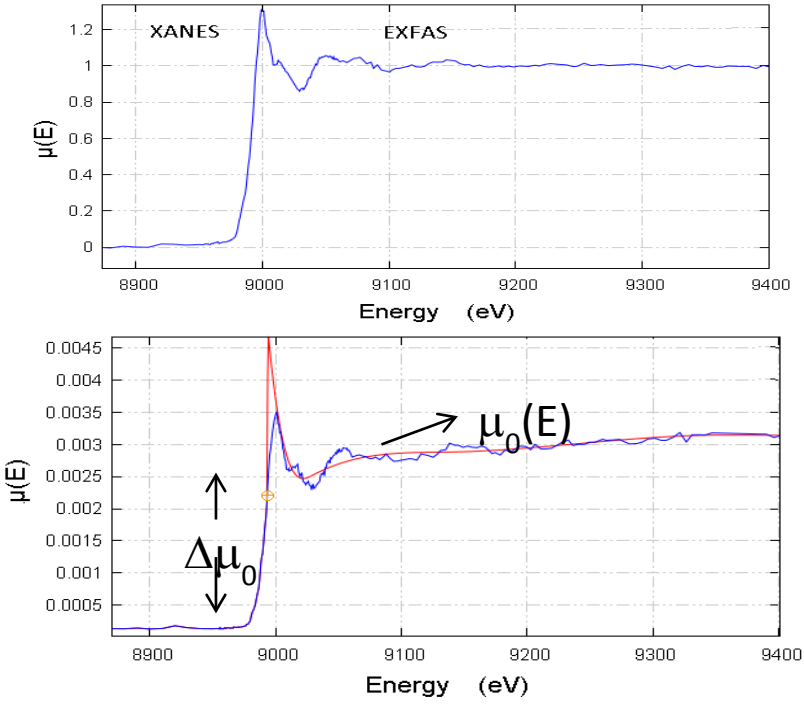

Figure 3.11: XAFS μ(E) for YBCO. On top, the measured XAFS spectrum is shown with the XANES and EXAFS regions identified. On the bottom, μ(E) is shown with smooth background function μ_0(E) and the edge-step $\mu_0(E_0)$.

As we will see below, EXAFS is best understood in terms of the wave behavior of the photo-electron created in the absorption process. Because of this, it is common to convert the x-ray energy to k, the wave number of the photo-electron, which has dimensions of 1/distance and is defined as

$$k = \sqrt{\frac{2m(E-E_0)}{\hbar^2}} \tag{3.14}$$

where E_0 is the absorption edge energy and m is the electron mass. The primary quantity for EXAFS is then χ(k), the oscillations as a function of photo-electron wave number, and χ(k) is often referred to simply as "the EXAFS".

In this way, the EXAFS extracted from the YBCO K-edge is shown in Figure 3.12 (top). As you can see, the EXAFS is oscillatory and decays quickly with k. To emphasize the oscillations, χ(k) is often multiplied by a power of k typically k^2 or k^3, as shown in Figure 3.12 (bottom).

The different frequencies apparent in the oscillations in χ(k) correspond to different near-neighbor coordination shells which can be described and modeled according to the EXAFS Equation,

$$\chi(k) = \sum_j \frac{N_j f_j(k) e^{-2k^2\sigma_j^2}}{kR_j^2} sin\left[2kR_j + \delta_j(k)\right] \tag{3.15}$$

where f(k) and δ(k) are scattering properties of the atoms neighboring the excited atom, N is the number of neighboring atoms, R is the distance to the neighboring atom, and σ^2 is the disorder in the neighbor distance being the exponential term the so called ''Debye–Waller'' factor. Though somewhat complicated, the EXAFS equation allows us to determine N, R, and σ^2 knowing the scattering amplitude f(k) and phase-shift δ(k). Furthermore, since these scattering factors depend on the Z of the neighboring atom, EXAFS is also sensitive to the atomic species of the neighboring atom. However, the EXAFS amplitude falls off as $1/R^2$ meaning that the XAFS information is limited to atoms in the near vicinity of the absorber.

For a full quantitative analyses, the EXAFS can be described considering also damping terms coming from inelastic loss processes, or the mean free path of the photoelectron $\left(\lambda(k)\right)$ [232–234] but here we won't enter into detail.

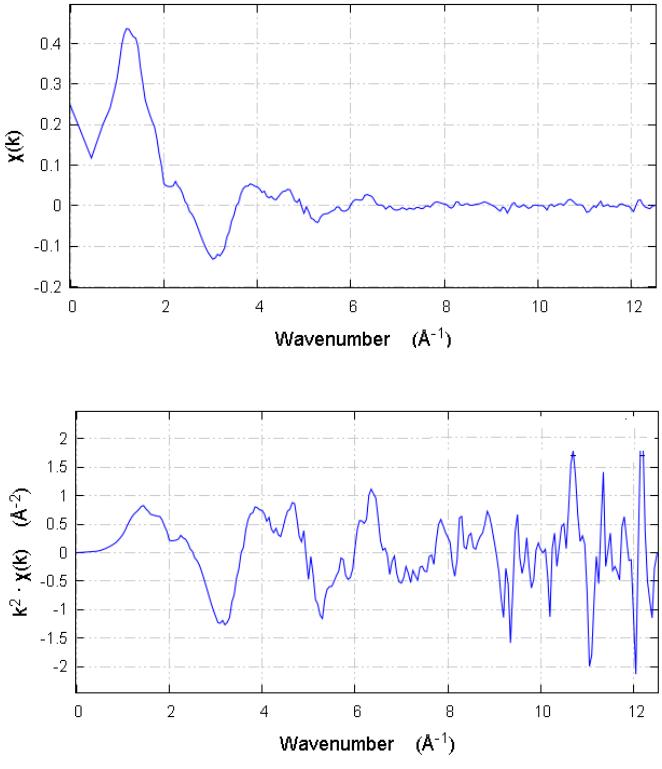

Figure 3.12: Isolated EXAFS χ(k) for YBCO (left), and the k-weighted XAFS, $k^2\chi(k)$ (right).

The discussion above assumed that the X-ray excited photoelectron was scattered only by a single scattering atom before returning to the absorbing atom. In fact, the X-ray excited photoelectron can be scattered by two (or more) atoms prior to returning to the absorbing atom. Multiple scattering is particularly important at low *k* and it is extremely angle dependent what means that EXAFS can, at least in principle, provide direct information about bond angles.

7.5 EXAFS data reduction

In this section, we'll outline the steps of raw data reduction:

- Convert measured intensities to μ(E), possibly correcting systematic measurement errors such as self-absorption effects and detector dead-time.

- Subtract a smooth pre-edge function from μ(E) to get rid of any instrumental background and absorption from other edges.
- Identify the threshold energy E_0, typically as the energy of the maximum derivative of μ(E).
- Normalize μ(E) to go from 0 to 1, so that it represents the absorption of 1 x-ray. The normalized spectra are useful for XANES analysis.
- Remove a smooth post-edge background function to approximate $\mu_0(E)$.
- Isolate the XAFS χ(k), where $k = \sqrt{\frac{2m(E-E_0)}{\hbar^2}}$
- k-weight the XAFS χ(k) and Fourier transform into R-space

Special care has to be taken removing the post-edge background spline function. The main point to keep in mind is that the function should not remove the XAFS itself, and needs to remove only the very low frequency components of.

The Fourier transform is critical to XAFS analysis. The Fourier Transform is a complex function it will be important to keep in mind that has both real and imaginary components when modeling.

CHAPTER 4

Characterization and device fabrication

1 Growth and characterization of thin films

The structural properties of thin films influence their physical properties. To ensure high quality and epitaxial growth it is important to control and determine the defect structure, crystallinity and the surface morphology. In the following section the optimal structural characterization for the thin films of YBCO, PBCO and amorphous alumina is presented, as well as a brief characterization of the IL that has been used in the EDLT.

1.1YBCO growing and characterization

All the YBCO samples studied in this work have been grown on $SrTiO_3$ substrate (100)-oriented. The pressure during the deposition was 3.4mbar at a growth temperature of 900ºC. The chamber is oxygenated at 600ºC and the annealing is made at 500ºC during 5 minutes at 800 mbar O_2 pressure. In Figure 4.1 resistance versus temperature has been measured for a thin film of 20nm showing the superconducting state at a critical temperature of 90K.

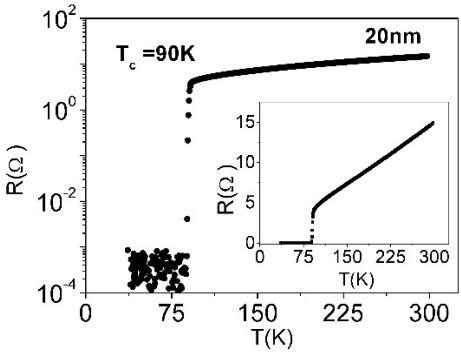

Figure 4.1 Resistance versus temperature curve of a thin film of 20nm YBCO grown by sputtering deposition.

Reflectivity and diffraction spectra for YBCO thin films indicate good structural properties showing flat and epitaxial growth. The thickness of the thin films is calculated from the finite size oscillations of the reflectivity spectra (Figure 4.2a). The first Bragg peak of YBCO observed at 2θ=7.57 allows us to determine the lattice parameter c=11.67 Å.The diffractograms at high angles show the diffraction peaks of both the thin film and the substrate labeled in Figure 4.2b).

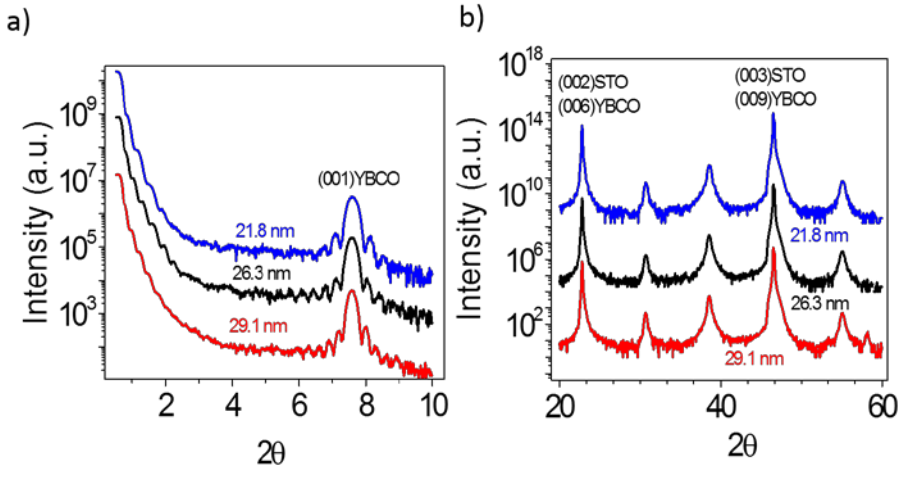

Figure 4.2. X-ray reflectivity and diffraction spectra of YBCO thin films grown for different thicknesses

Field effect experiments performed in this thesis have been done on ultrathin YBCO films (3 u.c.) to ensure doping of the whole sample thickness. In order to obtain high quality 3nm thin films preserving their optimal properties PBCO has been used as a buffer layer [235] and different approaches have been done to characterize both materials combining trilayers and superlattices of YBCO and PBCO.

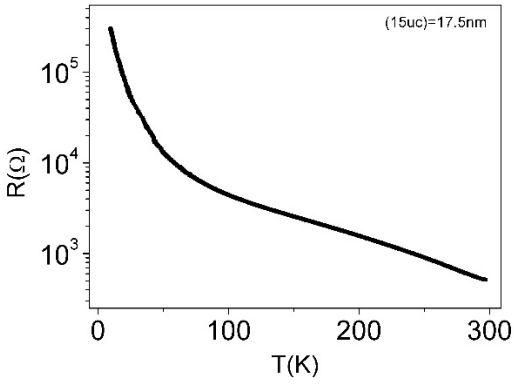

Figure 4.3 Resistance versus temperature curve for a thin film of 20nm PBCO grown by sputtering deposition.

Measurements of resistance versus temperature of a single thin film of 15u.c of PBCO are shown in Figure 4.3. The growth conditions, pressure and temperature are similar to the YBCO and also the annealing process. The PBCO is an insulator isostructural with the YBCO. Reflectivity and diffraction X-ray measurements are shown in Figure 4.4 for different thicknesses. As the thickness is increased from 14nm (black curve) to 18nm (pink curve) the first diffraction peak decreases in width. Finite size oscillations both in XRR and in XRD around the (006) PBCO diffraction peak shows the smoothness of the surface for all the samples.

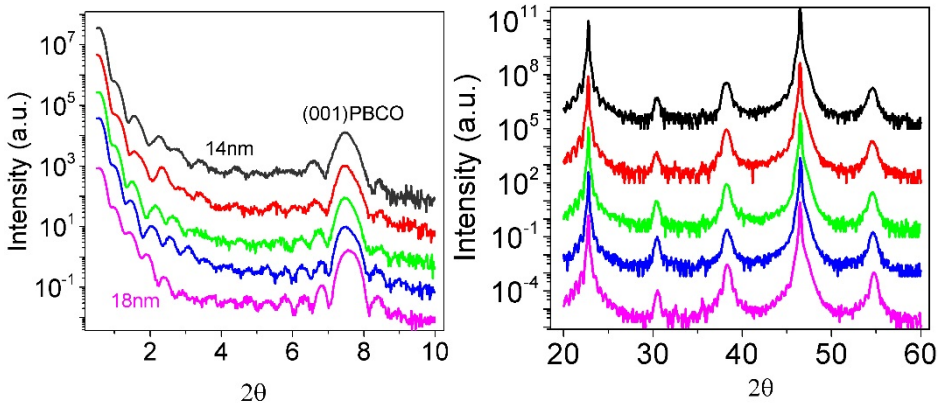

Figure 4.4. X-ray reflectivity and diffraction spectra of PBCO thin films grown for different thicknesses.

The same lattice parameters of the PBCO and YBCO makes the PBCO an ideal candidate as a buffer layer to warrant epitaxial growth of YBCO on top of it attesting good surface morphology and abrupt interfaces preserving the superconducting properties of YBCO even in ultrathin films [235].

1.2 Trilayers of PBCO/YBCO/PBCO

An experiment aimed at producing ultrathin films of YBCO has been done on trilayers $PrBa_2Cu_3O_7$ (10uc)/$YBa_2Cu_3O_{7-x}$(n)/$PrBa_2Cu_3O_7$(10uc) where the number of unit cells of YBCO was systematically decreased (n=4,3,2,1). The capping layer of PBCO is necessary to ensure the transport properties of the YBCO surface in contact with the atmosphere. We decided to use for the capping layer the same thickness as for the buffer layer.

Resistance versus temperature curves plotted in Figure 4.5 shows a decrease of the superconducting critical temperature as a function of the thickness due to the induced strain in the sample as previously observed in the literature [236–240]. The sample of just one unit cell of YBCO has a temperature of 50K (at a cero resistance) in accordance with the broad characterization of this system done previously by M.Varela [241].

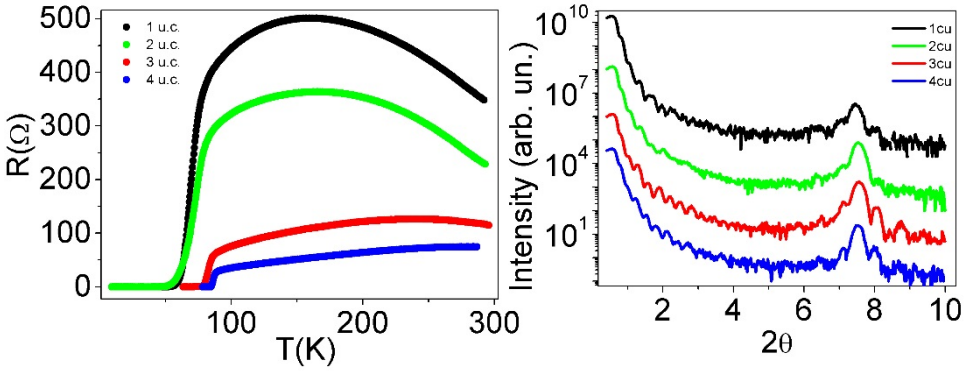

Figure 4.5 a) Resistance versus temperature measurements for trilayers $PrBa_2Cu_3O_7$ (10uc)/$YBa_2Cu_3O_{7-x}$(n)/$PrBa_2Cu_3O_7$(10uc) varying the amount of YBCO from 1 to 4u.c. b) XRR spectra for the same samples.

The ultrathin layer of YBCO has a refraction index slightly different from PBCO introducing a phase factor in the reflectivity pattern generated between the upper and lower PBCO layers. This phase factor is shown in the reflectivity pattern of the composite thin film by an extra thickness modulation. It is better observed as the thickness of the intermediate YBCO layer is increased as shown in Figure 4.4 for 3 and 4 u.c and in both samples of Figure 4.6 (5u.c and 10uc. respectively). It evidences that the thin YBCO layers are coherent over long lateral distances showing good structural integrity and high quality interfaces between the YBCO and PBCO.

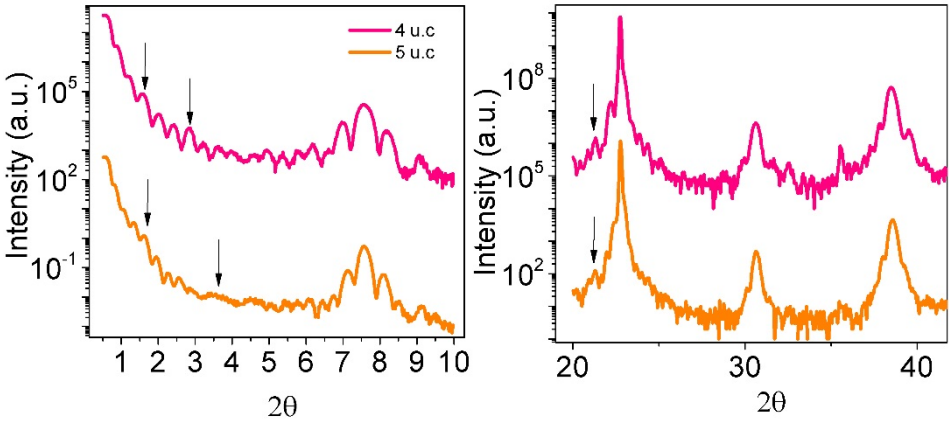

Figure 4.6 X-ray measurements, reflectivity and diffraction for trilayers of $PrBa_2Cu_3O_7$ (10uc)/$YBa_2Cu_3O_{7-x}$(n)/$PrBa_2Cu_3O_7$(10uc) where the thickness of YBCO is 5 and 10 u.c respectively.

1.3 Superlattice PBCO/YBCO

A series of superlattices of $[PrBa_2Cu_3O_7(2u.c)/YBa_2Cu_3O_{7-x}\ (2u.c)]_{x6}$ have also been characterized. They have been grown on a STO(100) substrate with a buffer layer of 5 u.c. of PBCO to warrant the superconductivity of the first layers of YBCO. And alternate combination of 2nm YBCO and 2nm PBCO has been deposited during 6 repetitions.

Finite size oscillations in the reflectivity spectra of Figure 4.7 shows planar surface over long distances and it is found two different interference patterns. One due to the total thickness of the sample, sensitive to the average refraction index of the superlattice, and the other one corresponding to the artificial modulation of the superlattice showing new maxima (labeled n=1) in the angular positions given by Bragg's law for grazing incidence. In this same figure for higher angles it is found the first diffraction peak of (001) YBCO and its corresponding satellite peaks for a superlattice.

Figure 4.7 b) shows the diffraction spectra of a $[PrBa_2Cu_3O_7\ (2u.c)/YBa_2Cu_3O_{7-x}\ (2u.c)]_{x6}$ superlattice were the superlattice Bragg peaks (labeled as 0) and the superlattice satellite peaks are labeled according to equation 3.2. The finite size

peaks corresponding to the whole thickness of the superlattice can be also observed.

The clear superlattice Bragg peaks displayed by both XRR and XRD spectra indicate flat YBCO/PBCO interfaces. Superlattice Bragg peaks around the substrate (002) Bragg peak in the XRD spectra are clearly seen as well as finite size oscillations around each satellite. This provides evidence of coherent heteroepitaxial growth with sharp interfaces.

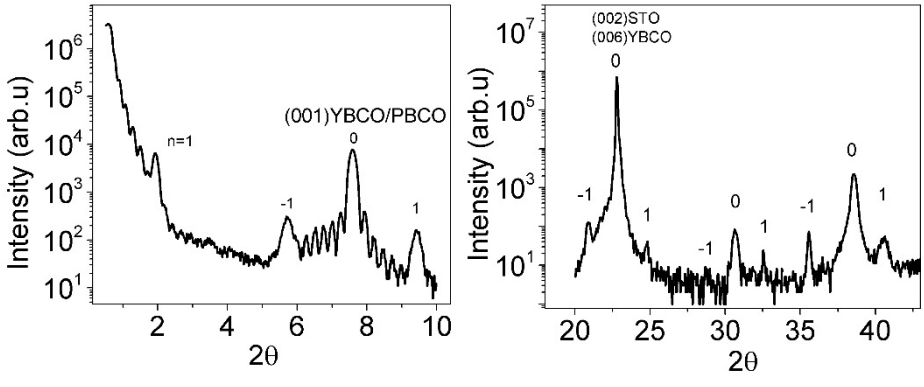

Figure 4.7. X-ray reflectivity of $[PrBa_2Cu_3O_7(2u.c)/YBa_2Cu_3O_{7-x}\ (2u.c)]_{x6}$ superlattice**.** X-ray diffraction spectra of a $[PrBa_2Cu_3O_7(2u.c)/YBa_2Cu_3O_{7-x}\ (2u.c)]_{x6}$ superlattice grown on STO (001) substrate.

Low magnification Z-contrast image of a $[PrBa_2Cu_3O_7(2u.c)/YBa_2Cu_3O_{7-x}\ (2u.c)]_{x6}$ superlattice is shown in Figure 4.8. A high angle annular dark field (HAADF) image show flat layers over long lateral distances and around 25 nm thin layer. Figure 4.8 (b) shows the 100 zone axis of the STO substrate by annular bright field ABF image.

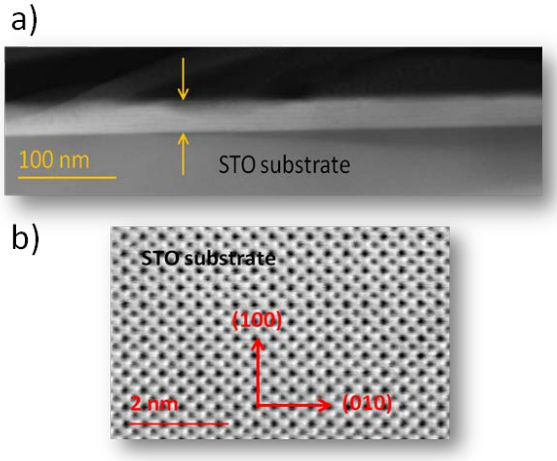

Figure 4.8. a) Low magnification Z-contrast image of a $[PrBa_2Cu_3O_7(2u.c)/YBa_2Cu_3O_{7-x}\ (2u.c)]_{x6}$ superlattice .b) show the 100 zone axis of STO by annular bright field ABF image. Images taken from Mariona Cabero at Centro de Microscopia

HAADF images in Figure 4.9 show the good quality epitaxy of the superlayer and the coherent growth of the structure. An alternate structure of 2u.c. PBCO/YBCO is clearly defined in the image with atomic resolution. Brighter spots correspond to heavier atoms, YBCO and PBCO are isotructural being Z of Pr higher that for Y, thus brighter planes are associated with PBCO.

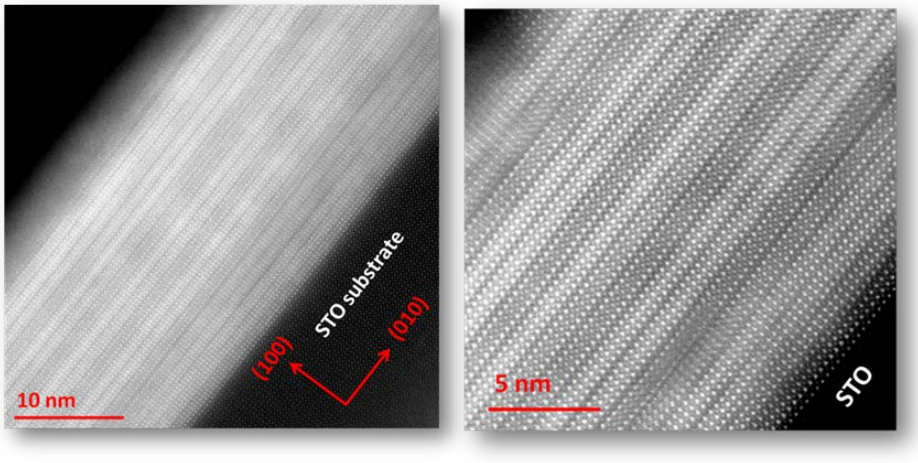

Figure 4.9. HAADF images of a $[PrBa_2Cu_3O_7(2u.c)/YBa_2Cu_3O_{7-x}\ (2u.c)]_{x6}$ superlattice. Images taken from Mariona Cabero at Centro de Microscopia

1.4 Growth of nanocristaline alumina (Al_2O_3)

The growth of amorphous alumina Al_2O_3 (ALO) will allow us to define the pattern for the field effect experiments. A previous systematic analysis of the transport properties, reflectivity and topography has been done.

The samples have been grown in a DC magnetron sputtering which has been built up during this PHD project. It has been used for deposition of amorphous aluminum oxide through reactive sputtering combing the reactive gas, O_2, with the inert Ar gas flow for different rates. In Figure 4.11 there is a summary of the growing characterization as a function of the deposition time (Figure 4.11a, I_{DC}=200mA, Rate=2:1), the rates between the different gases (Figure 4.11b, I_{DC}=200mA for 2 and 4h), and the applied DC current (Figure 4.11c, Rate=2:1, time=2h). All the samples have been grown at a $7.4 \cdot 10^{-3}$mbar chamber pressure and at room temperature. The optimal growth conditions were found at low rates=2:1, but high I_{DC} and high deposition time processes obtaining flat thin films over long distances as indicated by the finite size peaks of reflectivity spectra, amorphous is indicated by the observed diffraction peaks. All the samples exhibit a line structure topography pattern as it is show in Figure 4.10 with an AFM image and were insulating.

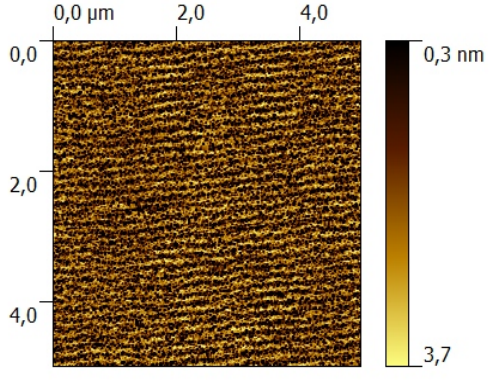

Figure 4.10. AFM image of nanocristaline ALO

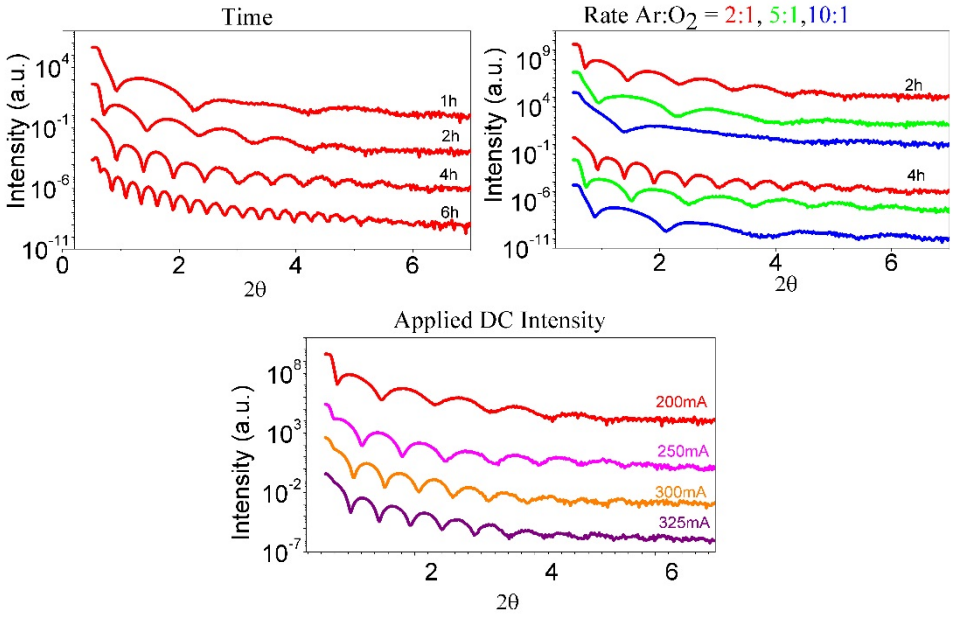

Figure 4.11. a) b) ALO characterization for different deposition times at I_{DC}=200mA, and for different gases rates. C) ALO deposition as a function of the I_{DC} applied intensity for a an Ar:O_2 rate 2:1 during 2hours.

Time	2:01	Thickness (Å)
1h	ALO35	52.31 ± 0.72
2h	AlO30	93.17 ± 0.53
4h	ALO33	161.17 ± 0.35
6h	ALO36	301.84 ± 0.55
	5:01	
2h	ALO07	54.8 ± 1.4
4h	ALO31	87.34 ± 0.51
	10:01	
2h	ALO32	38.87 ± 0.21
4h	ALO34	58.77 ± 0.94

DC Intensity		Thickness
200mA	AlO30	93.17 ± 0.53
250mA	ALO37	120.58 ± 0.51
300mA	ALO38	149.8 ± 1.1
325mA	ALO39	159.9 ±1.4

Table 4.1. Growth conditions and ALO thickness prepared by a DC magneton sputtering plotted in Figure 4.10.

2 Characterization of the Ionic Liquid

The ionic liquid that has been used in this thesis as a dielectric in the Electrostatic Double Layer Transistor (EDLT) is the so called N,N-diethyl-N-(2-methoxyethyl)-N-methylammonium bis (trifluoromethlysulphonyl) imide, simply named DEME-TFSI. The molecular structure is formed by the positive ion (cation), $DEME^+$, due to the missing electron around the nitrogen atom at the center, and the negative ion (anion), $TFSI^-$, due to the one electron excess around the nitrogen atom at the center. The molecular structures of DEME-TFSI with its constituent charged ions are represented in Figure 4.12.

It was found that the DEME-TFSI show a large capacitance allowing for charges in the sheet carrier density of up to $8 \cdot 10^{14} cm^{-2}$ on the surface of ZnO [10], eight times higher than what had been achieved using polymer electrolytes [12]. EDLT operate at temperatures in the "Rubber phase", in this range of temperatures where there is a suppression of the chemical reactions happening at room temperature (see Figure 4.12b) [242][243].

Ions in DEME-TFSI were found to be mobile down to temperatures as low as 200K. The DEME-TFSI does not exhibit a clear melting and freezing point, however, the glass-transition temperature, Tg, measured by Differential Scanning Calorimetry (DSC) methods has been observed at 183K [244]. Below the glass transition the effective electrochemical window is expanded, and hence, the possibility to applied higher V_G, will allows us to further increase the carrier density. Owing to the substantial supercooling properties of this liquid and its glass transition characteristics the DEME-TFSI is considered to be an optical choice for the use of EDLT doping experiments.

In order to use the DEME-TFSI as the gate dielectric it was previously characterized by frequency dependent measurements of capacitance and conductivity by dielectric spectroscopy.

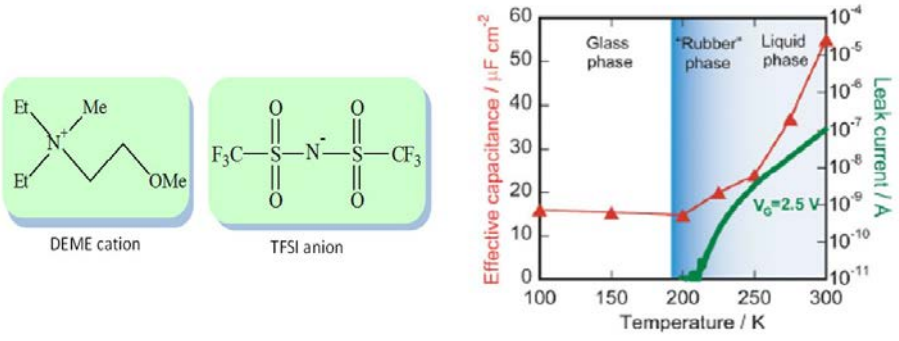

Figure 4.12 The molecular structure of DEME-TFSI. $DEME^+$ is the positive ion (cation) due to the one deficient electron around the nitrogen atom at the center, while the $TFSI^-$ is the negative ion (anion) due to the surplus of one electron around the nitrogen atom at the center.

An ideal ionic conductor with not interacting charge carriers exhibits the so called electric field relaxation. Capacitance and conductance exhibit the characteristic Debye like behavior. Capacitance shows a down-step forwards high frequency while conductance shows an up-step due to the blocking of charge carriers at the electrodes. In the time domain this dielectric response is governed by an exponential (Debye) relaxation function. Coulomb interaction between carriers give rise to non-exponential relaxation in the time domain, often described by the Kohlrausch-Williams-Watts (KWW) stretched exponential function [245].It has been used for representing time-dependent relaxation functions of ionic liquids. It is an indicator of the interaction of the charge carriers, particularly the asymmetric ones of the ionic liquids.

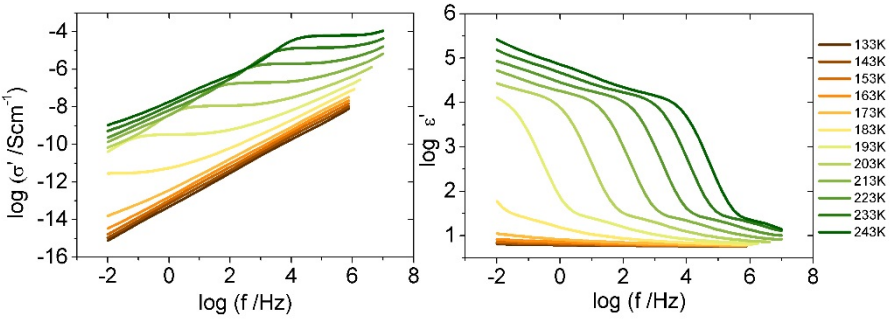

Figure 4.13. a) Real part of the conductivity of the IL versus frequencies at different temperatures. b) Real part of the dielectric permittivity behavior versus frequencies for the ionic liquid

Figure 4.13a) shows the conductivity measured for a wide temperature range as a function of frequency. In addition to the intrinsic conductivity of the ionic liquid (plateau), there is at low frequencies a decrease associated to the contribution of the charge originating the blockade at the electrode. At high frequencies the exponential behavior makes the conductivity to increase above a crossover frequency, ω_p , associated with the stretched exponential relaxation. The inverse of the crossover frequency ω_p gives a characteristic time in the conductivy process $\tau_p = 1/\omega_p$. For frequencies lower than ω_p o times larger than τ_p the ions are in the long range conduction regime. However, for frequencies higher than ω_p or times lower than τ_p we can talk about local ion motions where the interaction between ions produce a behavior departing from the ideal Debye electric field relaxation.

This particular potential dependence of the electric conductivity has been called by A. Jonscher "Universal Dynamic Response" [246] and it can be described as:

$$\sigma * (\omega) = \sigma_0 \left(1 + \left(i\frac{\omega}{\omega_p}\right)^n\right)$$

n give us the degree of deviation from the ideal conduction process, so if n were n=0 the charge carriers would not interact and the conductivity will be constant for each frequency and the electric modulus would yield the Debye type behavior.

As the temperature is decreased there is a shift of the crossover frequency to lower values, the mobility of the ions is reduced, and below 183K (yellow line), the ionic liquid is below the glass transition and the long range motion of the ions becomes negligible. At low temperatures there is a linear dependence with the frequency associated with the so called constant losses regime [247] where the imaginary part of the permittivity ε'' will show a constant value (magnitude that indicates the electric losses of the material).

Figure 4.13 b) shows frequency dependent of the real part of the dielectric permittivity, ε'. Low frequencies show the extrinsic capacity of the electrode-sample interface contribution, and for high frequencies it is measured the intrinsic sample contribution (ionic liquid). departing from the horizontal behavior of a Debye type response there is a gradient in this contribution associated to the non-exponential response due to charge carrier's interaction. As the temperature is decreased the power law dependence shows up and a shift to low frequencies in a thermally activated fashion.

The imaginary part of the electric modulus (M'') allow us to determine the characteristic relaxation time of the low capacitance due to the ionic liquid (see Figure 4.14). It shows a maximum at a characteristic frequency that is inversely proportional to the electric field relaxation time [247]. Contrary to the Debye behavior the maximum is non-symmetric and it shows a shift to lower frequencies as the temperature is decreased. Below 183K the ionic liquid enters in the glass phase and accordingly large relaxation times are found. this value is in good agreement with the glass transition temperature, Tg, for the DEME-TFSI measured by calorimetry techniques (DSC).

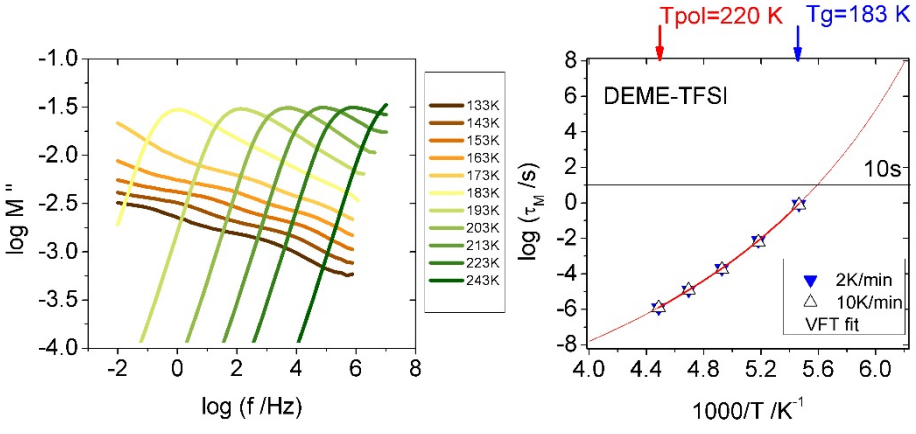

Figure 4.14 a) The imaginary part of the electric modulus versus frequency for the IL showing the peak at a certain frequency associated with the relaxation time. b) Relaxation time versus 10^3/T showing the exponential behavior of the IL.

The relaxation times obtained from the modulus peaks are plotted in Figure 4.14 b) as a function of the 10^3/T showing the exponential Vogel Fulcher Tammann (VFT) behavior, characteristic of the ionic liquids, which departs strongly from the linear Debye behavior due to the interaction of the charge carriers. That important degree of asymmetry is characteristic of glass former behavior that do no crystalized. The equilibrium liquid relaxation time is estimated to be 10s.

3 Device patterning for the EDLT

The device for the EDLT was fabricated on top of (001) oriented $SrTiO_3$ (STO) substrate using a pattern of nanocrystalline ALO deposited using mechanical masks. The insulating alumina allow us to define the active channel of the superconductor YBCO, grey rectangle in figure 4.15, as well as the gold electrodes for the transport measurements and the gating process, top yellow rectangles and bottom yellow rectangle) respectively.

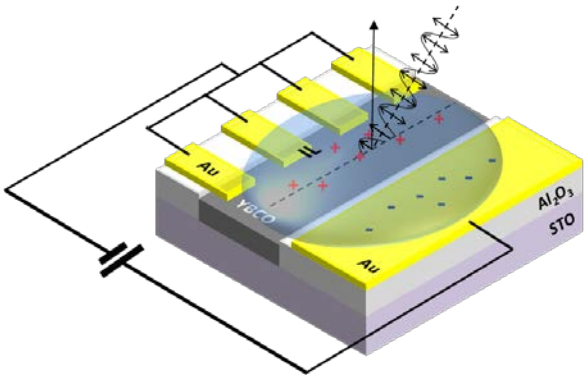

Figure 4.15 Schematic representation of the double-layer field-effect transistor device in YBCO showing the configuration of the gating process and the geometry of the X-Ray measurements.

The 3 unit cell thick YBCO thin film was grown on top of a 5 unit cell thick PBCO buffer layer to ensure optimal superconducting properties an excellent epitaxial properties Notice that on top of the bare STO substrate the films are epitaxial and superconductor (see Figure 4.16a) while on top of the nanocrystalline ALO there is no growth of YBCO and PBCO but the deposition of the corresponding binary oxides forming a non-crystalline composite showing an insulator behavior (see Figure 4.16b).

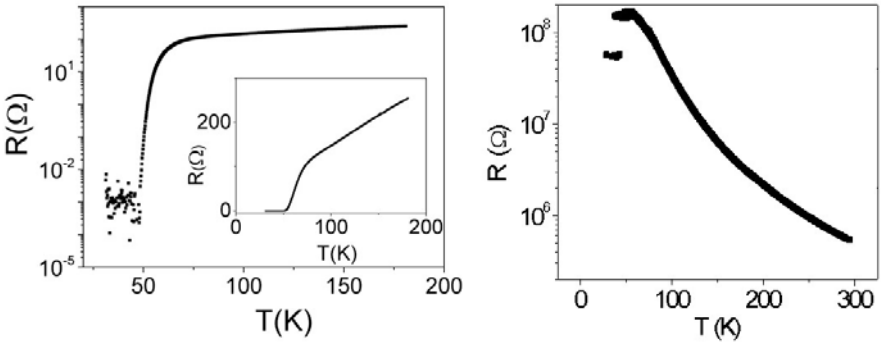

Figure 4.16. Resistance versus temperature of a) the active channel of YBCO, b) the binary oxides of PBCO and YBCO grown at the top of the ALO.

The gate dielectric was deposited using a 1 μl drop of the ionic liquid DEME-TFSI as sketched in Figure 4.16. To prevent the reaction of the surface of the sample with the water of the ionic liquid, the DEME-TFSI was previously baked at 100°C and at 10^{-2} Torr during 24 hours. The ionic liquid drop was spread over the sample's surface using a 10 μm thick polyester film allowing for a vertical configuration inside the He flow cryostat.

4 Measurement Procedure

The doping process that has been followed is indicated in the sketch of Figure 4.17. Starting at 180K, the temperature is raised above the glass transition temperature, T_{pol}=230K, and an external bias, V_G, is applied between the sample and the gate electrode during 10 min. Intensity versus time curves have been measure to determine the leakage current during the charging process. After that, the temperature is decreased to freeze the ionic liquid into the glass phase while the V_G is kept applied to the system.

At 180K, the bias is turned off and using a Switching System 2123, which has been mounted and assembled during this thesis, we set the Van der Pau configuration to make a four-point transport measurement of the YBCO while temperature is decrease. The absorption spectra have been measured at 20K. While the temperature is increased, resistance versus temperature measurements are recorded again up to 180K, where polarization configuration is recovered to restart the cycle with a new V_G. The new sequence starts always with the last voltage, V_{Gi}, applied, to warrant that as the temperature is increased to T_{pol}, (during the IL melting process) there is not a discharge relaxation process.

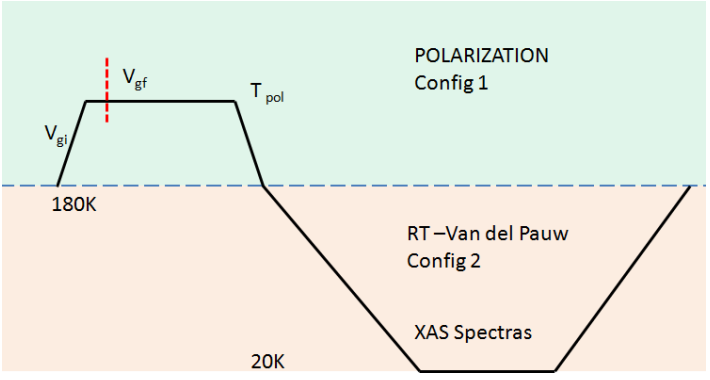

Figure 4.17 Temperature ramps during the doping procedure

4.1 Charge polarization curves

The polarization curves associated with the charging process of the IL are measured for each applied V_G followed by the relaxation decreasing to a background level. As the V_G reaches higher values the background level increases for both positive and negative V_G.

In Figure 4.18, different gate voltages are applied to the system while the leakage current is monitored. The total current is a combination of non-Faradaic charging current (decaying exponentially) and Faradaic electrochemical current (described by Cottrell equation) [248]:

$$I = \frac{nFA\sqrt{D}c}{\sqrt{\pi t}}$$

where n is the number of electrons transferred, F is the Faraday constant, A is the area of electrode, D and c are diffusion coefficient and bulk concentration of the reactants in the electrolyte, respectively. From the charging plot it could be inferred that practically it takes about 10 min for the gate's EDLC to be fully charged under a DC bias even though charging time will also depend on device geometry.

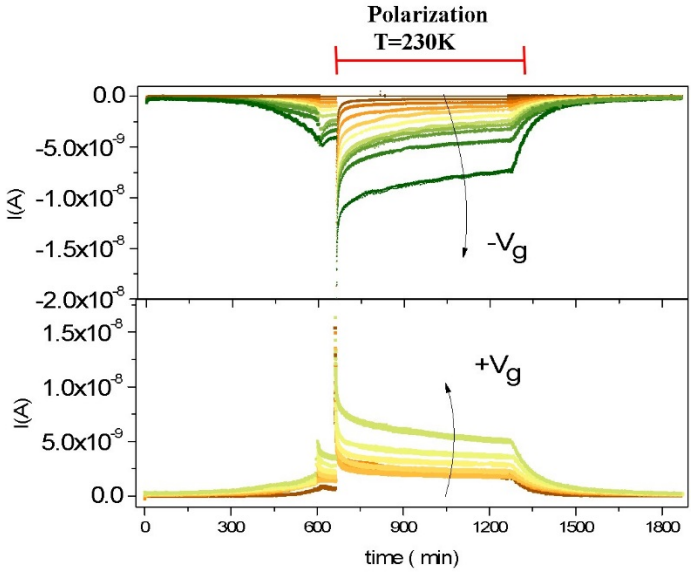

Figure 4.18 A series of intensity versus time curves measuring the current leakage for positive and negative bias when the polarization process is happening.

Above a certain defining voltage value, electrochemical window reactions can happen at the surface of the sample damaging the IL and inhibiting the polarization process. Measuring the current leakage, it is a well selected technique to identify the proper polarization mechanism. Breakdown of the doping process has been identified when voltage is raised above the electrochemical limit showing two different breaking behaviors. The current leakage experiments a decrease of the charging peak followed by an inversion of the polarization (see Figure 4.19(a)), or its magnitude increase up to values as high as $1 \cdot 10^{-7}$ showing finite oscillations due to the reactions with the surface (see Figure 4.19(b)).

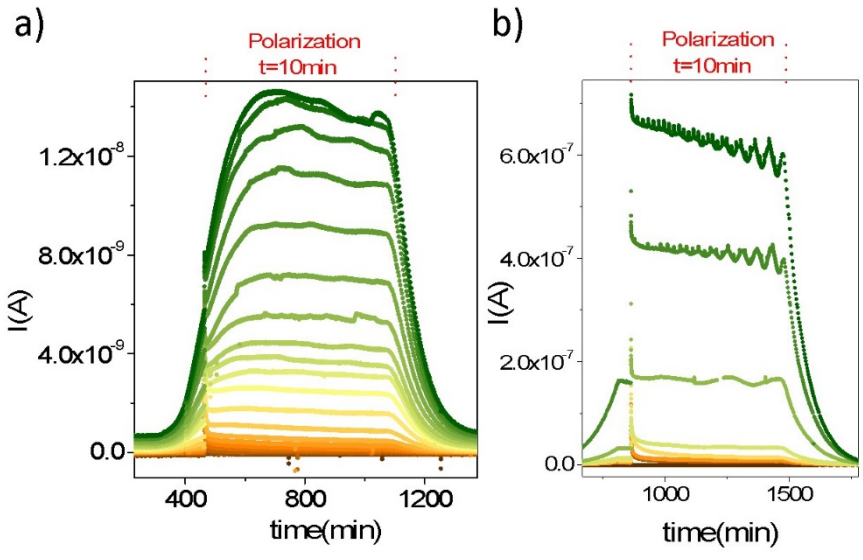

Figure 4.19 Over the V_G electrochemical window, chemical reactions start to occur in the IL- YBCO interface and the polarization process stops without moving the Tc anymore. A series of intensity versus time curves measuring the current leakage for positive and negative bias.

The electrochemical reactions between IL and the YBCO and/or moisture reactions may mimic the 'pure' field effect from electrostatic doping and lead to ambiguity and complexing in the data interpretation. A deep understanding of the electrochemical interactions of the IL with the surface is of most importance for the interpretation of the field-effect phenomena.

CHAPTER 5

YBCO superconductor-insulator transition and its reversibility

1Motivation

Electrolyte gating of complex oxides has proven to be a powerful tool for studying the electronic phase boundaries and the response of these materials to strong electric fields. Moreover, understanding the doping mechanism behind the EDL technique has become a crucial topic of fundamental research. The origin of large modifications of the conducting state and the associated emergent properties observed in such field effect devices is a matter of intense debate due to competing contributions from electrostatic (charge accumulation) and electrochemical (changes of the crystal chemistry) effects [22, 23, 185, 249].

Understanding the mechanism of the doping process may uncover further methods to control the interfacial charge transfer and the related electronic conductivity at interfaces. This may have implications for the design of future field effect devices with high carrier density systems in a broader setting.

2 Superconductor-Insulator transition

Resistance versus temperature measurements for the different applied voltages are shown in Figure 5.1 exhibiting the superconductor-insulator transition The system has been driven to the insulating phase applying positive V_g starting at 0.2V and systematically increasing each ΔV_g= 0.4V from 0.4 to 2.4V. A threshold voltage associated with the start of the T_c decrease is obtained suggesting the existence of an activation process. Once the system has been activated, a small increase of V_g

leads to a significant decrease of the T_c, as happened between 2 and 2.4V where an abrupt modification of the resistance and suppression of the T_c is observed for the same applied voltage ΔV_g indicating that the transition has been passed. This is the first indication that a two-steps doping process may be happening in the experiment.

All the measurements have been done at T_{pol}=220K and the voltage applied during 10 minutes. The raw data have been interpolated and the values of the T_c calculated by the maximum of the derivative of the resistive transition. The superconducting transitions of ultrathin films are broad and the T_c depends strongly on the criteria selected to calculate it showing an increase of almost 10K if is calculated from the onset transition temperature where the resistance drops to its 90% value. The samples are strained due to the thin film thicknesses of just 3 nm, and a depressed superconducting transition temperature is expected due to the strong thickness dependence of T_c [238–240].

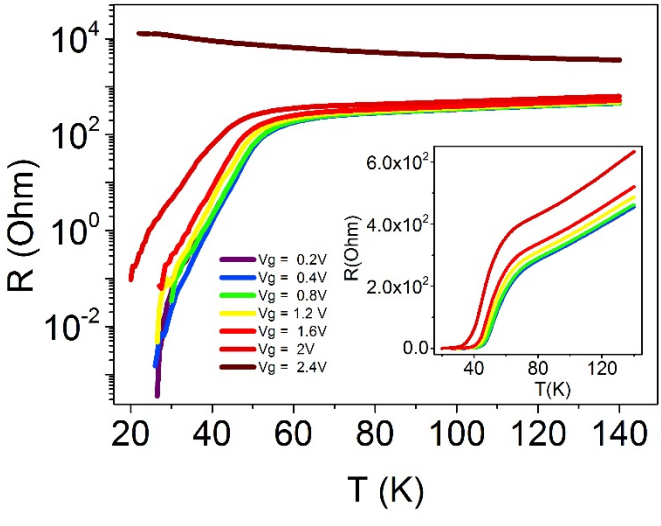

Figure 5.1. Resistance versus temperature measurements for different applied positive voltages.

T_c is known to depend on the number of charge carriers and on disorder through pair braking [250] and/or localization. These two variables determine the number of Cooper pairs. I.e. for a certain number of carriers, localization or pair breaking

effect may limit the number of pairs to its actual value, n_s, defining the superfluid density. In 123 cuprate compounds, the normal resistance is determined by the carriers both on the CuO_2 planes and on the CuO_x chains while T_c is mainly determined by the carriers on the CuO_2 planes [251].

As discussed below, crossing the MIT causes irreversibility in the doping process. In order to understand the doping mechanism associated with a decreasing of the T_c in the 3 u.c superconductor phase a new experiment was done keeping the system in the superconductor phase not allowing the system to pass the metal-insulator transition (see Figure 5.2).

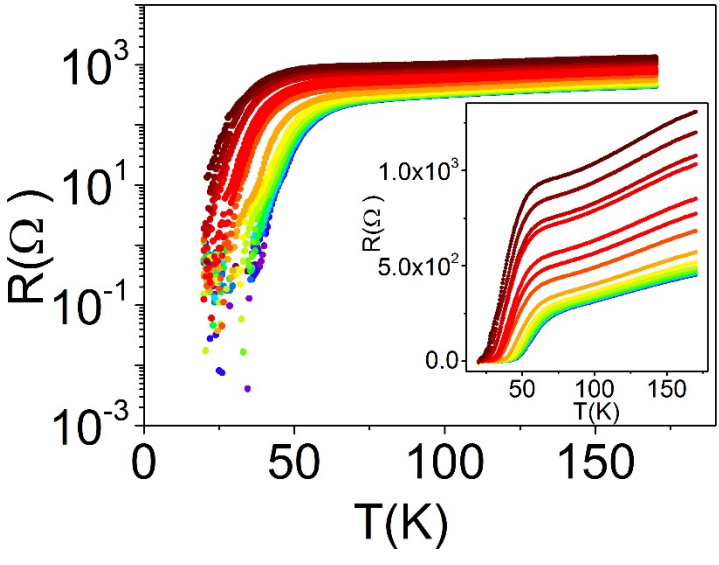

Figure 5.2. Resistance versus temperature measurements for positive Vg from 0 to 0.9V, and as a function of the polarization time (from 10 to 110 min) at a constant Vg=0.9V

In this experiment, positive gate voltages were applied in 0.1 V steps up to 0.9 V. The polarization temperature was the same in the whole experiment, 220K. A required threshold V_G is also found to produce a shift of the T_c (blue area) exhibiting a parabolic behavior decreasing with the voltage once the process has been activated (pink area). Then voltage was fixed at this value and we measured the evolution of resistance curves as a function of the polarization time (from 10 to 110 min) which led to further decrease of the critical temperature characteristic

of a larger degree of underdoping (see green area of Figure 5.3)). The decrease of the Tc as a function of the polarization time at a constant gate voltage is by itself a strong indication that (apart from the simple electrostatic screening effect) oxygen migration plays a role in the doping process. As before, the T_c was calculated as the maximum of the derivate of the resistance versus temperature measurements for what the raw data were previously interpolated.

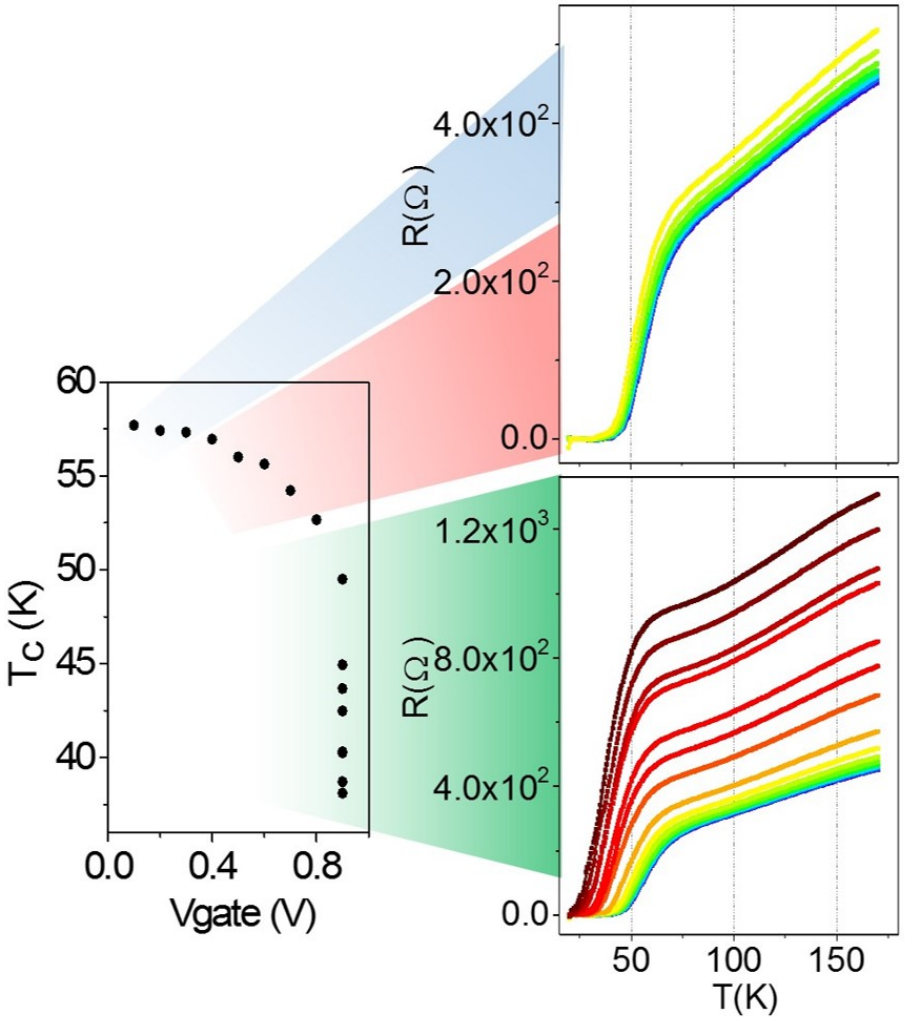

Figure 5.3. Resistance versus temperature measurements for positive Vg from 0 to 0.9V, and as a function of the polarization time (from 10 to 110 min) at a constant Vg=0.9V

3 Quantification of electric disorder using Matthiessen rule

While the system is in the superconductor phase (before crossing the MIT) it is possible to quantify the electrical disorder, using the empirical Matthiessen rule. It expresses the resistivity of a metallic sample as the sum of two contributions (one coming from the interaction with phonons and the other due to the disorder or crystallographic imperfections). The resistivity of a metallic crystal can be expressed as:

$$\rho = \frac{m^*}{ne^2\tau} \tag{1}$$

Where m* is the effective mass of the electron, n is the number of carries, e is the charge of the electron, and τ is the scattering time.

The scattering time has thus a contribution due to the phonons, which is temperature dependent , and other one due to the scattering by impurities disorders or othe lattice imperfections, which is temperature independent.

$$\frac{1}{\tau} = \frac{1}{\tau_1}(T)\Big|_{phonons} + \frac{1}{\tau_0}\Big|_{disorder} = AT + \frac{1}{\tau_0}\Big|_{disorder} \tag{2}$$

The resistivity in the metallic state has a linear dependence with the temperature.

$$\rho = \rho_0 + \alpha T \tag{3}$$

$$\rho_0 = \frac{m*}{ne^2\tau_0} \tag{4}$$

$$\alpha = \frac{m*}{ne^2}A \tag{5}$$

Dividing the residual resistivity, by the slope of the metallic part we obtain a parameter that is proportional to the disorder and independent of the number of carriers where A is a constant value. As discussed below the linear resistivity term A has profound meaning in the HTS, which connects scattering in a non- Fermi

liquid to the mechanism of the superconductivity. In addition, the residual resistivity of the layers of YBCO is inversely proportional to both, the disorder and the number of carrier density.

$$\alpha = \rho_0 A \tau_0 \tag{6}$$

$$\frac{\rho_0}{\alpha} = \frac{1}{A\tau_0} \tag{7}$$

The equations (3-5) have been computed from the normal resistance linear term at high temperature. Figures 5.4 and 5.5 show the quantified parameters and the evolution of the Tc for the applied gate voltage (blue and pink area) and for the polarization times (green area).

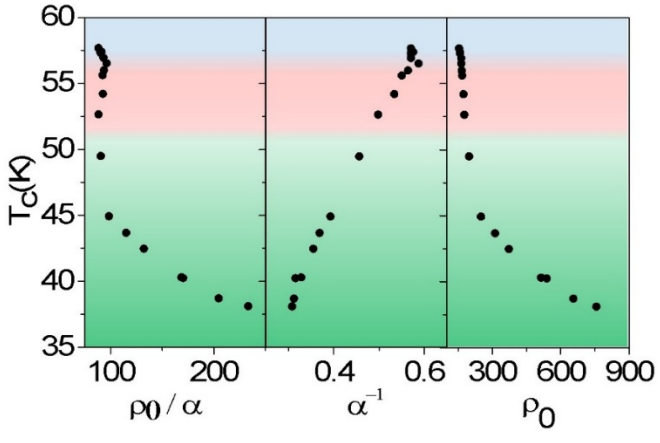

Figure 5.4 Evolution of the T_c, the electrical disorder $\frac{\rho_0}{\alpha}$, the parameter $\frac{1}{\alpha}$, and the residual resistance ρ_0, as a function of the applied voltage V_g (blue and pink area) and the polarization time (green area).

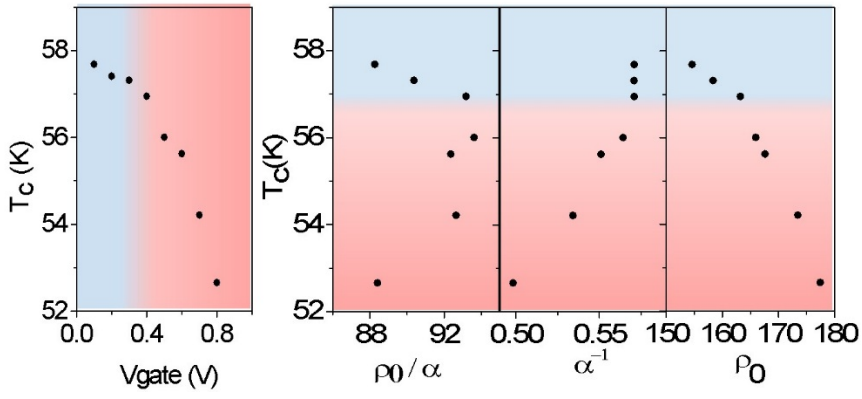

Figure 5.5. Zoom of the Figure 5.4 showing the evolution of the Tc as a function of the applied gate voltage for the electrical disorder $\frac{\rho_0}{\alpha}$, the parameter $\frac{1}{\alpha}$, and the residual resistance ρ_0,

Two different doping mechanism can be inferred which modulate the Tc; one as the gate voltage, Vg, is increased (blue and pink area), and the other for larger applied polarization times, Tpol, (green area). In Figure 5.2 and Figure 5.3 the disorder parameter $\frac{\rho_0}{\alpha}$, the parameter $\frac{1}{\alpha}$. and the residual resistivity , ρ_0, measured as the zero temperature extrapolation of the normal state resistivity for the three areas have been plotted.

As the voltage is increased and the system doped to lower T_c there is a slight increase of the intrinsic values of the electric disorder $\frac{1}{\tau}$ (proportional to $\frac{\rho_0}{\alpha}$) while $\frac{1}{\alpha}$ remains constant (blue area). Notice that $\frac{1}{\alpha}$ is proportional to the number of charge carriers in the sample although it is also affected by scattering. Up to a certain threshold voltage the disorder decreases and also does the parameter $\frac{1}{\alpha}$. This is an indication of a two-steps doping process happening as the gate voltage is applied.

An effective hole doping " p" has been inferred by using the empiric parabolic relation described by J. Tallon [102], which has been proven to hold to be true for bulk high T_c superconductors including 123 compounds [101].

$$\frac{T_c}{T_{cmax}} = 1 - 82.6(p - 0.16)^2 \quad (8)$$

Figure 5.6 shows the modulation of the T_c and the different values estimated for the p parameter. The black triangles represent the evolution of T_c versus the number of holes/ Cu ‘‘p’’ computed using the empiric parabolic relation (equation 8) where the $T_{c\,max}$ has been obtained for the V=0V value. In the same figure, in the upper axis $\frac{1}{\alpha}$ has been plotted which, as expected, scales linearly with p. The small decrease of the T_c for this voltage range, does not allow to access the superconducting dome observed in a wider doping range, and only a small linear regime can be studied.

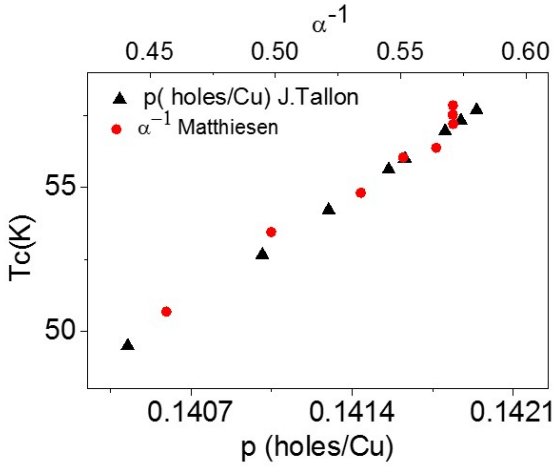

Figure 5.6. Dependence of the calculated p carriers (holes/Cu), the α^{-1} with the critical temperature.

Two scenarios can be considered to explain the evolution of the Tc with the applied voltage in electrolyte gating (blue and pink area). One associated only with ions accumulated and forming an EDL at the solid/liquid interface where the additional carriers are induced electrostatically, and the other associated with electrochemical changes that could lead to resistance modulation by creating defects (ion migration, oxygen vacancies) and the corresponding charge compensation.

From the pure electrostatic picture it was suggested that the doping of YBCO is a two-step process [18]. First the carriers are induced only on the CuOx chains, and second, once a threshold concentration is reached, carriers can be induced on the CuO_2 planes indirectly doped through intracell charge transfer [6]. In this scenario, below the threshold voltage, Tc is not modified, yet the normal state resistance increases which would be an indication that the carriers can be induced only on the CuOx chains. Above the threshold voltage V_G, the carriers can be induced reversibly on the CuO_2 planes by the electrostatic charging and thus the Tc and the normal resistance change together. In this way, the threshold voltage found in our experiment is in accordance with the idea of this two-steps doping process.

However, from the electrochemical picture, the existence of the threshold voltage also is supported by the idea of an activating barrier for the creation of oxygen vacancies and the corresponding oxygen diffusion process. Once the process has been activated any change of the hole doping (under the superconducting dome) will simultaneously affect the normal resistance and the superconducting properties.

The large increase in the electrical scattering disorder due to large polarization times (see green area in Figure 5.4), from 10 to 120 min, induce us to think that are happening electrochemical reactions in the surface damaging the YBCO/IL interface. Special care has to be taken with this parameter to avoid damage due to the reactivity of the IL at 220K. For this reason, for all remaining experiments the polarization time was keep constant at 10 minutes, which also reduces the number of experimental variables.

4 Reversibility of the process

An important issue to address is the reversibility of the doping process. We have conducted an experiment in which negative voltages were applied to restore the initial state after driving a sample into the underdoped regime by applying positive gate voltages.

Looking back to the results shown Figure 5.3 a dramatic shift of the Tc was found as a function of the voltage and as a function of the polarization time (from 10 to

110 min) keeping the system at a constant Vg. Afterwards, negative gate voltages were applied to restore the initial state (see Figure 5.6). Larger absolute values of the negative voltages than the positive values were needed to produce the underdoped state. By applying -4 V the superconducting critical temperature is fully recovered, showing the reversibility of the gating process. In fact, the Tc value for -4 V is even slightly higher than the initial one, which indicates that in addition to the oxygen migration an electrostatic effect is present in the doping process (oxygen backdiffusion due to the negative voltages cannot yield larger hole doping than the initial state).

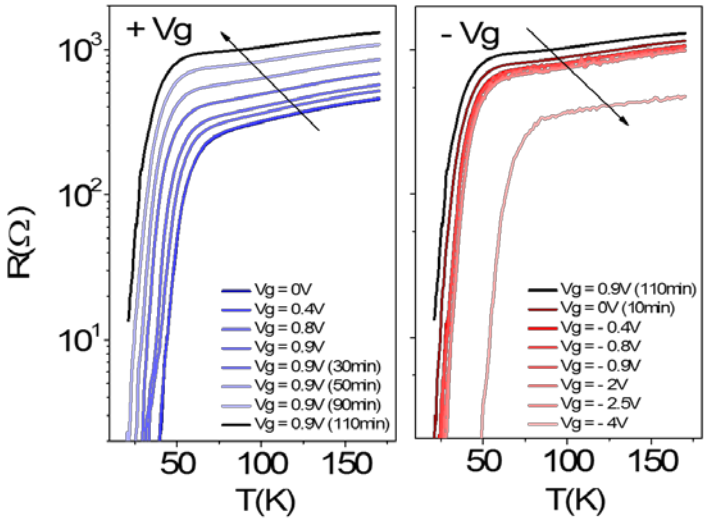

Figure 5.6 Resistance versus temperature curves measured for positive and negative gate voltages showing the reversibility of the process as long as the superconductor-insulator transition is not reached. a) Positive gate voltages were applied in 0,1 V steps up to 0.9V producing a systematic shift of Tc. In addition, the evolution of the resistance curves is also plotted as a function of the polarization time (from 10 to 110 min) leading to further decrease of the critical temperature underscoring the important oxygen migration role in the doping process. b) Negative gate voltages allow the system to recover its initial state showing an hysteretic voltage behavior. By applying -4 V the superconducting critical temperature is fully recovered, showing the reversibility of the gating process.

Device operation is reversible as far as the superconductor- insulator transition is not reached. Figure 5.7. Negative voltages were applied starting from the insulating state (2.4V curve of Figure 5.1) from V_g = -0.4 to -2V each ΔV_g= -0.4V. and no reversibility up to the initial superconductor state was found but a hysteresis

behavior was present. We can talk about a final inhomogeneous superconductor state characterized by a metallic resistivity state and a T_c onset (see Figure 5.7). This might result from the difficulty to create a large homogeneous electric field once the system has reached an insulating state and/or from destructive electrochemical reactions for large oxygen depletion from the sample.

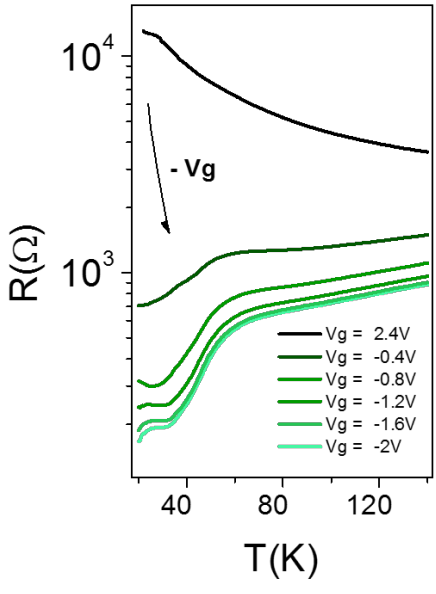

Figure 5.7. Resistance versus temperature curves for different applied negative voltages looking for the reversibility in an insulating YBCO previously doped sample. Just a metallic state is found but no superconductivity.

As long as the metal to insulator transition is not crossed, the results confirm that the doping process is reversible with a hysteresis behavior as function of gate voltage in accordance with the measurements of J.Barriocanal et al.[18]. Possible explanations are as follows. We may have to consider that an irreversible oxygen depletion may be produced during doping and therefore larger and reverse polarity voltages are necessary to restore the initial value of the Tc. A threshold gate voltage of reverse polarity is needed to change the sign of the ions that covered the surface at the interface between the ionic liquid and the cuprate, and hence destroy the electronic double layer, which could lead to the observed hysteretic dependence.

Furthermore, anions and cations from the ionic liquid are different in size and molecular weight and an asymmetric response to positive or negative gate voltages can be expected.

5 Conclusions

In this chapter the modulation of the T_c using and electric double layer to dope the superconducting YBCO has been studied. A threshold V_G was found necessary to obtain a large decrease of the T_c revealing that doping can be regarded as a two-step process.

Quantification of scattering disorder using the Matthiessen rule support this two-step doping process showing a different behavior in the electric disorder and the number of charge carriers above threshold voltage. A first interpretation of the doping mechanism (which will be further substantiated later) can be anticipated: the Tc starts to decreases associated first with a purely electrostatic doping due to the formation of screening charges at the interface followed by the second doping step associated with oxygen displacement, thus leading to a complex doping process combining electrostatic and electrochemical processes.

Special care has to be taken to avoid electrochemical reactions in the surface of the IL/YBCO interface as a result of large polarization times that would make the Tc to decrease by increasing the electrical disorder due to the interface damaging. As a consequence, the polarization time in the rest of the experiments was kept at a constant value of 10 minutes low is enough to charge the capacitor without causing surface damaging.

Speaking about the reversibility, the intrinsic original superconductivity is recovered if the system remains in the superconducting phase without crossing the metal to insulator transition. Once the system has been carried to the insulating phase, reverse voltages to restore the initial state drive the sample into an inhomogeneous state.

CHAPTER 6

In-operando evidence of deoxygenation in ionic liquid gating of $YBa_2Cu_3O_{7-X}$

1 Motivation

The debate on the true nature, electrostatic vs electrochemical, and the necessity of careful study the mechanism behind the EDL doping with ionic liquids is essential to fully understand the innermost origin of the generated electric charge at the interface of the doped material. Recent results obtained with EDL transistors based on VO_2 have challenged the conventional interpretation that EDL doping of oxides is due only to the electrostatic screening of the accumulated charges at the interfaces showing that it also involves the migration of oxygen atoms of the crystallographic unit cell [22, 23].

A complete and advanced understanding of the previously proposed two-steps YBCO doping process governed by an oxygen displacement was needed. In this chapter, we address the doping mechanism of the high temperature superconductor $YBa_2Cu_3O_{7-X}$ (YBCO) by simultaneous ionic liquid gating and X-ray absorption experiments.

Pronounced spectral changes are observed at the Cu K-edge concomitant with the superconductor-to-insulator transition, evidencing modification of the Cu coordination resulting from the deoxygenation of the CuO chains, as confirmed by first principles density functional theory (DFT) simulations.

The charge transfer between CuO_2 planes and CuO_X chains yielding superconducting planes is therefore hindered and the superconductivity suppressed.

2 Measurement assembling

EDL transistors for 3.u.c YBCO in side gating geometry were fabricated as it was indicated in Chapter 4 (Figure 4.15). It was tuned the cuprate from superconductor to insulator by applying positive gate voltages while measuring absorption spectra in the Cu K-edge. Figure 6.1(a) shows the R(T) curves corresponding to gate voltages, V_G = 0, 4, 5 and 10 V. The fresh sample, without an applied V_G, has a T_C close to the corresponding optimally doped 3 u.c. YBCO thin film and evolves into the insulating state with increasing gate voltage as expected with electron doping (hole depletion).

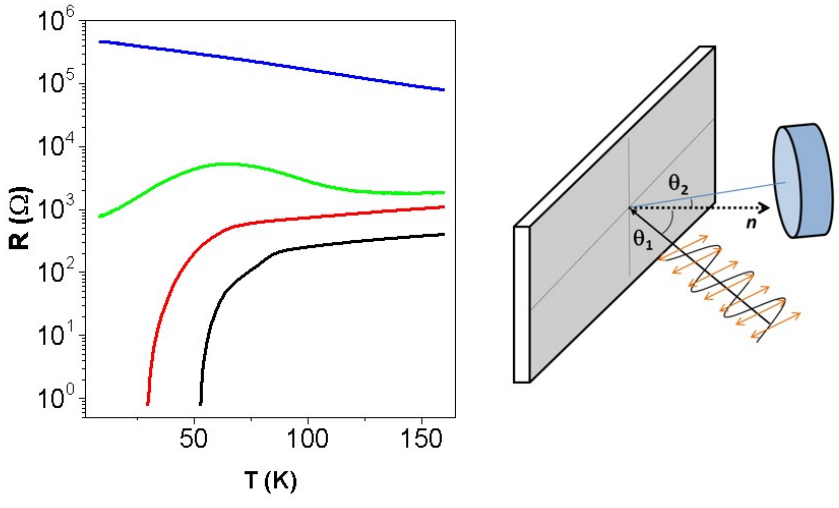

Figure 6.1. a) Resistance versus temperature curves measured at different gate voltages: 0 V (black), 4 V (red), 5 V (green) and 10 V (blue). b) Sketch indicating the synchrotron measurements were done with linearly polarized x-rays with an incident angle of 40° with respect to the normal of the sample.

3 *In-situ* NEXAFS spectra while doping

Near-edge x-ray absorption fine structure (NEXAFS) spectra were collected at the Cu K-edge at 10 K at the beamline BM25A of the European Synchrotron Radiation Facility (ESRF) simultaneously with gating using an ionic liquid. The NEXAFS technique is element-specific and the spectral features correspond to electronic transitions of the excited core electrons of Cu atoms to unoccupied states. The technique provides local electronic structure and coordination information due to the necessary spatial overlap between the core-level states and the empty final states.

The synchrotron measurements were done with linearly polarized x-rays with an incident angle of 40° with respect to the normal of the sample see Figure 6.1(b). The XAS signal was collected with a fluorescence detector mounted at an angle of 10° with respect to the normal of the sample surface. The gate voltage (V_G) was applied at 220 K for a period of 10 minutes and the device was immediately cooled down to 10 K. The R(T) curves were recorded during the warming of the sample up to 180 K and the XAS measurements were done at 10 K.

In Figure 6.2(a), we show the NEXAFS spectra collected as a function of the gate voltages, 0 V (black line, 4 V (red line), 5 V (green line) and 10 V (blue line). Due to the complex set up in the XAS line and the dependence of the gate voltages on the polarization temperature; it was necessary to apply high V_G in order to have standard values of the leakage current in the charging process. In Figure 6.2(a), it can be observed that the pre-edge and main edge are both strongly affected by the gating process. Upon positive gating, the intensity of the pre-edge line of the Cu K-edge (labeled A) increases systematically while the intensity of the white line (labeled B) of the resonant peak decreases. In figure 6.2(c), we have plotted the difference between the spectra obtained under 4, 5 and 10 V and the spectrum obtained without applied gate voltage (red, green and blue curves, respectively). The difference is positive around the pre-peak of the Cu K-edge, located at 8985 eV approximately, and negative around the main absorption edge, located around 9000 eV, highlighting the spectral weight transfer between the main edge and the pre-edge that is produced during the gating process.

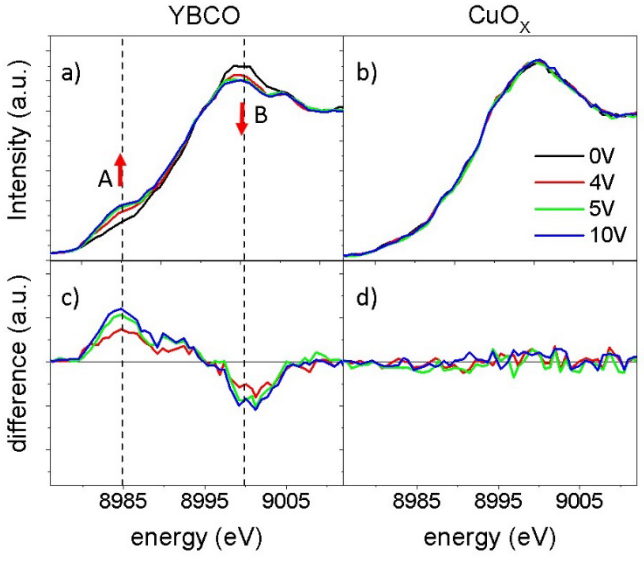

Figure 6.2. Evolution of the Cu K-edge NEXAFS spectra of YBCO (a) with increasing gate voltage [0 V (black), 4 V (red), 5 V (green) and 10 V (blue)]. (b) No evolution is found for the CuO_X deposited under the gate electrode. The difference spectra determined by subtracting the 0 V curve from each of the other curves for YBCO and the CuO_X are shown in panels (c) and (d) respectively. As expected the differences for the spectra of the CuO_X deposited on top of alumina and under the gold gate electrode are negligible

As a control test of the experiment we have measured the Cu K-edge absorption spectra of the binary Cu oxide that grows on top the alumina and below the gold gate electrode. For these materials, the Cu ions should not be affected by the electric field of the ionic liquid that is completely screened at the gold electrode. Figures 6.2(b) and 6.2(d) exhibit no measurable difference between the spectra measured below the gold electrode at the different applied gate voltages suggesting that all changes in figures 6.2(a) and 6.2 (c) arise from the electric field generated at the interface between YBCO and the ionic liquid.

In this experiment, we probe core-excited states comprising of a 1s hole and a local electronic p character at the same site consistent with the dipole selection rule. Because NEXAFS is strongly sensitive to hybridization between the Cu and O p orbitals, changes in spectral features can be related to the modification of the local

environment around the absorbing species. Aside from this, changes in the valence charge of the excited atom modify the core-hole screening and are related to the energy position of the absorbing edge allowing the probe of charge transfer effects.

Notably, the changes in the absorption spectra observed when the gate voltage is increased are similar to those found previously [252–256] in NEXAFS spectra of deoxygenated bulk samples (see Figure 6.3), suggesting that oxygen content may be, in fact, modified by doping with the ionic liquid.

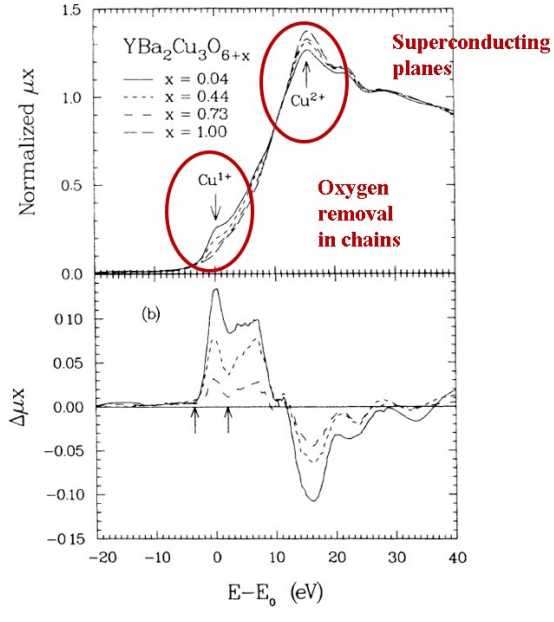

Figure 6.3. Tranquada XAS measurements for different oxygen content of YBCO samples

EELS measurements of optimally doped ($YBCO_7$) and deoxygenate samples($YBCO_6$) done at the chains and the plains in Cu L edge and O K edge support this scenario [256].

4 DFT simulations of NEXAFS

DFT calculations have been used to compute the NEXAFS spectra considering several possible doping scenarios.

The x-ray absorption spectra have been simulated using a plane-wave pseudopotential orbital-occupancy constrained DFT framework, employing the PBE functional within the PWSCF package [257]. For each configuration, we optimized both atomic positions and lattice parameters. The transition amplitudes were calculated according to Fermi's golden rule for the absorption cross-section within the electric-dipole approximation. We also computed the quadrupole matrix elements and found that they contribute negligibly to the total transition amplitudes. The initial and final states were single-particle Kohn-Sham eigenstates of the ground and excited-state self-consistent field, respectively. The initial state was the 1s orbital of Cu and the final state were accessible Kohn-Sham eigenstates derived from a self-consistent field computed within the excited electron and core-hole (XCH) approximation. Two similar implementations were used to compute the spectra yielding the same result, the xspectra utility [258] and the method by Prendergast et al [259, 260]. Starting from the transition amplitudes, the final spectra were computed using a Gaussian convolution of 0.8 eV using the experimental direction of the x-ray polarization. An average in-plane polarization was considered in order to mimic the presence of domains in the experiment.

First, we considered the scenario of oxygen removal from the CuO_x chains corresponding to stoichiometries of $YBa_2Cu_3O_7$, $YBa_2Cu_3O_{6.75}$, $YBa_2Cu_3O_{6.50}$ and $YBa_2Cu_3O_{6.25}$. In accordance with experimental evidence, we have generated structures with alternating filled and empty chains consistent with each stoichiometry [261]. The computed spectra qualitatively reproduce the experimental trends (see figure 6.4(a)).

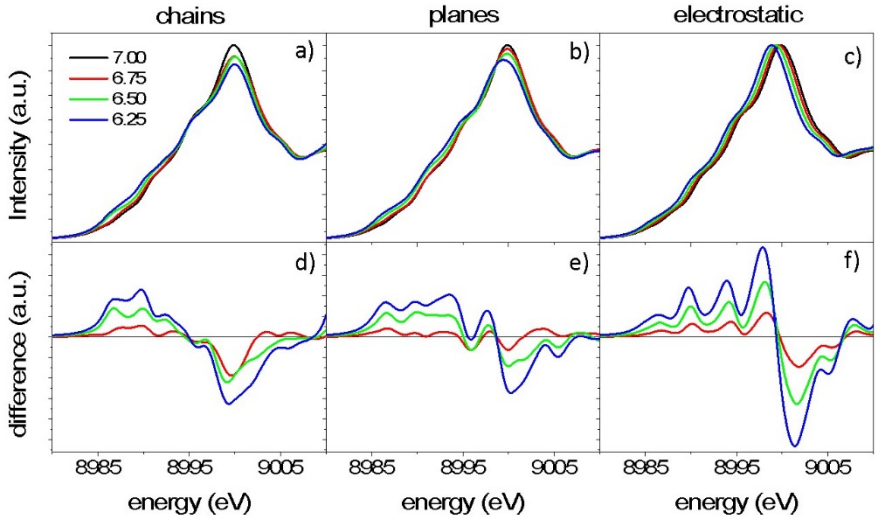

Figure 6.4. a) Calculated NEXAFS spectra of YBCO with oxygen stoichiometries corresponding to 7, 6.75, 6.5 and 6.25 (black, red, green, and blue) when the oxygen vacancies are exclusively generated in the CuO_X chains. b) Calculated NEXAFS spectra of YBCO for the same stoichiometries used in a) but with the oxygen vacancies generated exclusively in the CuO2 planes. c) Calculated NEXAFS spectra of YBCO when the compound is electrostatically charged with 0 (7), 0.25 (6.75), 0.5 (6.5) and 0.75 (6.25) electrons per unit cell (corresponding oxygen stoichiometry). Figures d), e) and f) show the intensity difference between the calculated spectra for YBCO with oxygen stoichiometries 6.75, 6.5 and 6.25 and the calculated spectra of YBCO with oxygen stoichiometry 7 for the different cases of study. Note that all the panels of this figure use the same color code as the ones displayed in a) and d).

Oxygen removal from the CuO_2 planes was also considered and ruled out. The simulations shown in figure 6.4(b) were carried out by removing oxygen from the CuO_2 planes up to the same oxygen concentrations considered for the vacancies in the chains. A significant shift of the whole pre-edge region to lower energies is predicted but was not observed in the experimental spectra. The spectral changes are also characterized by a redshift of the white line with decreasing oxygen content, also not found in the experimental data.

Pure electrostatic doping where the YBCO is electron doped in a fashion similar to that expected for a classical field effect transistor can also be ruled out (see figure 6.4c). Different spectra were simulated by adding electrons to match the

carrier concentrations corresponding to the oxygen stoichiometries. The resulting spectra exhibit a rigid shift to lower energy due to the increase of the energy of the Fermi level. There are no other changes in the shape, which is at variance with the more complex spectral changes observed in the experimental spectra discussed previously.

Only the modification of the pre- and main edge computed for oxygen removal from the chains and shown in figure 6.4(a) are similar to those observed in the gating experiments (figure 6.2(b)).

5 Ligand field molecular orbital theory

The observed evolution of the spectral features reflects a change in the local electronic structure around the Cu atoms that can be understood using ligand field molecular orbital theory. For $YBa_2Cu_3O_7$, the pre-edge feature of the K-edge XANES spectrum corresponds to non-bonding $4p_x$ states of Cu atoms within the chains. The main edge feature arises from antibonding states between Cu (at the chains $4p_y$ and the superconducting planes $4p_{x,y}$) and $2p_{x,y}$ O atoms. In absence of vacancies, the $4p_y$ orbitals of the Cu atoms in the Cu-O-Cu chains, along the y direction, hybridize with the $2p_y$ O states to form occupied sigma bonding, not probed here, and unoccupied σ^* antibonding states (see figure 6.5(a)). As O vacancies are created within the chains the Cu ligand field changes from square planar (see figure 6.5(a)) to linear (see figure 6.5(b)), yielding an intensity increase of the pre-edge feature due to allowed transitions to non-bonding $4p_y$ Cu states (see figure 6.4(c)). Spectral weight is thus transferred from the white line to the pre-edge region. The blue and red lines of figure 6.5(c) represent integrated intensity measured at V_G=0 V and 10 V respectively that supports the formation of oxygen vacancies in the Cu chains.

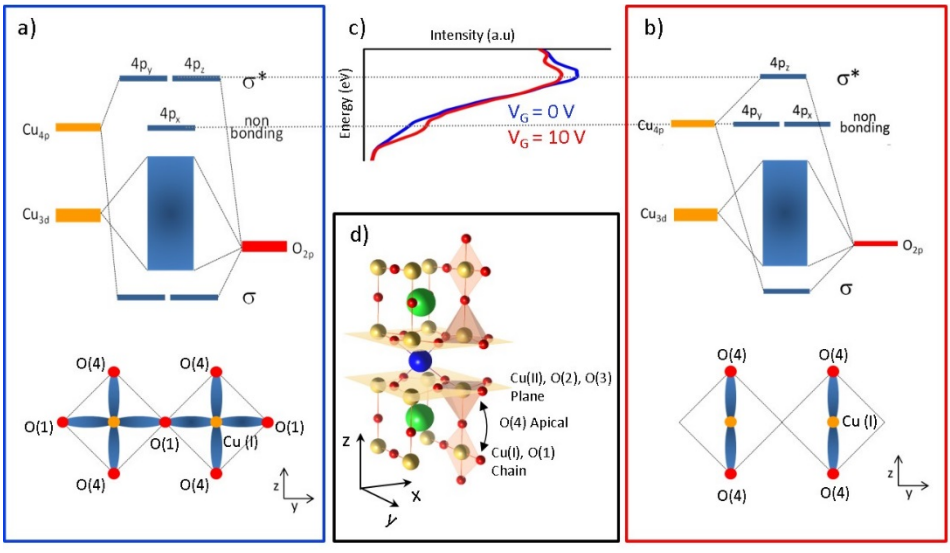

Figure 6.5. Schematic representation of the hybridized molecular orbitals for the two extreme compounds of the YBCO series: $YBa_2Cu_3O_7$ (a), $YBa_2Cu_3O_6$ (b). The Cu coordination in the yz plane of the CuO_X chain structure is also represented. (c) NEXAFS experimental data obtained with a voltage gate of 0 V (blue line) and 10 V (red line) shows the spectral weight transfer from the main edge feature to the pre-edge in agreement with the formation of oxygen vacancies in the Cu chains. d) YBCO crystallographic structure with the Cu, O, Ba and Y represented with the yellow, red, green and blue colors respectively. The coordination polyhedra of the CuO_X chains planes (top and bottom) and the superconducting CuO_2 planes (middle) are highlighted as well as the superconducting CuO_2 planes. The black arrow illustrates the intra unit cell charge transfer process between the CuO_X chains and the superconducting CuO_2 planes.

Therefore, our results are a spectroscopic evidence of chemical changes within the YBCO unit cell (see sketch 6.5(d)) occurring during the doping process with ionic liquids. The changes in the Cu coordination and consequently in the electronic structure of YBCO indicate oxygen migration under the strong electric field developed at the double layer. Oxygen migration from the CuO_x chains is not unrealistic and it has been shown to occur in cuprates at moderate temperatures under weak electric fields [262, 263]. The strong electric field developing at the double layer is expected to lower the structural barriers for ion motion and generate oxygen vacancies by electromigration.

6 Conclusions

In this chapter the superconductor to insulator transition of YBCO by means of the EDL technique has been studied realizing an in-situ experiment measuring hard x-ray absorption spectroscopy while doping.

It was found a spectral weight transfer between the main edge and the pre-edge of the Cu K-edge that is produced during the gating process. The systematically increase in the pre-edge line is associated with a reduction in the Cu coordination of the CuO chains while the decrease in the intensity of the white line is a signature of the superconducting planes. The spectral changes found at the absorption edges arise from oxygen depletion of the CuO_x chains as it was confirmed by Density Functional Theory (DFT) simulations. The charge transfer between CuO_2 planes and CuO_X chains yielding superconducting planes is therefore hindered and the superconductivity suppressed.

This chapter evidences that doping mechanism behind the EDL technique in the YBCO has primordial electromigration character that cannot be neglected. The generation of oxygen vacancies by electromigration shows the potential of gating with ionic liquids as a powerful tool for the controlled generation of oxygen vacancies in oxides and thus it signals, a path to a new degree of freedom in future oxide electronics devices exploiting phase changes associated to this doping strategy.

CHAPTER 7

IL-doping of heterogeneous systems: adding an intermediate layer between the IL and the YBCO

1 Motivation

To further verify the scenario of generation of oxygen vacancies by electromigration, two different gating experiments have been carried out introducing insulating interlayers (either Al_2O_3 and $PrBa_2Cu_3O_7$ (PBCO)) between the YBCO and the ionic liquid [264] (see Figure 7.1(a)). These materials have very different permeability to oxygen ions, which allows for the examination of the role of oxygen out-diffusion from the sample during the doping process. If doping by electrostatics were dominant, we would expect small or no changes in the electric properties of YBCO. If doping were the result of the presence of electromigration of oxygen, we would expect a much stronger doping effect in the case of the PBCO interlayer, more permeable to oxygen ions.

To understand de evolution of the T_c an analysis of resistance curves in terms of the empirical Matthiessen rule has also been carried out in this chapter for sample with both ALO and PBCO interlayers. This analysis underscores the role of the electrical disorder underlying doping in depressing the critical temperature.

2 Al_2O_3 (ALO) and $PrBa_2Cu_3O_7$ (PBCO) interlayer

In the first case we have used a 2 nm nanocrystaline Al_2O_3 (ALO) interlayer between the superconductor and the IL, which acts as a diffusion barrier for oxygen protecting the superconductor from chemical reactions at the interface and

excluding the oxygen to go out of the sample. As shown in figure 7.1(b), there is a slight modification of the T_c of less than 15 K for gate voltages up to 1.8 V without any alteration of the normal resistance. By further increasing the gate voltages up to 4 V, there is no noticeable changes in the R(T) curves of the ALO/YBCO device.

In the second case (see figure 7.1(c)), we have used a 2 u.c. $PrBa_2Cu_3O_7$ (PBCO) interlayer. PBCO is isostructural to YBCO, which allows oxygen diffusion into the layer facilitating oxygen migration. Interestingly, in this case the change of the critical temperature for the same 1.8 V is very pronounced (more than 50 K), in addition there is an increase in the sheet resistance and the measured curves resemble those of deoxygenated YBCO [106].

XAS measurements done with the ALO interlayer in the synchrotron (following the process explain in Chapter 6) confirmed no oxygen migration (see Figure 7.2). XAS spectra were only possible to be measured at two voltages (0 and -1V) showing no change in the white line (associated with the superconductor planes) nor in the prepeak (associated with the coordination of the Cu in the chains). This further supports that the amorphous ALO is acting as a physical barrier preventing oxygen diffusion out of the sample.

The slight decrease in the Tc is therefore associated with a purely electrostatic doping. Interestingly it occurs independently of the sign of the applied voltage: Tc decreases no matter the voltage sign (as will be discussed later).

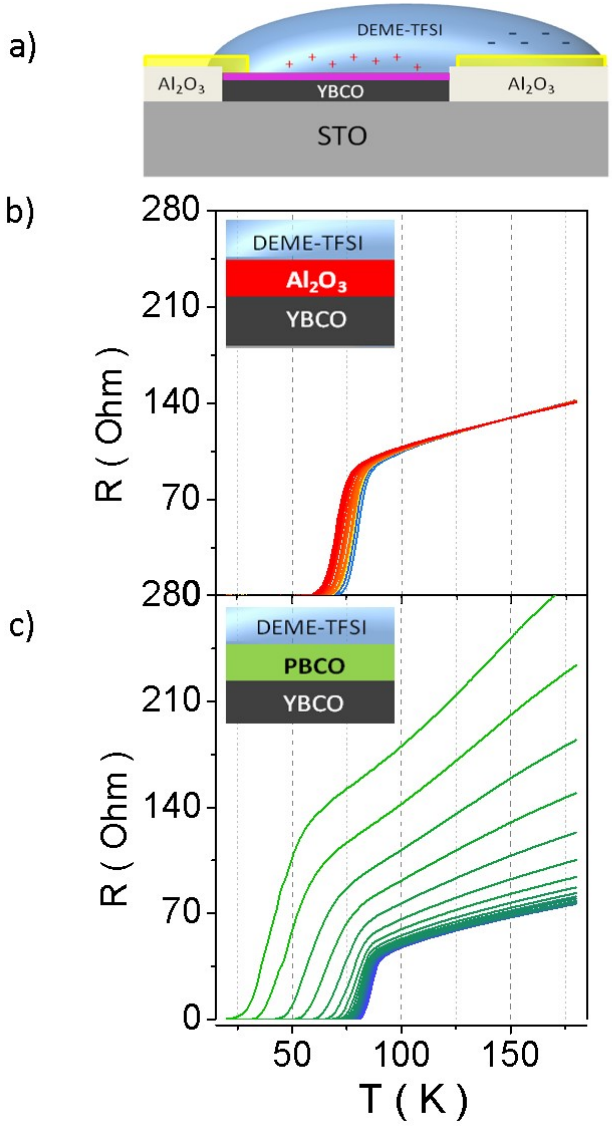

Figure 7.1 a) Schematic structure and resistance-temperature measurements of the electric-double-layer field-effect transistor of YBCO with an interlayer. Schematic representation of the gating device showing the configuration with an interlayer between the YBCO and the Ionic liquid. Figures b) and c) show resistance versus temperature curves measured at different gate voltages (from 0 V to 1.8V) when the interlayer is amorphous Al_2O_3 and isostructural PBCO respectively. While the amorphous Al_2O_3 is acting as a physical barrier preventing oxygen diffusion, the PBCO interlayer acts as an oxygen reservoir allowing oxygen migration from the YBCO. Figure c) shows a similar behavior of the resistance versus temperature curves of deoxygenated YBCO samples.

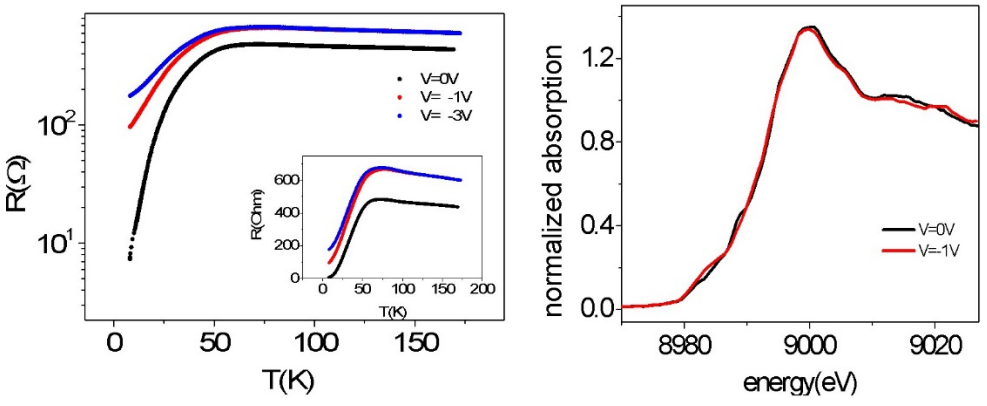

Figure 7.2. b) Resistance versus temperature for different applied negative V_g and its XAS spectra respectively.

In the following sections an empirical analysis using the Matthiessen rule has been carried out in order to understand the influence of the scattering disorder on the evolution of the T_C , for samples with both types of interlayers.

3 Evolution of the Tc with the Al_2O_3 (ALO) interlayer

3.1 Applied cycle of V_G

Figure 7.3 and Figure 7.4 show the evolution of the T_c in the case of samples with ALO interlayer. Initially, a slight decrease of the T_C was induced with positive applied gate voltages, associated with an electrostatic doping contribution occurring through the ALO physical barrier. The influence of the polarization temperatures, T_{pol}, has also been studied and it was found to be associated to an enhancement of the T_C.

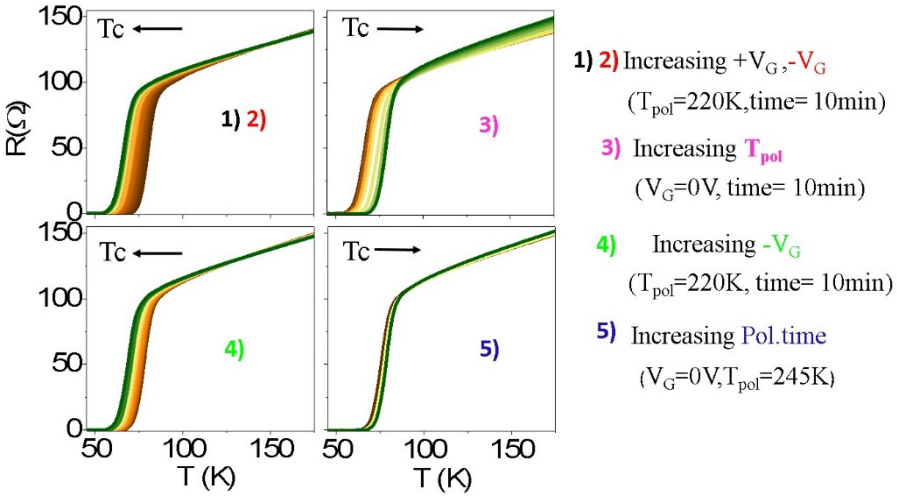

Figure 7.3: Resistance versus temperature for different applied voltages. Region 1) 2) positive and negative V_g respectively; there is a decreasing of the T_c. Region 3) shows an increase of the T_c as the T_{pol} is also increases at V=0 bringing the system to the initial T_c. Region 4) 5) negative and positive V_g makes the T_c to decrease again. 6) The Tc increases with the polarization time at T_{pol}=245K.

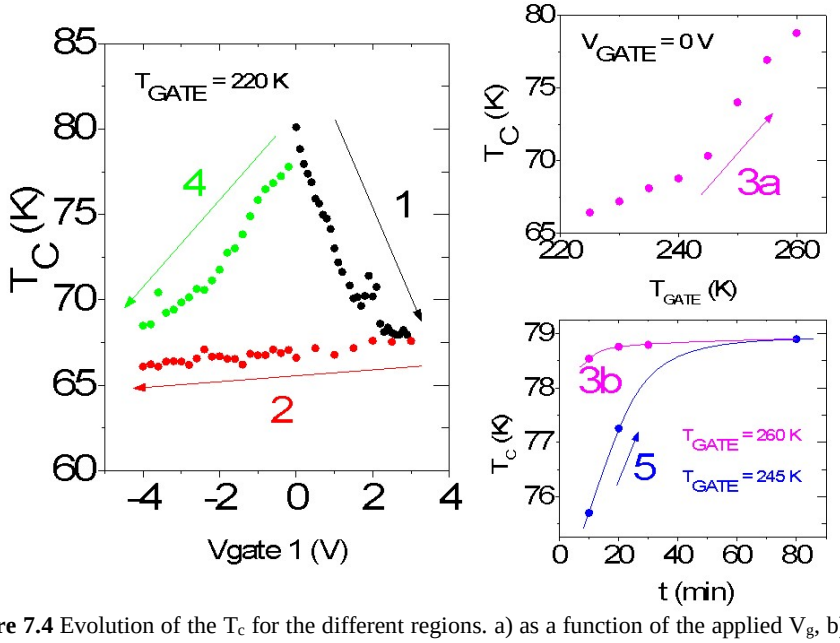

Figure 7.4 Evolution of the T_c for the different regions. a) as a function of the applied V_g, b) as the T_{pol} is increased, c) as a function of the polarization time.

Figure 7.4 shows the evolution of the T_C for positive applied V_G at T_{pol}=220K and applied during 10 minutes (the region 1)). A slight modification of the T_c of less than 15 K for gate voltages up to 1.8 V was found without much alteration of the normal state resistance. Figure 7.5(a) shows the current leakage curves in this region exhibiting some oscillations up to 1.2V. For higher voltages the leakage current drops to 0 indicating that the polarization process in not taking place. This shows that regime 2 characterized by a T_c independent of the gating voltage is in fact due to the absence of the charging peak which denounces a sort of quenching of the doping process. It has to be noticed that this quenching is not released by further increasing the gate voltages up to 4V, upon which no noticeable changes in the R(T) curves were observed.

No threshold V_g was needed for the T_c to start to drop, what makes us think that this process is associated with the first-step doping process which is just a purely electrostatic mechanism modulating the Tc with the accumulation of the screening charges of the YBCO at the interface. ALO is insulating and thus strongly decrease the magnitude of the electric field at the YBCO surface.

As the voltage is increased the resistance does not change significantly exhibiting a slight inversion of the trend displayed by the slope of R(T) curves with voltage.

To look at the reversibility of the process, decreasing positive voltages (region 2 of Figure 7.4) have been applied continuing into negative values. Tc does not change and exhibits a voltage independent quenching of the doping process described above. In this quenching condition, T_c remains at this value even though negative voltage up to -4V are applied. This suggests that the doping process after the application of large voltages produces irreversible changes in the double layer. This changes can be chemical modifications (electric field driven) or simply a stability condition of the IL (due to the different ions sizes) which need excess energy supply to break it.

The temperature plays an interesting role. It was found that an increase of the polarization temperature, T_{pol}, of the IL makes it possible to recover the original conditions of the IL and the polarization system (see region 3(a) in Figure 7.4). At V_g=0 an enhancement of the T_c was measured when increasing polarization temperatures starting at 220K up to 260K. A linear parallel behavior in the R(T) is shown in this region and an increase in the normal resistance R_n takes place. While

polarization temperature is increased the leakage current remain at 0 value up to 245K where a negative polarization peak is recorded associated with the discharging process. At T_{pol}=260K, keeping V_g=0V, the system was allowed to discharge for longer time 10, 20 and 30min (region 3(b) in Figure 7.4) and the initial critical temperature was recovered.

Region 4) of Figure 7.4 shows the negative V_g applied from – 0.2V to -4V each ΔV= -0.2V. A decrease in the T_c was found up to certain voltage. R(T) curves resembles the ones in region 1), showing again slight inversion of the trend of the voltage dependent R(T) slope. Figure 7.5(b) shows the leakage current curves in this region exhibiting some oscillations up to -1V. For higher negative voltages the leakage current drops to 0 indicating that the polarization process in not taking place showing an absence of the charging peak which explains the quenching of the doping process.

It is necessary to increase the temperature (region 5 of Figure 7.4) recover the polarization peak in the current leakage curves. Aiming at an enhancement of the T_c, the polarization temperature was increased up to at 245 K with V_g =0V for (region 5). The value of 245K was chosen as the starting temperature of the discharging process. Keeping the system at this temperature for different polarization times 10, 20 and 80min the T_c was reversed and the initial value is reached.

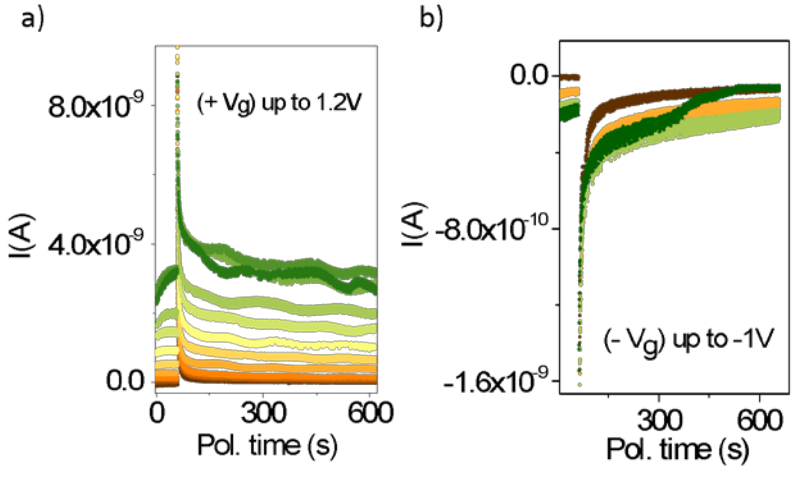

Figure 7.5 Current leakage curves for regions 1) and 4) up to a certain voltage

In summary, the ALO interlayer acts as a physical barrier to avoid the oxygen migration associated to IL doping. The mechanism behind the YBCO doping through the ALO interlayer has a purely electrostatic character and the system is not allowed to go to low Tc values, even for high applied voltages, where it was found a quenching of the doping process. The slight decrease measured in the Tc is due to the electrostatic screening of the charges to the electric field confirming that the doping with EDLT devices is a two-step doping process governed by the oxygen migration. The polarization temperature plays a key role making the system to go back to its initial value when it is increased, suggesting that additional energy has to be supplied to reverse the quenching of the double layer.

3.2 Quantification of the electrical disorder using Matthiessen rule

A quantitative analysis of the electrical disorder and its evolution with the Tc and the applied voltage cycle using the empirical Matthiessen rule and the equations (3-5) of the Chapter 5 has been conducted.

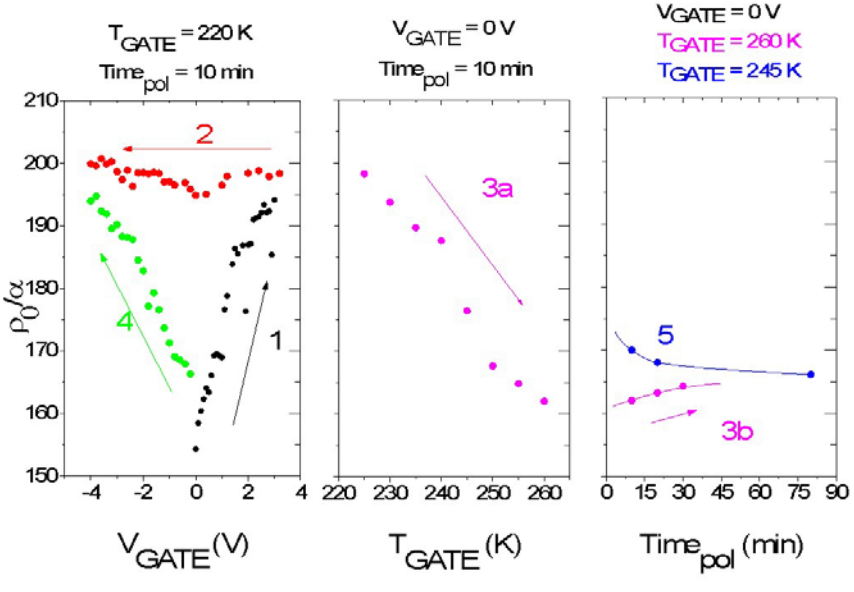

Figure 7.6: Evolution of $\frac{\rho_0}{\alpha}$, proportional to the electrical disorder for the different regions

An increase in the electrical disorder, $\frac{\rho_0}{\alpha}$, was found (see Figure 7.6) independently of the sign of the applied voltage (regions 1 and 4). This suggests

that the modulation of the T_c in these two regimes involves the generation of disorder. In regime 3) along with an enhancement of the T_c a decrease of $\frac{\rho_0}{\alpha}$ was observed. It is clearly seen that the polarization temperature plays a role in restoring the system to the initial disorder state.

Two different mechanisms can be invoked to explain the effect of the disorder in the superconductor properties:

Localization of carriers: The disorder can determine the number of charge carriers that are going that contribute to the superconductivity due to a phenomenon of localization. This phenomenon of localization is produced by the introduction of a random mofication of the lattice potential and triggers a continuous transition from a metallic to an insulating state [265].

Pair braking: Pair braking due to the electrical disorder.

The excess of charge carriers introduced in the double layer are generated to screen an intense electric field. The strongly interacting electrons may give raise to fluctuations of the local electric field due to incomplete and or inhomogeneous screening of the electric field locally. Local fluctuations of the electric field act as strong scattering center providing and additional scenario for the induced scattering in presence of gating.

The evolution of the parameter $\frac{1}{\alpha}$ has also been estimated and behaves in the same way as the electrical disorder as is plotted in Figure 7.7. This indicates that both parameters are correlated and the variable $\frac{1}{\alpha}$ cannot be associated as in a normal metal with the number of charge carriers.

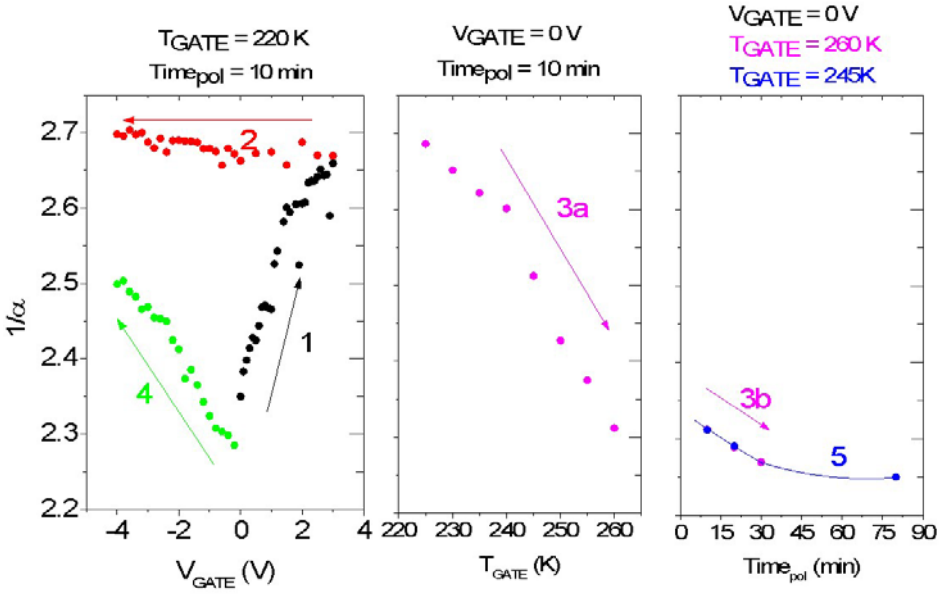

Figure 7.7: Evolution of $\frac{1}{\alpha}$, proportional to number of carriers for the different regions.

This term is supposed to be temperature independent, $\alpha = \frac{m*}{ne^2}A$. However, in cuprate superconductors the parameter A is non-linear and it has been previously considered that the coefficient of the linear resistivity goes to zero, A→0, at the same doping as T_c→0 [266]. The remarkable correlation between linear resistivity and Tc has been associated with a common origin between the anomalous (non-Fermi-liquid) scattering and pairing in cuprates [266]. The increase of $\frac{1}{\alpha}$ as the Tc decreases found, independently of the sign of the gate voltage in addition with the obtained increase in the electrical disorder shows this direct empirical correlation and strongly supports this common origin.

The evolution of the Tc in relation to the electrical disorder $\frac{\rho_0}{\alpha}$, the parameter $\frac{1}{\alpha}$, and the residual resistance in the metallic state (ρ_0) is summarized in Figure 7.8 Extrapolating to 90K, the disorder does not go to cero, as would be expected for a completely oxygenated thin film and free of defects. This can be associated to the fact that the samples used are just 3 u.c thick and some disorder aside from some

oxygen deficiency can be expected. The fact that the disorder parameter recovers its initial value suggest its electronic origin.

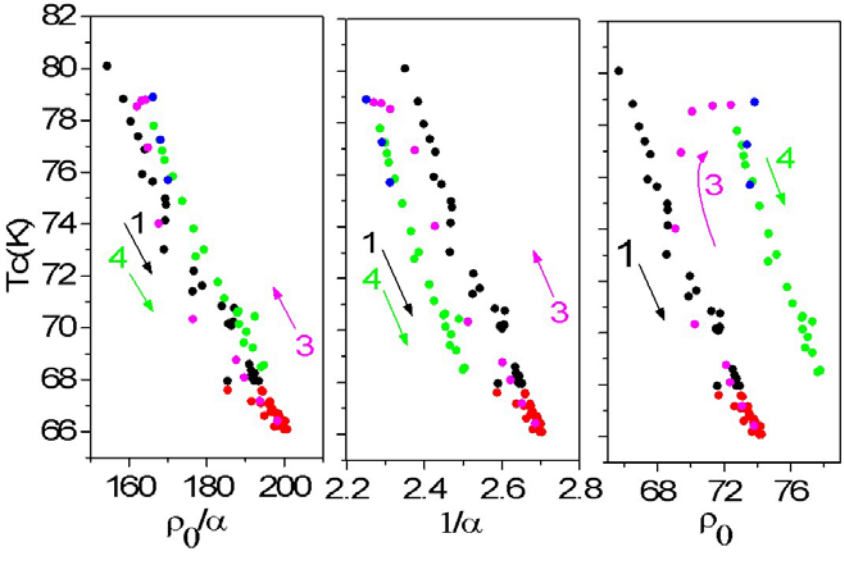

Figure 7.8 Evolution of the T_c, with the parameters connected with the disorder, the number of carriers and the residual resistance.

Similar experiments have been done starting either with negative or positive applied gate voltages, V_g, and no changes in the results were observed. This confirms that the sequence of changes of the sign of the gating voltage has no effect showing an increase in the electrical disorder independently of the sign of the applied voltage.

4 Evolution of the Tc with the PBCO interlayer

4.1 Applied cycle of V_G

The isostructural PBCO allows the oxygen diffusion through the sample but protects the YBCO from electrochemical reactions. In the Figure 7.9 the critical temperature dependence with the applied voltage is represented showing two

different regions evidencing the two-steps doping process. The Tc slowly decreases each 0.2V for low voltages exhibiting a linear dependence up to a threshold voltage, 1V. This first region is associated with the purely electrostatic mechanism due to the screening charges to the applied electric field what is basically the same mechanism that was found in the ALO interlayer. The PBCO layer allows oxygen diffusion across it so we can talk about a second doping step, which governs the doping, associated with a migration process that has been activated. This results in an abrupt decrease of the Tc and the appearance non-linear (pseudo) gap features in the resistance versus temperature curves characteristic of deoxygenated samples.

All the measurements have been done at T_{pol}=220K and the voltage applied during 10 minutes. To study the reversibility of the process, it was decided to do not allow the system to go to the insulating phase and at a certain voltage of 1.8 V, decreasing V_g were applied going into negative values. The T_c modulation is nonvolatile, namely, the T_c remains at this value even though negative voltages are applied. We checked the ionic liquid to operate properly displaying well behaved charging curves, what discards quenching of the double layer observed previously at high voltages in samples with ALO interlayers. The absence of Tc change with negative voltages is consistent with the removal of oxygen from the YBCO which only occurs with positive voltages.

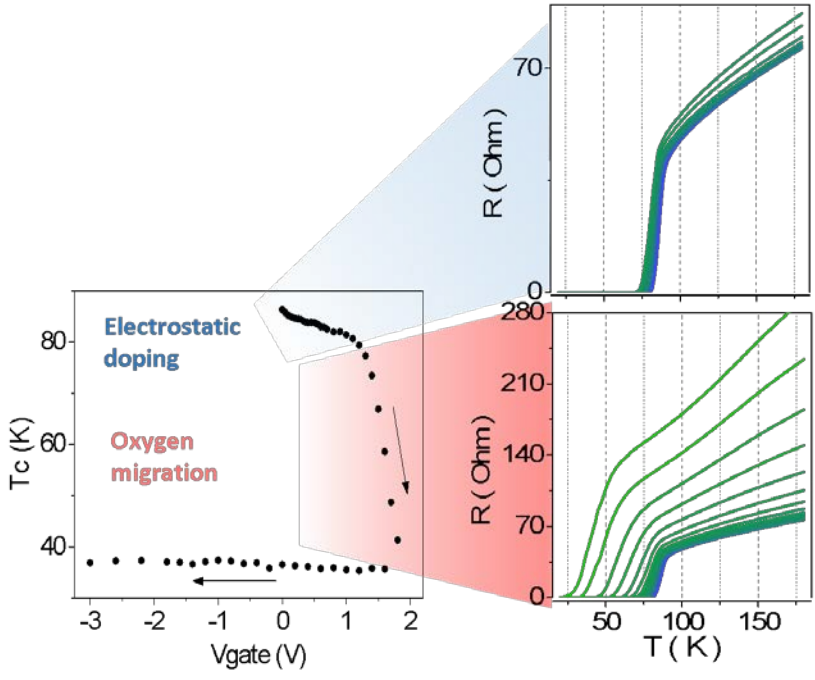

Figure 7.9. a) Evolution of the Tc for the different applied voltages and the correspondence resistance versus temperature curves.

Looking at the reversibility of the process, the polarization temperature of the system was increased up to 260K with V=0V obtaining the expected enhancement of the T_c up to 70K, even though the initial value was not reached (see red curve in Figure 7.10). The PBCO interlayer is acting as an oxygen reservoir allowing the system to recover its initial state as the temperature in increased restoring the leaked oxygen ions to the YBCO.

Finally, the system was driven to room temperature and the IL removed using isopropanol (see blue curve in Figure 7.10). The R(T) shows an onset of the T_c similar to the initial state of the sample even though the transition is not so abrupt. Despite the PBCO capping layer is protecting the YBCO, some increase of the R_n, probably associated to some damage in the sample is observed.

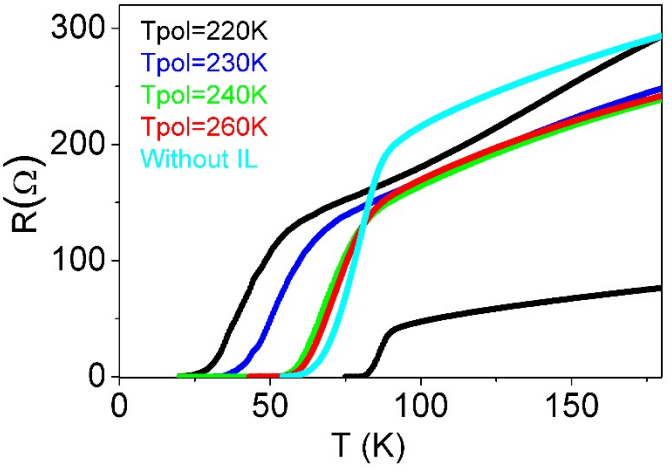

Figure 7.10. Resistance versus temperature curves for different regions at different T_{pol} and for the sample without the IL. The T_c increases as it is increased the T_{pol}.

4.2 Quantitatively analysis of scattering disorder using Matthiessen rule

A quantitative evaluation of the scattering disorder using the Matthiessen rule has been done for the first region (positive V_g) of the PBCO interlayer experiment. Making use of expressions (3-5) of the chapter 5 we have found the evolution of the scattering disorder displayed in Figure 7.11

The modulation of the T_c with gating can be analyzed in the previously mentioned two-steps doping process. There is a threshold voltage (up to 1V) for which the T_c decreases linearly with the applied gate voltage, and the electrical disorder increases slightly, in a similar fashion to the case of the ALO capping. This regime would be associated with a purely electrostatic mechanism. However, above the threshold voltage the second doping step triggers an abrupt parabolic decrease of the electrical disorder parameter. The suppression of the disorder for large doping levels is probably associated to the opening of the (pseudo) gap in the spectrum of low energy spin and charge excitations which are known to play a leading role in the scattering mechanism of cuprates.

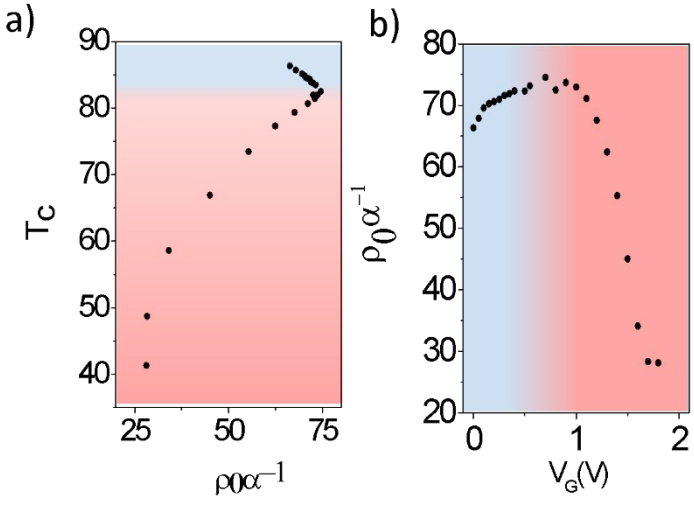

Figure 7.11. a) Evolution of the T_c, with electrical disorder. b) Evolution of the electrical disorder as function of the applied V_g. Blue region associated with a pure electrostatic mechanism and pink region with an oxygen migration process.

Figure 7.12 shows the relative modulation of the critical temperature, ΔTc, as a function of the relative change of the scattering disorder parameter, $\Delta(\frac{\rho_0}{\alpha})$ for both the ALO and the PBCO interlayer. In the first-step process there is an increase in the electrical disorder for both cases associated with a purely electrostatic mechanism. The alumina is acting as a physical barrier not allowing the oxygen to go out of the sample, so the electrical disorder keeps increasing as it increases the screening charges.

In the case of the PBCO both mechanisms are involved, an increase of the scattering disorder occurs first resulting from the inhomogeneous screening of the electric field, followed by an activation of the oxygen migration process which encompasses a decrease of the scattering disorder (probably as a result of the opening of the pseudogap).

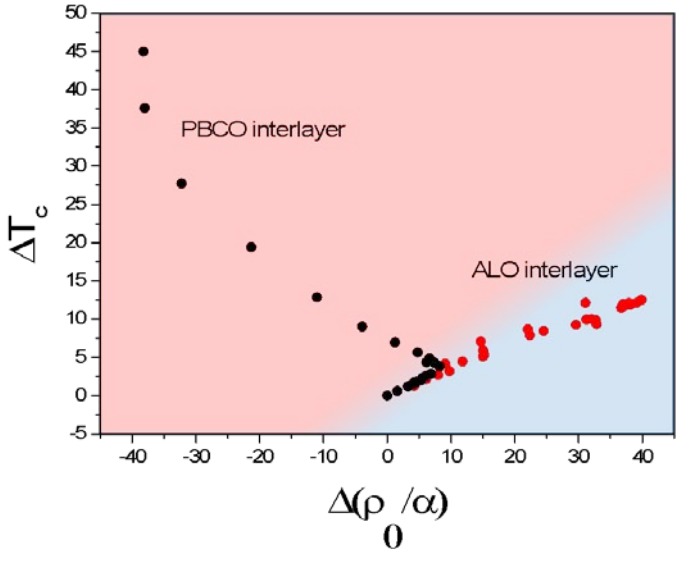

Figure 7.12. Modulation of the critical temperature, ΔTc, as a function of the relative disorder experimented, $\Delta(\frac{\rho_0}{\alpha})$ for both the ALO and the PBCO interlayer. Blue region associated with a pure electrostatic mechanism and pink region with an oxygen migration process.

5 Conclusions

The results obtained in this chapter confirm that the dominant contribution to the doping of the YBCO using ionic liquids has a chemical origin and arises from the electromigration of oxygen ions from the CuO_x chains.

Experiments using intermediate layers acting as oxygen barriers and oxygen reservoirs indicate that the effect of the large electric field at the interface between the ionic liquid and the YBCO triggers a doping process in two-steps. One due to the electrostatic screening with the additional contribution of the effect of scattering disorder on Tc and a second step above a certain voltage which induces the electromigration of oxygen ions from the CuO_x chains and governs the doping process.

The temperature plays a key role by making the oxygen to go back to its initial position allowing the system to recover the initial Tc in accordance of Chapter 5 as long as the superconductor-insulator transition is not crossed.

The present experiment, shows the potential of gating with ionic liquids as a powerful tool for the controlled generation of oxygen vacancies in oxides and thus a path to future oxide electronics devices exploiting phase changes associated to this doping strategy.

CHAPTER 8

In- situ impedance spectroscopy measurements

1. Motivation

To fully understand the doping mechanism behind EDLT it is important to study the electronic and electrochemical interaction between the ionic liquid and the oxide interface, characteristic of these novel devices.

There have been reports on the instability of $YBa_2Cu_3O_{7\_x}$ interfaced to ionic liquids under external bias [267]. The instability is often inferred from irreversible change in channel resistance or a morphology change of channel surface. However, in recent years, direct methods to characterize electrochemical reactions have been developed as it is the impedance spectroscopy technique, as already mentioned in the experimental chapter. The first report of electrochemical impedance spectroscopy (EIS) of EDLT represented as the spectra of the phase angle (θ) identified the fundamental processes in the EDL formation, appearing as an ideal technique to evaluate the electrostatic or electrochemical nature of EDL interface [242].

In this chapter we investigated the charging dynamics and the charge accumulation of ionic-liquid/YBCO EDL interfaces in the transistor configuration. Capacitance (*C-f*), and conductance *(G-f)* data as a function of the external gate voltage was recorded at different temperatures providing us information on the mechanism behind the EDL interface formation and the characteristic evolution of the double layer as the doping process is carried on [268–270].

2. EDL formation in ILs.

The interface between an ionic liquid and a metal electrode is a complex problem which is still the subject of much study [271]. In the following we take a simplified approach that allows us to understand the doping process going on in the surface of the electrode, YBCO in our case.

The EDL of the highly concentrated ILs cannot be described by theories developed for dilute solutions, such as Gouy-Chapman (see Figure 8.1(a) and (b)). At the vicinity of an electrified interface, the distribution of ions with the same sign (i.e., anions or cations) and the thickness of EDL depend on the electrode charge potential. In the case of IL with a large cation-anion pair, all of the ions that deliver the full countercharge to compensate the charge density of the electrode do not have room in the nearest single layer of the electrode because of their bulky size. In this situation, the rest of the ions required to compensate the electrode charge density completely reside in the next consecutive layers (see Figure 1(c)). This is known as “lattice saturation” [272, 273].

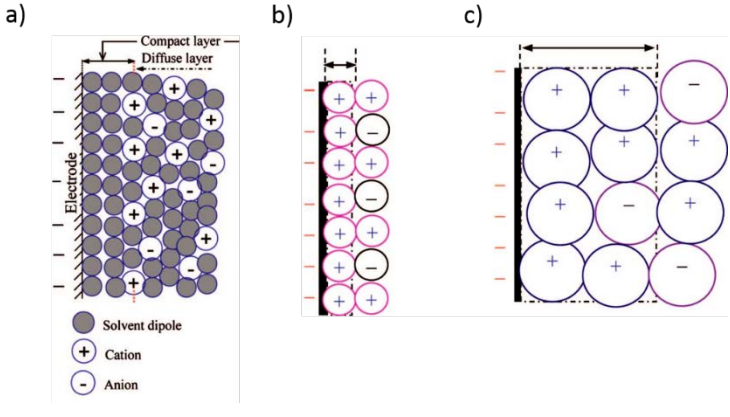

Figure 8.1. Schematic diagrams of EDL structures and *C-E* curves in conventional solution containing solvent dipole and electrolyte (a) and IL (b and c), where the electrode is considered to be negatively polarized. Panels (b) and (c) represents the distribution of small and large ions, respectively.

Thus, at a particular potential, the thickness of EDL (Figure 8.1(c)) and hence the absolute value of *C* would be expected to depend on the characteristics of ILs, that

is, the size of ions and the parameter γ (associated with the degree of incompressibility of the IL).

The double layer is hence composed by more than one layer of ions with same/different signs (i.e., cations or/and anions) arranged in proportion to the charge density of the electrode. The overall capacitance (i.e., C_{dl}) of such an EDL in ILs may be expressed as the sum of reciprocal of the inner or compact layer, C_c , (or Helmholtz layer, see Figure 8.1(b)) and diffuse layer, C_d, capacitances :

$$\frac{1}{C_{dl}} = \frac{1}{C_c} + \frac{1}{C_d} \tag{1}$$

$$C_c = \frac{\varepsilon^*}{4\pi d} \tag{2}$$

$$C_d = C_D \times \frac{cosh\left(\frac{u}{2}\right)}{1+2\gamma sinh^2\left(\frac{u}{2}\right)} \times \sqrt{\frac{2\gamma sinh^2\left(\frac{u}{2}\right)}{\ln[1+2\gamma sinh^2\left(\frac{u}{2}\right)]}} \tag{3}$$

where C_c and C_d signify the compact and diffuse layer capacitances, respectively. $C_D = \varepsilon/4\pi L_D$, and L_D is the Debye length. The ε^*, ε, and d represent the effective dielectric constant of the compact layer, the high-frequency dielectric constant of the IL, and the distance of the closest approach of ions to the electrode, respectively and $u = e\Phi/k_BT$, where Φ is the total potential drop across the EDL and the value of $(k_B \times T/e)$ is 25.69 mV at 25 ºC [272]; the parameter $\gamma = 2c_0/c_{max}$, where c_0 is the average bulk number density of cations or anions and c_{max} is the maximal possible local concentration of ions (both cations and anions), respectively [274, 275].

In the EDLT configuration, the distance d between the ions and the electrodes is the proper size of the ions ($DEME^+$ and $TFSI^-$) allowing the parameter d to be as low as 1 nm. As a consequence, the capacitance of the compact layer (C_c) is going to be the one that governs the overall capacitance (C_{dl}). From now on, we will talk about the total capacitance of the EDL just as the Helmholtz layer, considering undistinguished C_{dl} and C_c.

3. Device configuration

To be able to measure accurately the capacitance and conductivity with the impedance spectroscopy technique a slightly different geometrical configuration has been used to dope the YBCO. The 3 u.c thick film was settled inside a glue glass cylinder contain the ionic liquid. In this out of plane configuration designed the gate electrode is an inert platinum coil situated at the top of the cylinder as is indicated in Figure 8.2. The EDL formation was probed by applying a DC gate voltage with an AC 20 mV signal superimposed, in the frequency range 10^{-2} - 10^{7} Hz. Nevertheless, at frequencies larger than 1 MHz, the Pt coil inductance becomes significant and data are not considered.

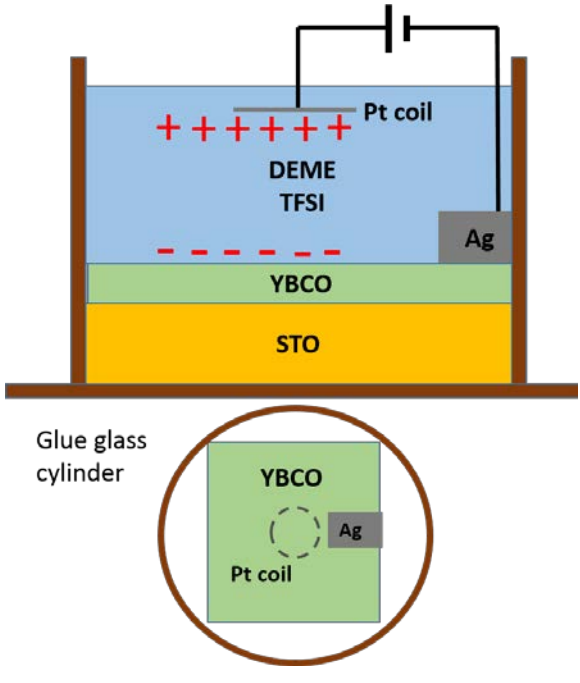

Figure 8.2 Scheme of the EDL device in the perpendicular configuration used to dope the YBCO and measure the impedance.

4. Charging Mechanisms of the EDL interface

The impedance data of the YBCO EDL device at 240 K is presented in Figure 8.3 in the tan(δ) representation. For the sake of clarity, data are shown progressively in three different ranges: 0 - 1 V panel a), 0 - 2.4 V panel b), and 0 - 3 V panel c), in 0.2 V steps. In figure 8.3 a) and b), the electric response shows three frequency regions well separated, as a consequence of the different contributions [242]. The main contribution to the tan(δ) is the bulk conductivity process of the ionic liquid, observed in the 1 - 10 kHz range, appearing as a pronounced maximum as a consequence of the capacitive behavior of the ionic liquid (phase angle 90º). At lower frequencies, around 3 Hz, another process is observed, this time as a shoulder instead of a maximum, indicating the capacitance contribution of the EDL formation. At the lowest frequencies, after a minimum around 10^{-1} Hz, there is another contribution which increases tan(δ), this is the final charge accumulation in the YBCO electrode. In this range we probe the interaction during the charging process between the ions of the IL and the YBCO electrode, becoming the critical region to differentiate the electrostatic and electrochemical nature of the doping processes. The frequency separation comes as a consequence of the value of the characteristic capacitance of each process, the bulk IL has a small capacitance, $C_{IL,}$ the EDL a larger value, and the electrode charge accumulation a still larger value, increasing the time constants proportionally.

Regarding the frequency dependence of each process, in Figure 8.3 (a) the bulk IL, the EDL and the YBCO electrode contribution are DC gate independent within experimental error in the range 0 - 1 V. A different scenario appears in panel b), where the region of the YBCO electrode contribution shows an evident DC gating dependence in the range 1 - 2.4 V. In Fig 8.c the YBCO electrode contribution is more steeply dependent on frequency in the gating range 2.4 - 3 V, in fact a maximum appear in the tan(δ) spectra, but also the EDL contribution is affected, decreasing its contribution from the value without gating.

To better understand the different mechanisms that affect the YBCO electrode in the gating process we analyze the low frequency measurements in the simultaneous conductance (G) and capacitance (C) representations in figure 8.4. We have also

divided the figure in three panels a), b) and c) with the same voltage ranges as in Figure 8.3.

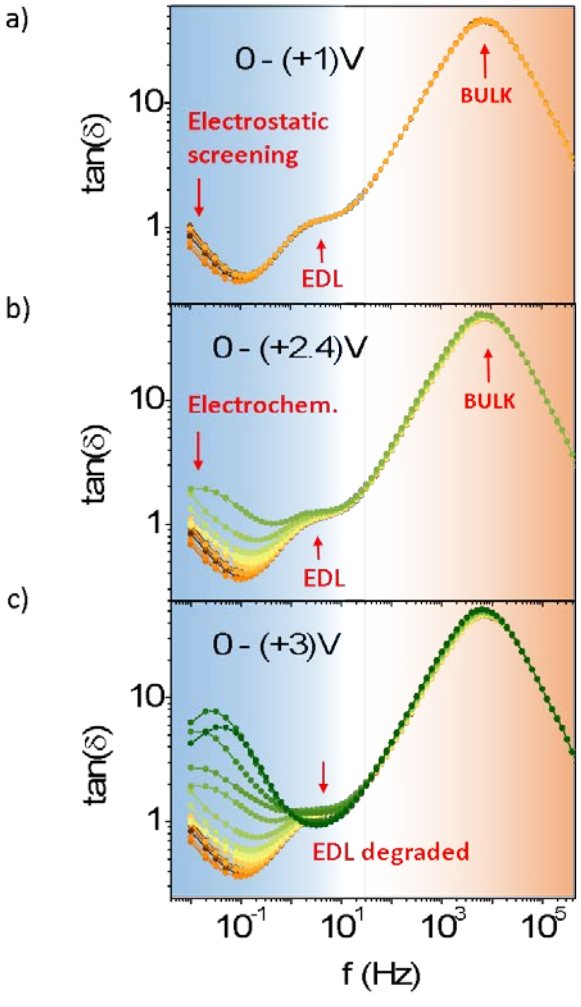

Figure 8.3. Phase angle plots of the IL/YBCO system by impedance spectroscopy at 240 K under different DC bias. The shadowed blue area is dominated by the electric-double-layer capacitance at ionic liquid/YBCO interface, while the red part is dominated by ionic liquid's bulk capacitance.

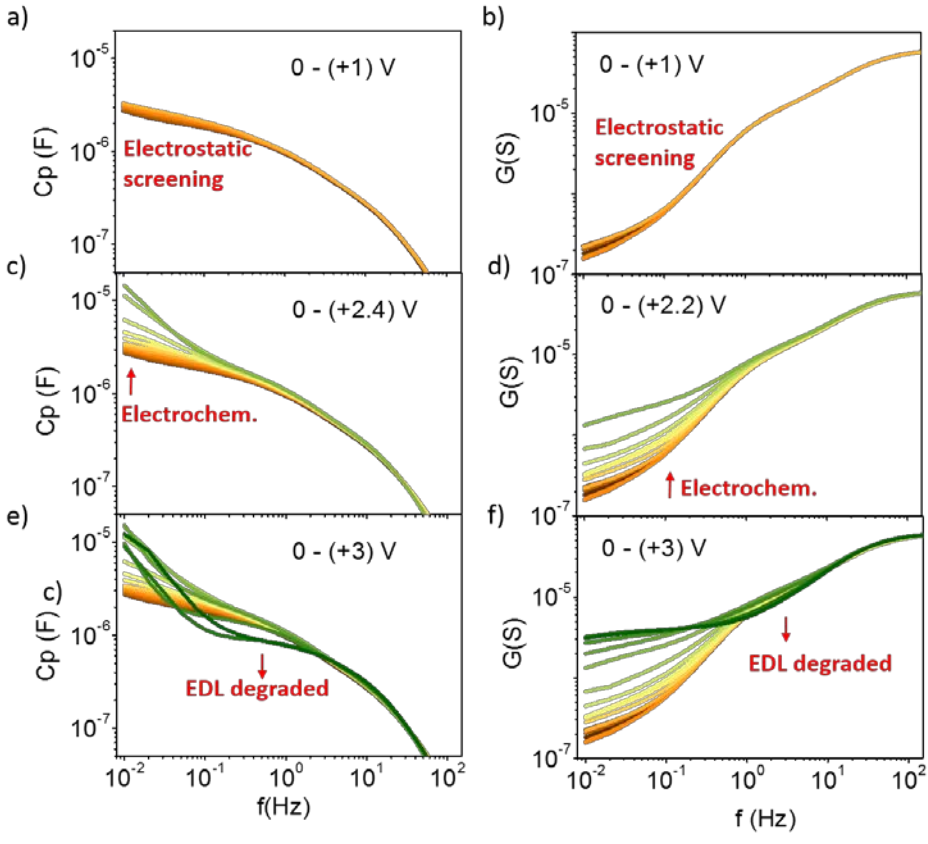

Figure 8.4. Capacitance and conductivity of the EDLT at 240 K, from 0 to 3 V, showing first an electrostatic contribution and then electrochemical reaction that ends up with the EDL degradation.

In figure 8.4(a) and (b), gating voltages from 0 - 1 V, we observe that there is no voltage dependence neither in the capacitance nor in the conductivity, as we have seen in the tand(δ). This is an indication that no charge is reaching the YBCO electrode (no conductivity increase), and therefore the charge accumulation is electrostatic, due to the screening of the gating voltage. Consequently, the gating mechanism of the YBCO in this voltage range is mainly electrostatic.

Figure 8.4(c) and d presents the voltage range 1 - 2.4 V. As we observe in the tan(δ) representation, both the capacitance and the conductance in the YBCO

electrode frequency region (below 1 Hz) display a strong V_G dependence. The capacitance shows an increase with the gating, which can be understood in terms of an electrochemical reaction taking place in the YBCO electrode, because Faradaic charges Q_F transferred through EDL interfaces in a surface redox process are a function of gate potential [242]. It is this variation with chemical origin that gives a so called pseudo-capacitance $C_{ech} = dQ_F/dV$, which we observe in figure 8.4(c) [276]. But in such a situation the YBCO electrode is not any more blocking all the carriers, since part of them are involved in the electrochemical reaction, and the conductance should sense the situation. Indeed in figure 8.4 (d) a progressive increase of the conductance is observed as increasing the gating in this second step. This electrochemical nature of the gating process in YBCO is in nice agreement with the XAS results presented in chapter 6.

The highest voltage range 2.4 - 3 V is shown in figure 8.4(e) and (f). Both the capacitance and the conductance are not showing any more the expected behavior, and the curves depend on frequency at higher frequencies, above 1 Hz, indicating that the EDL is being modified because of a very strong gating voltage, reaching the reversible limit of our device. We may speculate that the degradation of the double layer could be due to a re-ordination of the cation an anions layers at the IL interfaces promoted by the oxygen presence at the interface and the induced electrochemical reactions. If we consider the oxygen migration scenario, a recombination and charge transfer between the oxygen ions and the first layer cations would make the capacitance and the conductivity to decrease over a certain voltage.

6. Gating Reversibility

In order to check the reversibility of the gating effects we performed several gating cycles, for simplicity we analyze only the capacitance data, since the same information is present in the conductance spectra. The voltage was systematically increased as from 0 to 3V (see Figure 8.5 (a)) exhibiting the degradation of the double layer already explained in the previous section. Then the voltage was decreased Figure 8.5 (b) and negative values have been applied to complete the cycle Figure 8.5 (c) and (d). As we have also seen in the previous section, the capacitance shows two frequency separated contributions; one coming from the

double layer formation (at 0.3 Hz), C_{EDL}, and other with a chemical origin due to the electrochemical reactions in the interface at low frequencies, $C_{ech.}$

In the panel 8.5(b) as the voltage is removed after the EDL degradation, the chemical origin capacitance, C_{ech}, decreases abruptly for 2.8, 2.6 and 2.4 V indicating an abrupt decrease of the electrochemical reactions in the interface. However, for lower voltages it increases systematically again until the Vg is close to 0 where no changes are observed in the curves, meaning no voltage dependence and no reactions. These dynamics are associated with a systematic increasing of the C_{EDL} contribution as the voltage is removed. It indicates that as the voltage decrease the cations and anions of the IL are reoriented creating again the double layer and so increasing the capacitance.

When the system is driven to negative polarization bias, V_G, the two voltage ranges for the gating process found for positive voltages are expected, Figure 8.5(c). Low negative voltages exhibit a mainly electrostatic behavior showing a constant value of the capacitance for gating voltages down to -1 V. As the bias is decreased further than -1 V, electrochemical reactions are found at the lowest frequencies, showing again a voltage-dependence of the capacitance. However, in negative voltages, the systematic increase of the capacitance with the applied voltage is obtained for both, C_{EDL} and C_{ech} contribution. Based on our XAS results we can associate the presence of the electrochemical voltage dependence to the oxygen diffusion flow back to its initial positions inside the YBCO surface. It was seen in Chapter 5 that, as soon as the superconductor-insulator transition is not crossed, negative V_G will make the T_C to increase in a reversible but hysteretic way, and therefore one could move the oxygen vacancies back and for. It is interesting to note that no degradation of the gating process is found at -3 V, indicating that the threshold voltage to degrade the double layer with negative applied voltages is higher than the positive ones. This fact can be compatible with the scenario of the oxygen migration, since the anions would accumulate in the YBCO surface, avoiding the removal of the oxygen and the eventual degradation of the EDL.

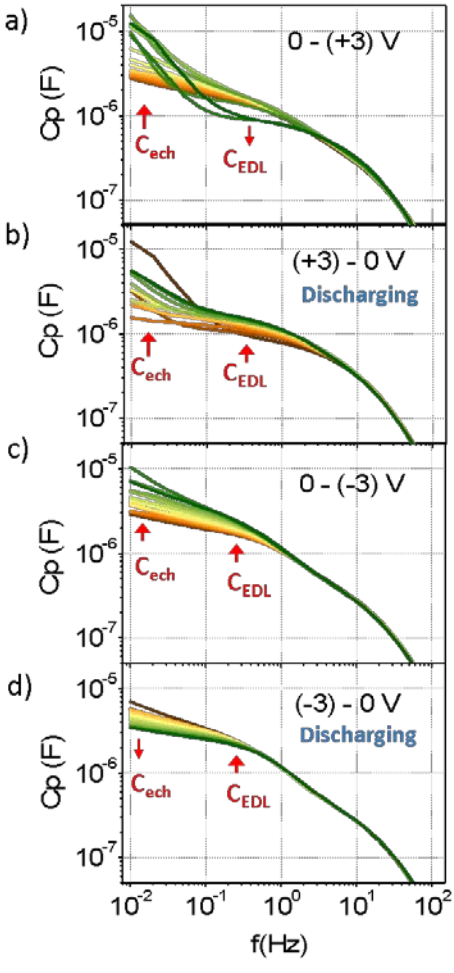

Figure 8.5 Capacitance, conductivity and phase angle measurements for a cycle of voltages at 240 K; starting from 0 to 3 (a), removing the bias (b), applying negative voltages (c) and removing the negative bias (d). A purely electrostatic mechanism is found at low voltages followed by electrochemical reactions happening in the interface for higher voltages. At high positive voltages (+3V) a degradation of the double layer was obtained that is absent in the negative voltages. This is associated with the oxygen displacement of the ions up to the interface provoking the EDL to break.

Finally Figure 8.5(d) shows the discharging process of the negative applied voltages. A progressive decrease of the capacitance is observed for the electrochemical contribution, and less evident, for the EDL, ending up in a

situation where almost no voltage dependence is observed for capacitance spectra at the smallest negative values.

7. Voltage induced ordering

One of the exotic features of ionic liquids in metal electrodes is the relation of the long range structural order and the electrochemical response of the EDL [271].To have an insight in this topic we performed a series of capacitance and conductance measurements at fixed temperatures from 180 to 300 K, probing the AC IL response in the presence of the YBCO metal electrode (the configuration described in Chapter 4). The measurements were performed after a gating of the YBCO at $V_G = 3$ V, so we want to address if such a voltage can induce structural changes in the EDL.

Capacitance and conductance isotherms are shown in Figure 8.6 (a) and (b), data were obtained increasing temperature from 180 K, below the glass transition temperature of the ionic liquid. If the gating voltage induces any ordering or "crystallization", a sudden change in capacitance or conductance is expected as increasing temperature, when the gated induced phase is melted. Such a behavior is observed in figures 8.6 (a) and (b), a flat capacitance curve with a value of 20 pF is observed in the ordered phase for temperatures below 240 K, and at 250 K the curve changes completely to the typical IL behavior observed in chapter 4, with the capacitance increasing 4 orders of magnitude at the lowest frequencies. The same spectacular change is observed in the conductance representation, fig. 8.6 (b), where a negligible conductance is observed in the solid ordered phase below 10^{-9} S, and when increasing the temperature to 250 K the melting of the phase increases the conductance over 6 orders of magnitude to 10^{-3} S. Therefore, in this series of curves in figure 8.6 (a) and (b) we observe the returning to the equilibrium of the IL (isotropic liquid) of the interface of the YBCO electrode and the IL.

Figure 8.6 (c) and (d) shows the cooling process after the previous heating measurements. No gate voltage was applied and the data follow the standard normal behavior of an IL.

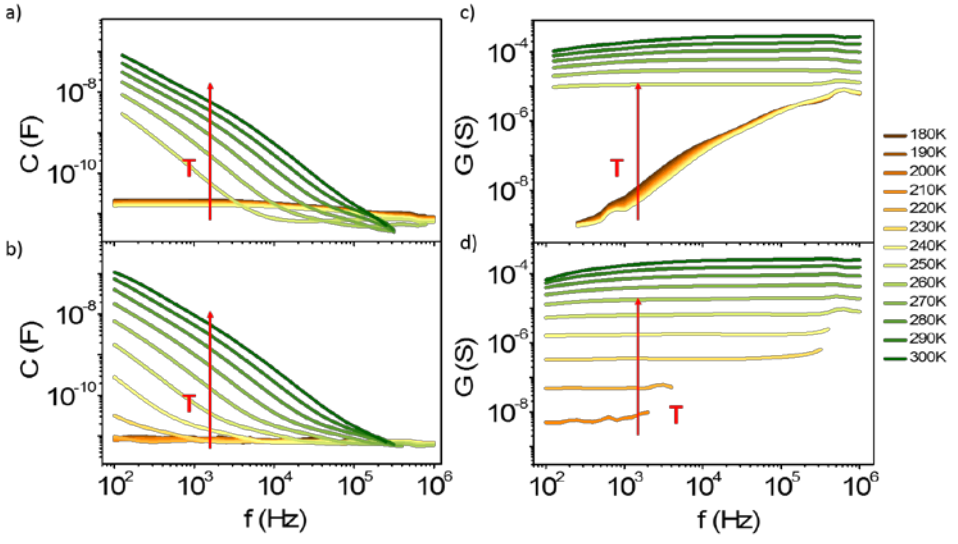

Figure 8.6 Capacitance and conductance measured at different temperatures from 180 - 300 K, a) b) Heating process showing the ordering or "crystallization" after the gating Vg=3 V. c) and d) are measured cooling down showing the standard normal behavior of an IL.

8 Conclusions

Electrochemical impedance spectroscopy (EIS) has been applied as a method for distinguishing the electrostatic or electrochemical nature of the EDL interface. Several experiments have been performed to observe the gating/doping process of the surface of an YBCO thin film using the EDL of an IL.

AC Impedance data analyzed in terms of the tan(δ) measurements, capacitance and conductivity, show the different contributions to the charge accumulation in the YBCO electrode. The bulk, EDL and electrode response are well separated in the frequency domain and can be identified and studied individually. Increasing gating voltage, a mainly electrostatic doping of the YBCO appears up to values around 1 V. Over this threshold voltage and below 3 V, electrochemical reactions are evidenced in the electrical characterization, supporting the presence of oxygen migration observed in XAS. A degradation of the double layer was found at the highest voltage (+3 V) that may come from the direct interaction of the oxygen

ions with the IL at the interface exhibiting an unusual decreasing of the capacitance.

The reversibility of the gating process was investigated measuring negative a complete symmetric cycle going to – 3 V and then to 0 V. In contrast with the positive gating, no evident EDL degradation was observed at -3 V, as the oxygen ions are force out of the interface. We also found indications of a voltage induced ordering or “crystallization” of the IL in the metallic electrode of the YBCO.

In this chapter we have discovered the boundaries of the electrochemical reactions originating the IL-doping process by means of Impedance Spectroscopy, which appear as a simple method to follow “in operando” the gating process in EDLT, easily separating the electrostatic and electrochemical contributions.

.

CHAPTER 9

Conclusions

The new and novel electrostatic double layer transistors (EDLT) have broadened the boundaries of field effect experiment on condensed matter systems. Specifically on cuprates IL-doping has enabled the exploration of their rich phase diagrams by the possibility to abruptly modify their physical properties controlling the charge carrier density [16–20]

Recent results obtained with EDL transistors have challenged the conventional understanding of the EDL operation regarded in terms of modifications of the charge density to screen the electric field generated at the double layer. It has been recently reported that the suppression of the metal to insulator transition induced in VO_2 by ionic liquid gating is due to oxygen vacancy formation rather than to electrostatic doping [22, 23]. These results underscore the debate on the true nature, electrostatic vs electrochemical, of the doping of cuprates with ionic liquids. These results highlight the necessity of careful studies of the mechanism of doping induced by the electric field generated at the interface between the tested material and the ionic liquid to fully understand the innermost origin of the generated electric charge.

In this thesis, we address the doping mechanism of the high temperature superconductor $YBa_2Cu_3O_{7-X}$ (YBCO) induced by the EDL technique. A deep characterization of the system has been done, optimizing the growth conditions of the 3u.c YBCO ultrathin-films. In addition, a full impedance spectroscopy characterization of the used IL has been given including a detail explanation of the device fabrication.

Simultaneous ionic liquid gating on $YBa_2Cu_3O_{7-X}$ (YBCO) and X-ray absorption experiments were conducted. Pronounced spectral changes are observed at the Cu K-edge concomitant with the superconductor-to-insulator transition, evidencing

modification of the Cu coordination resulting from the deoxygenation of the CuO chains. The charge transfer between CuO_2 planes and CuO_X chains yielding superconducting planes is therefore hindered and the superconductivity suppressed. The obtained results were confirmed by first principles density functional theory (DFT) simulations.

Experiments using intermediate layers acting as oxygen barriers (Al_2O_3) and oxygen reservoirs ($PrBa_2Cu_3O_7$ (PBCO)) confirm the effect of the large electric field at the interface between the ionic liquid and the YBCO inducing electromigration of oxygen ions from the CuO_x chains [264]. It has enable the examination of the role of oxygen out-diffusion from the sample during the doping process. Oxygen diffusion into the isostructural PBCO interlayer layer facilitates oxygen migration and the measured curves resemble those of deoxygenated YBCO [106].

The reversibility of the doping process has been studied by means of the disorder induced in the sample. Device operation is reversible as far as the superconductor-insulator transition is not reached. Negative voltages were applied to restore the initial state superconducting critical temperature supporting oxygen go and back diffusion. The temperature was found to play a key role in the reversibility process and electrostatic effect cannot be deny for low voltages.

Electrochemical impedance spectroscopy (EIS) measurements verify the scenario of creation of oxygen vacancies being a direct method to identify electrochemical reactions in the IL-YBCO interface while doping. The bulk, EDL and electrode responses are well separated in the frequency domains and have enable to distinguish the electrostatic or electrochemical nature in terms of the applied voltage.

To summarize, exceeding an initial electrostatic contribution the process that governs the IL-doping in the YBCO has a chemical origin and arises from the electromigration of oxygen ions from the CuO_x chains. This thesis provides direct evidence of deoxygenation in ionic liquid gating of YBCO and the results exposed here outline the importance of electrochemical processes in EDL transistors. We have demonstrated that EDL involves atomic displacements associated to the very strong electric fields generated at the interface of the cuprate and the ionic liquid

and it should not be regarded equivalent to chemical doping or conventional electrostatic doping using solid gates.

Beyond providing evidence of the importance of chemical doping in EDL gating experiments with superconducting cuprates, our work shows that interfacing correlated oxides with ionic liquids enables a delicate control of oxygen content paving the way to novel electrochemical concepts in future oxide electronics. Our work shows the potential of gating with ionic liquids as a powerful tool for the controlled generation of oxygen vacancies in oxides and thus, it signals a path to a new degree of freedom in future oxide electronics devices exploiting phase changes associated to this doping strategy.

CHAPTER 10

Resumen en español

1 Introducción y objetivo

La posibilidad de usar un campo eléctrico para modular la densidad de carga de un semiconductor de manera controlada es la base de la industria tecnológica actual. Más allá de estos materiales, los óxidos complejos prometen ser toda una familia fascinante para generar nuevos dispositivos debido a la posibilidad de controlar la densidad de carga a lo largo de sus ricos diagramas de fases. En particular, los óxidos complejos, basados en metales de transición, son extremadamente sensibles a la concentración de portadores, presentando distintas fases estables con fenómenos físicos tales como transiciones metal-aislante, magnetorresistencia colosal o superconductividad de alta temperatura [1, 277–280].

Diversos experimentos de dopado de estos óxidos complejos se han llevado a cabo desde hace tiempo [2–8], y en los últimos años, unos nuevos transistores llamados transistores de doble capa (EDLT) han conseguido cambios sin precedentes usando un líquido iónico como dieléctrico de puerta [9–11]. Estos nuevos transistores de doble capa han ampliado las fronteras de los experimentos de efecto campo en los sistemas de materia condensada, permitiendo inducir superconductividad en materiales aislantes tales como $SrTiO_3$ [12], ZrNCl [13], $KTaO_3$ [14] o en MoS_2 [15]. Especialmente en cupratos, la aplicación de voltajes de puerta positivos a través del líquido iónico, se asoció a una disminución de los portadores de carga, en este caso huecos, permitiendo modificar sus propiedades superconductoras e inducir su estado aislante [16–20].

Estos resultados han conseguido que la comunidad científica centre su atención en la técnica del EDL, no solo desde un punto de vista funcional y aplicado sino

también desde el punto de vista de la física fundamental por ser una oportunidad única para entender y estudiar los ricos diagramas de fase de estos materiales.

Sin embargo, los resultados más recientes con los transistores de doble capa han desafiado la interpretación convencional del funcionamiento de los transistores EDL en óxidos complejos, demostrando que el dopado con líquidos iónicos, más allá de tratarse de un mecanismo puramente electrostático debido al apantallamiento de las cargas de la interfase, es debido a la migración de átomos de oxigeno de sus celdas unidad [22, 23].

Estos resultados han abierto el debate sobre la verdadera naturaleza, electrostática o electroquímica del dopado de cupratos con líquidos iónicos. Queda así motivada la necesidad de estudiar el mecanismo de dopado al generar un alto campo eléctrico entre el material y el IL para entender en profundidad el verdadero origen de la carga eléctrica generada.

Esta tesis, se ha centrado en el estudio del mecanismo de dopado del superconductor de alta temperatura $YBa_2Cu_3O_{7-x}$ (YBCO) usando la técnica de dopado con líquidos iónicos mediante un transistor de doble capa (EDLT). Diferentes experimentos de dopado de dicho material nos han permitido estudiar su transición superconductor–aislante, así como explorar la estructura electrónica del YBCO en sus diferentes fases estables y la naturaleza de este proceso de carga por sí mismo.

2 Resultados y conclusiones

Se ha realizado una completa caracterización del sistema, optimizando las condiciones de crecimiento y garantizando una perfecta calidad cristalina de películas ultradelgadas de 3c.u. de YBCO. Además, se ha llevado a cabo una caracterización del líquido iónico usando la técnica de espectroscopia de impedancias, y de igual manera, se ha incluido una explicación detallada de la fabricación del dispositivo y del funcionamiento de las medidas realizadas con esta nueva técnica.

Se han llevado a cabo simultáneamente experimentos de dopado de $YBa_2Cu_3O_{7-X}$ (YBCO) con líquido iónico a la vez que se han realizado medidas de absorción de rayos X. Los espectros muestran notables cambios en el borde K del Cu concurrente con la transición superconductor-aislante dando una clara evidencia de la modificación de la coordinación del cobre Cu, asociada a una desoxigenación de las cadenas CuO del YBCO. La transferencia de carga entre los planos superconductores CuO_2 y de las cadenas CuO_X, que produce los planos superconductores, es entonces reducida provocando una supresión de la superconductividad. Cálculos de DFT corroboran que los cambios en los espectros de absorción corresponden a una disminución del oxígeno de las cadenas CuO_x del YBCO.

Experimentos usando capas intermedias que actúan como barrera de oxigeno (Al_2O_3) y como reservorio de oxigeno ($PrBa_2Cu_3O_7$ (PBCO)) confirman que el efecto de tan grande campo eléctrico en la interfase del IL con el YBCO induce migración de iones de oxígeno de las cadenas de CuO_x [264]. Este experimento ha permitido estudiar el papel de la difusión del oxígeno saliendo de la muestra durante el proceso de dopado. La difusión del oxígeno en el aislante isostructural PBCO facilita la migración del mismo y sus curvas de transporte se asemejan a las de un YBCO desoxigenado [106].

La reversibilidad del proceso se ha estudiado en términos del desorden inducido en la muestra. El dispositivo es reversible siempre y cuando la transición superconductor aislante no se alcanza. Voltajes negativos fueron aplicados para restaurar el estado superconductor inicial induciendo una difusión del oxígeno a sus posiciones iniciales. Se ha encontrado que la temperatura juega un papel fundamental en el proceso reversibilidad y la migración de oxígeno a pesar de que un pequeño efecto electrostático a bajos voltajes no puede ser rechazado.

Medidas de espectroscopia de impedancia verifican este escenario de creación de vacantes de oxígeno indicando reacciones electroquímicas en la interfase del IL con el YBCO mientas se dopa. Esta técnica permite separar fácilmente en el dominio de frecuencias la electro-respuesta del bulk, de la doble capa y del electrodo. Se convierte así, en un método directo para identificar las reacciones químicas en la interfase del IL-YBCO y, por tanto, en una herramienta única para

separar la naturaleza electrostática de la electroquímica en función del voltaje aplicado.

A modo de resumen, esta tesis aporta una evidencia directa de la desoxigenación del YBCO en experimentos de dopado con líquidos iónicos resaltando la importancia de las reacciones químicas en los experimentos con EDL. Se ha demostrado que esta técnica incluye desplazamientos de los oxígenos de sus posiciones atómicas debido a los fuertes campos eléctricos generados en la interfase del IL y del YBCO, de manera que la técnica de dopado con líquidos iónicos no puede verse más como un dopado convencional puramente electrostático.

Además, más allá de ser una evidencia de la importancia del dopado químico en los experimentos con EDL en cupratos superconductores, nuestros resultados muestran que una combinación de estos óxidos complejos con los nuevos transistores de doble capa permite un control delicado del contenido de oxígeno presentándose como una herramienta con un potencial único, sentando las bases de nuevos conceptos electroquímicos e indicando un nuevo camino para futuras aplicaciones en dispositivos electrónicos.

CHAPTER 11

Annex

1 List of publications

1) **A. M. Perez-Muñoz**, P. Schio, R. Poloni, A. Fernandez-Martinez, A. Rivera-Calzada, J. C. Cezar, E. Salas-Colera, G. Castro, Joe Kinney, C. Leon, J. Santamaria, J. Garcia-Barriocanal, A. M. Goldman. *In-operando* evidence of deoxygenation in ionic liquid gating of $YBa_2Cu_3O_{7-X}$. Future publication in PRX

2) C. Visani, F. Cuellar, **A. M. Perez-Muñoz**, Z. Sefrioui, C. León, J. Santamaría, and J. E. Villegas. *Magnetic field influence on the proximity effect at YBa2Cu3O7/La2/3Ca1/3MnO3 superconductor/half-metal interfaces*. Phys. Rev. B 92, 014519 **(2015)**

3) M. Rocci, J. Azpeitia, J. Trastoy**, A. M. Perez-Muñoz**, M. Cabero, R. F. Luccas, C. Munuera, F. J. Mompean, M. Garcia-Hernandez, K. Bouzehouane, Z. Sefrioui, C. Leon, A. Rivera-Calzada, J.E. Villegas, y J. Santamaria. *Proximity Driven Commensurate Pinning in YBa2Cu3O7 through All-Oxide Magnetic Nanostructures*. *Nano Lett.*, *15* (11), pp 7526–7531 **(2015)**

4) A. Alberca, C. Munuera, J. Azpeitia, B. Kirby, N. M. Nemes, **A. M. Perez-Muñoz**, J. Tornos, F. J. Mompean, C. Leon, J. Santamaria, M. Garcia-Hernandez. *Phase separation enhanced magneto-electric coupling in La0.7Ca0.3MnO3/BaTiO3 ultra-thin films.* Scientific reports 5,17926 **(2015)**

5) J. Garcia-Barriocanal, **A. M. Perez-Muñoz**, Z. Sefrioui, D. Arias, M. Varela, C. Leon, S.J. Pennycook and J. Santamaria. *Disorder-controlled superconductivity at $YBa_2CuO_7/SrTiO_3$ interfaces.* Phys. Rev. B 87, 245105 **(2013).**

2 Conference contributions

1) In situ X-ray absorption spectroscopies study during doping of YBa2Cu3O7-X (YBCO) with an ionic liquid. **A. M. Pérez-Muñoz**, P. Schio, R. Poloni, A. Rivera-Calzada, J. C. Cezar, E. Salas, G. Castro, N.M.Nemes, M.Clement, E.Iborra, C.León, J.Santamaría, J.García-Barriocanal

Contribution: Oral

Location: Invited talk at Unité de Physique CNRS/Thales (Paris)

Date: 14 January 2016

2) In situ X-ray absorption spectroscopies study during electron doping of $YBa_2Cu_3O_{7-X}$ (YBCO) using an electric double layer (EDLT) configuration. **A. M. Pérez-Muñoz**, P. Schio, R. Poloni, A. Rivera-Calzada, J. C. Cezar, E. Salas, G. Castro, N.M.Nemes, M.Clement, E.Iborra, C.León, J.Santamaría, J.García-Barriocanal

Contribution: Oral

Location: XXXV Bienal de la Real Sociedad Español de Fisica, Gijón. Spain

Date: Julio 2015

3) Oxygen vacancy control of a ferroelectric memristor. **J. Santamaría,** Yaohua Liu, S. G. E. te Velthuis, D. Hernandez-Martín, A. M. Pérez Muñoz, M. Cabero, G. Sanchez-Santolino, J. Tornos, M. Varela, C. Leon, Z. Sefrioui, S. J. Pennycook

Contribution: Oral

Location: American Physical Society March Meeting 2015, San Antonio, Texas (USA)

Date: March, 2015

4)	Memristive behavior in tunnel junctions with graphene oxide barrier. **M. Rocci**, A. M. Perez-Muñoz, J. Del Valle, J.L. Vicent, C. Leon, Z. Sefrioui, J. Santamaria, F. Perrozzi, L. Ottaviano, M. Nardone, S. Santucci, E. Treossi, V. Palermo
Contribution	Oral
Location	American Physical Society March Meeting 2015, San Antonio, Texas (USA)
Date	March, 2015
5)	Oxygen vacancy control of resonant transport through ferroelectric domain walls in tunneling devices. **G. Sanchez-Santolino,** J. Tornos, D. Hernandez, A.M. Perez-Muñoz, M. Cabero, Z. Sefrioui, C. Leon, M. Varela, J. Santamaria, J. I. Beltran, M. C. Muñoz, C. Munuera, F. Mompean, M. Garcia-Hernandez, S. J. Pennycook
Contribution	Oral
Location	TO-BE Spring Meeting 2015.University of Aveiro, Aveiro, Portugal
Date	March 2015
6)	The mechanism of electrostatic doping on $YBa_2Cu_3O_7$ thin films investigated by X-ray absorption spectroscopy. **P. Schio**, A.M. Perez-Muñoz, A. Riveira-Calzada, J.C. Cezar, J. Garcia-Barriocanal, J. Santamaria.
Contribution	Oral
Location	XXXVIII ENFMC Brazilian Physical Society Meeting Foz do Iguaçu, PR
Date	May 2015
7)	Electrostatic doping of strongly correlated systems with ionic liquids. **A. Rivera-Calzada**, A.M. Pérez-Muñoz, P. Schio, R. Poloni , , J. C. Cezar, E. Salas, G.Castro, N.M.Nemes, M.Clement, E.Iborra, C.León, J.Santamaría, J.García-Barriocanal.
Contribution	Oral
Location	EXIL (Exhange on IL) COST CM1206 Workshop, Belek, Turkey
Date	Oct 2015

3 Short research stays

Center	*ESRF (European Synchrotron Radiation Facility*) at the Spanish BM25 Beamline (Spline).
Location	Grenoble (France)
Date	September 2014
Funding	European Research Council and Universidad Complutense de Madrid
Topic	X-ray absorption spectroscopies at the Cu K edge while doping of YBa2Cu3O7-X (YBCO) with an ionic liquid.
Center	*(Brazilian National Laboratry of Synchrotron Light)* at the PGM soft X-Ray beamline
Location	Campinas, Sao Paolo (Brasil)
Date	Dicember 2014
Funding	Group Funding. Spanish MICINN through grants MAT2011-27470-C02, MAT2014-52405-C2-1-R and Consolider Ingenio 2010- CSD2009-00013 (Imagine), by CAM through grant S2009/MAT-1756 (Phama) and S2013/MIT-2740 (Phama_2.0).
Topic	X-ray absorption spectroscopies at the O K-edge while doping of YBa2Cu3O7-X (YBCO) with an ionic liquid.

CHAPTER 12

Bibliography

1. M. Imada, A. Fujimori, Y. Tokura, Metal-insulator transitions. *Rev. Mod. Phys.* **70**, 1039–1263 (1998).
2. C. H. Ahn, J.-M. Triscone, J. Mannhart, Electric field effect in correlated oxide systems. *Nature*. **424**, 1015–1018 (2003).
3. C. H. Ahn *et al.*, Electrostatic modification of novel materials. *Rev. Mod. Phys.* **78**, 1185–1212 (2006).
4. D. G. S. J.Mannhart, Oxide Interfaces- An Opportunity for Electronics. *Science (80-.).* **327**, 1607 (2010).
5. A. P. M. S. and R. V. A. Cassinese, G.M. De Luca, Field-effect tuning of carrier density in $Nd_{1.2}Ba_{1.8}Cu_3O_y$ thin films. *Appl. Phys. Lett.* **84**, 3933 (2004).
6. M. Salluzzo *et al.*, Indirect electric field doping of the CuO2 planes of the cuprate $NdBa_2Cu_3O_7$ superconductor. *Phys. Rev. Lett.* **100**, 8–11 (2008).
7. K. A. Parendo, K. H. S. B. Tan, A. Bhattacharya, N. E. Staley, A. M. Goldman, Electrostatic Tuning of the Superconductor-Insulator Transition in Two Dimensions. *Phys. Rev. Lett.* **94**, 197004 (2005).
8. K. Ueno *et al.*, Field-Effect Transistor on $SrTiO_3$ with sputtered Al_2O_3 Gate Insulator. *Appl. Phys. Lett.* **83**, 1755 (2003).
9. H. Shimotani *et al.*, Insulator-to-metal transition in ZnO by electric double layer gating. *Appl. Phys. Lett.* **91**, 15–18 (2007).
10. H. Yuan *et al.*, High-density carrier accumulation in ZnO field-effect transistors gated by electric double layers of ionic liquids. *Adv. Funct. Mater.* **19**, 1046–1053 (2009).
11. Y. Yamada *et al.*, Electrically induced ferromagnetism at room temperature in cobalt-doped titanium dioxide. *Science*. **332**, 1065–1067 (2011).
12. K. Ueno *et al.*, Electric-field-induced superconductivity in an insulator.

Nat. Mater. **7**, 855–858 (2008).

13. J. T. Ye *et al.*, Liquid-gated interface superconductivity on an atomically flat film. *Nat. Mater.* **9**, 125–128 (2010).
14. K. Ueno *et al.*, Discovery of superconductivity in $KTaO_3$ by electrostatic carrier doping. *Nat. Nanotechnol.* **6**, 408–412 (2011).
15. J. T. Ye *et al.*, Superconducting Dome in a Gate-Tuned Band Insulator. *Science (80-.).* **338**, 1193–1196 (2012).
16. X. Leng, J. Garcia-Barriocanal, S. Bose, Y. Lee, a. M. Goldman, Electrostatic control of the evolution from a superconducting phase to an insulating phase in ultrathin YBa2Cu3O7-x films. *Phys. Rev. Lett.* **107**, 6–9 (2011).
17. A. T. Bollinger *et al.*, Superconductor-insulator transition in La2 - xSrxCuO4 at the pair quantum resistance. *Nat. 458*. **472**, 8–10 (2011).
18. X. Leng *et al.*, Indications of an electronic phase transition in two-dimensional superconducting YBa 2Cu 3O 7-x thin films induced by electrostatic doping. *Phys. Rev. Lett.* **108**, 1–5 (2012).
19. J. Garcia-Barriocanal *et al.*, Electronically driven superconductor-insulator transition in electrostatically doped La2CuO4+ thin films. *Phys. Rev. B.* **87**, 1–11 (2013).
20. S. W. Zeng *et al.*, Two-dimensional superconductor-insulator quantum phase transitions in an electron-doped cuprate. *Phys. Rev B.* **92**, 020503(R) (2015).
21. Y. Lee, A. Frydman, T. Chen, B. Skinner, a. M. Goldman, Electrostatic tuning of the properties of disordered indium-oxide films near the superconductor-insulator transition. *Phys. Rev. B - Condens. Matter Mater. Phys.* **88**, 1–5 (2013).
22. M. Li *et al.*, Suppression of ionic liquid gate-induced metallization of SrTiO 3(001) by oxygen. *Nano Lett.* **13**, 4675–4678 (2013).
23. J. Jeong *et al.*, Suppression of metal-insulator transition in VO2 by electric field-induced oxygen vacancy formation. *Science*. **339**, 1402–5 (2013).
24. W. K. and G. K. S. Maekawa, T. Tohyama, S.E. Barnes, S. Ishihara, *Physics of Transition Metal Oxides (Springer, 2004), chap. 1*.
25. E. Dagotto, Complexity in Strongly Correlated. *Sci. 309, 257* (2005), doi:10.1126/science.1107559.
26. E. Dagotto, Y. Tokura, S trongly Correlated Electronic Materials : **33**, 1037–1045 (2008).
27. H. Y. Hwang *et al.*, Emergent phenomena at oxide interfaces. *Nat. Mater.*

11, 103–113 (2012).

28. D. G. S. J.Mannhart, Oxide Interfaces — An Opportunity for Electronics. *Science (80-.).* **327**, 1607–1611 (2010).
29. S. O. and A. J. Millis, Electronic reconstruction at an interface between a Mott insulator and a band insulator. *Nature*, *428*, *630-633*. **428**, 2–5 (2004).
30. R.E.Glover, Changes in superconducting critical temperature produced by electrostatic charging. *Phys. Rev. Lett.* **5** (1960).
31. D. M. Newns *et al.*, Mott transition field effect transistor. *Appl. Phys. Lett.* **73**, 780–782 (1998).
32. J. G. Bednorz, K. a. Muller, Possible High Tc Superconductivity in the Ba - La - Cu - O System. *Zeitschrift für Phys. B Condens. Matter*. **64**, 189–193 (1986).
33. Y. Kamihara, T. Watanabe, M. Hirano, H. Hosono, Iron-Based Layered Superconductor La [O 1 - x F x] FeAs (x) 0 . 05 - 0 . 12) with T c) 26 K, 3296–3297 (2008).
34. R. E. Cohen, Origin of ferroelectricity in perovskite oxides. *Nature*. **358**, 136–138 (1992).
35. J. H. Park *et al.*, Direct evidence for a half-metallic ferromagnet. *Nature*. **392**, 794–796 (1998).
36. Y. Tokura, Y. Tomioka, Colossal magnetoresistive manganites. *J. Magn. Magn. Mater.* **200**, 1–23 (1999).
37. J. Brockman, thesis, Stanford University (2012).
38. N. Mott, On metal-insulator transitions. *J. Solid State Chem.* **88**, 5–7 (1990).
39. J. Hubbard, P. R. S. L. A, Electron Correlations in Narrow Energy Bands. *Proc. R. Soc.Lond.A.* **238-257** (1963), doi:10.1098/rspa.1963.0204.
40. N. F. Mott, The Basis of the Electron Theory of Metals, with Special Reference to the Transition Metals. *Science (80-.).* (1949).
41. J. A. M. and P. C. P. C. Zhou, D. M. Newns, A Field Effect Transitor based on the Mott Transition in a Molecular Layer. *Appl. Phys. Lett. 70,* 23–26 (1997).
42. J. Hubbard, Proc. Roy. Soc. A276, 238. *1963*.
43. T. Oka, and H. Aoki, edited by B. K. Chakrabarti, K. K. Bardhan, and A. K. Sen (Springer Berlin / Heidelberg, 2009).
44. V. I. Anisimov, J. Zaanen and O. K. Andersen. Band theory and Mott insulators: Hubbard U instead of Stoner I. Physical Review B, 44, 943-954 (1991).

45. Y. T. and Y. T. A. Fujimori, T. Yoshida, K. Okazaki, T. Tsujioka, K. Kobayashi, T. Mizokawa, M. Onoda, T. Katsufuji, Electronic structure of Mott-Hubbard type transition-metal oxides. *J. Electron Spectrosc. Relat. Phenomena, 117,A118, 277-286 (2001).*

46. M. Cardona and F. H. Pollak. Energy-Band Structure of Germanium and Silicon: The k-p Method. Physical Review, 142, 530-543 (1966).

47. B. Moyzhes, T. H. Geballe, S. Jeong, D. Gitlin and J. Karp. Current through SiO2 gate oxide and its low frequency fluctuations: Trapping on charged dangling bonds with negative Hubbard U. Journal of Applied Physics, 97, 074104 (2005).

48. D. M. Edwards and A. C. Hewson. Comment on Hubbard's Theory of the Mott Transition. Reviews of Modern Physics, 40, 810-811 (1968).

49. A. J. Zaaneen, Sawatzky, Band Gaps and Electronic Structure of Transition-Metal Compounds. *Phys. Rev. Lett.* **55** (1985).

50. A. Fujimori. Lectures on strongly correlated systems using synchrotron radiation: Basics to frontiers, Available online: http://wyvern.phys.s.u-tokyo.ac.jp/f/lecture/srrc/SRRC_MIT.pdf (2012).

51. P. W. Anderson, Phys. Rev. B 115, 2(1959), ibid. Adv. in Phys. 46, 3 (1997).

52. P. W. Anderson, in Magnetism, G. T. Rado, H. Suhl (Eds.), vol. 1, New York 1963.

53. J. B. Goodenough, Magnetism and the Chemical Bond, Interscience Publ., New York–London, 1963.

54. P. W. Anderson, Phys. Rev. B 79, 350 (1950); J. B. Goodenough, Phys. Rev. B 100, 546 (1955); J. Kanamori, J. Phys. Chem. Solid 10, 87 (1959).

55. H. K. Onnes., The resistance of pure mercury at helium temperatures. *Comm. Phys. Lab. 12 , 120b*. **Univ. Leid** (1911).

56. W. Meissner and R. Ochsenfeld, No Title. *Naturwissenschaften 21 787* (1933).

57. and J. R. S. J. Bardeen, L. N. Cooper, Theory of superconductivity. *Phys. Rev 108, 1175* (1957).

58. M. Tinkham, *Introduction to Superconductivity* (1996).

59. Z. E. V. Ginzburg and L. Landau, No Title. *Zh. eksper. teor. Fiz 20, 1064* (1950).

60. L. P. Gor'kov, No Title. *Zh. Eksperim. i. Theo. Fiz. 36, 1918* (1959).

61. G. S. PJ Ford, *The Rise of the Superconductors* (2005).

62. A. J. Leggett, What DO we know about high T c ? *Nat. Phys. 2, 134* (2006).

63. Z. Ren *et al.*, Superconductivity and phase diagram in iron-based arsenic-oxides ReFeAsO 1 − δ (Re = rare-earth metal) without fluorine doping. *EPL 83,17002.* (2008), doi:10.1209/0295-5075/83/17002.

64. A. F. and F. Minima, Valence-band photoemission and optical absorption in nickel compounds. *Phys. Rev. B, 30 , 957.* **30** (1984).

65. S. Hüfner, No Title. *Z. Phys. B, 61,135* (1985).

66. J. F. A. and R. M. M. A.K. McMahan, Cuprate parameters from numerical Wannier funtions. *Phys. Rev. B, 42 , 6268.* **42**, 6268–6283 (1990).

67. E. Pickett, Electronic structure of the high-temperature oxide superconductors. *Rev. Mod. Phys.* **61** (1989).

68. M. S. and D. R. M.S. Hybertsen, E.B. Stechel, Jennison, renrmalization from density-funtional theory to strong-coupling models for electronic states un Cu-O materials. *Phys. Rev. B.* **41**, 68–72 (1990).

69. V. J. Emery, Theory of High-Tc superconductivity in Oxides. *Phys. Rev. Lett.* **58**, 2794–2797 (1987).

70. J. Fink *et al.*, Electron energy-loss and X-ray absorption spectroscopy of cuprate superconductors and related compounds. *J. Electron Spectros. Relat. Phenomena*. **66**, 395–452 (1994).

71. A. J. A. C.G. Olson, R. Liu, D.W. Lynch, R.S. List, Y. C. C. P. Z. J. and A. P. P. B.W. Veal, High-resolution angle-resolved photoemission study of the Fermi surface and the normal-state electronic structure of BiSrcaCuO. *Phys. Rev. B.* **42**, 381–387 (1990).

72. R. M. G. Mante, R. Claesscn, T. Buslaps, S. Harm, M. S. and J. Fink, No Title. *Z. Phys. B, 80 , 181.* (1990).

73. L. B. J.C. Campuzano, G. Jennings, M. Faiz, H. B.W. Veal, J.Z. Liu, A.P. Paul&as, K. Vandervoort, A. J. A. and R. J. B. Claus, R.S. List, Fermi Surfaces of YBCO as seen by angle-Resolved Photoemision. *Phys. Rev. Lett.* **64** (1990).

74. M. B. J. M. and G. A. S. H. Eskes, Anomalous Transfer of Spectral Weight in Doped Strongly Correlated Systems. *Phys. Rev. Lett.* **67**, 1035–1038 (1991).

75. H. E. and G. A. S. M.B.J. Meinders, Spectral-weight transfer:Breakdown of low-energy-scale sum rules in correlated systems. *Phys. Rev. B.* **48**, 3916–3926 (1993).

76. 235 (1987) 1196; 256 (1992) 1526. P.W. Anderson, Science, S. S. G. Baskaran, Z. Zou and P.W. Anderson, 63 (1987) 973. Commun., 65 (1990) 2306. P.W. Anderson, Phys. Rev. L&t., No Title.

77. F.C. Zhang and T.M. Rice, Effective Hamiltonian for the superconducting

Cu oxide. *Phys. Rev. B.* **37**, 7–9 (1988).

78. W. S. and P. Horsch, fermi Surface and Dynamics of the t-J Model at Moderate Doping. *Phys. Rev. Lett.* **66** (1991).

79. A. M. and W. G. Dopf, J. Wagner, P. Dietrich, Hanke, Direct Comparison of Angle-Resolved Photoemission and Numerical Simulations for High-Tc supercondcutors. *Phys. Rev. Lett.* **68**, 2082–2085 (1992).

80. M. S. G. Mante, R. Claessen, A. Huss, R. Manzke, M. K. and I. F. Th. Wolf, Occupied electronic structure and Fermi surface of YBCO. *Phys. Rev. B.* **44** (1991).

81. K. A. Müller, On the oxygen isotope effect and apex anharmonicity in high-Tc cuprates. **80**, 193–201 (1990).

82. W. Weber, Z. Phys. B, 70 323 (1988).

83. H. R. K. D.L. Cox, M. Jarrell, C. Jayaprakash, and J. Deisz, Virtual Electric Quadrupole Fluctuations: A Mechanish for Hight Tc. *Phys. Rev. Lett.* **62**, 2188–2191 (1989).

84. H. K. and M. Eto, A1g to B1g conversion at eh Onset od superconductivity in La2-xSrxCuO4 due to the Apical Oxygen Effect. *J. Phys. Sot. Jpn., 59, 3053.* (1990).

85. J. Z. and O. K. A. V.I. Anisimov, M.A. Korotin, Spin Bags, Polarons, and Impurity Potentials in La2-xSrxCuO4 from First Principles. *Phys. Rev. Lett. 68*, 345–348 (1992).

86. L. F. F. and M. G. C. Di Castro, Symmetry of Hole States in Superconducting Oxides: Correlation with Tc. *Phys. Rev. Lett.* **66**, 3209–3212 (1991).

87. M. G. and C. D. C. L.F. Feiner, Apical oxygen ions and the electronic structure of the high Tc cuprates. *Phys. Rev B.* **45** (1992).

88. H. Eskes and G.A. Sawatzky, Single-, triple-, or multiple-band Hubbard models. *Phys. Rev B.* **44** (1991).

89. LB. Grant and A.K. McMahan, Spin bags and quasiparticles in doped La2CuO4. *Phys. Rev B, 46, 13* (1992).

90. D. Basov, T. Timusk, Electrodynamics of high-T c superconductors. *Rev. Mod. Phys.* **77**, 721–779 (2005).

91. M. Magnuson *et al.*, Self-doping processes between planes and chains in the metal-to-superconductor transition of YBa2Cu3O6.9. *Sci. Rep.* **4**, 7017 (2014).

92. M. Maki, T. Nishizaki, K. Shibata, N. Kobayashi, Electronic structure of the CuO-chain layer in YBa2Cu3O7-δ studied by scanning tunneling

microscopy. *Phys. Rev. B.* **65**, 3–6 (2002).

93. S. Massidda, J. Yu, A. J. Freeman, ELECTRONIC STRUCTURE AND PROPERTIES OF YBa2Cu3O7, A LOW DIMENSIONAL, LOW DENSITY OF STATES SUPERCONDUCTORS. *Phys. Lett. A.* **122**, 4–8 (1987).

94. A. J. F. Jaejun YU, S. MASSIDDA, BONDS, BANDS, CHARGE TRANSFER EXCITATIONS AND SUPERCONDUCTIVITY OF YBa2Cu3O7-x. *Phys. Lett. A.* **122**, 203–208 (1987).

95. P. J. D. and W.M. Temrnermann, G.M. Stocks, P.A. Stcme, Electronic structure of La-Cu and Y-Ba-Cu oxides: ground-state properties and photoemission spectra. *J. Phys. F, 17 ,135.* (1987).

96. and O. J. J. Zaanen, M. Aluani, X-ray absorption of YBCO : A band picture. *Phys. Rev B.* **40** (1989).

97. K. T. P. and A. J. F. J. Yu, Electronic structure and properties of YBa2Cu408. *Phys. C.* **172** (1991).

98. W.Y. Ching, G.-L. Zhao, Y.-N. Xu and K.W. Wong, Orbital- resolved partial density of states in YBa2Cu3O7. *Phys. Rev B.* **43** (1991).

99. T. U. and Y. M. M. Hirao, Electronic band strcuture of YBa2Cu307 and YBa2Cu306 by density funtional pseudopotential method. *Phys. C.* **195**, 230 (1992).

100. P. W. Anderson, The Resonating Valence Bond State in La2CuO4 and Superconductivity. *Sci. 235, 1196 (1987).*

101. J. D. J. J. L. Tallon, C. Bernhard, H. Shaked, R. L. Hitterman, Generic superconducting phase behavior in high-T, cuprates: T, variation with hole concentration in YBa2C3O7-delta. *Phys. Rev. B.* **51**, 911–914 (1995).

102. N. E. F. M.R. Presland, J.L. Tallon, R.G. Buckley, R.S. Liu, General trends in oxygen stoichiometry effects on Tc in Bi and Tl superconductors. *Phys. 176C, 95* (1991), doi:10.1016/0921-4534(91)90700-9.

103. L. Li *et al.*, Diamagnetism and Cooper pairing above T c in cuprates, 1–9 (2010).

104. Y. Wang, L. Li, N. P. Ong, Nernst effect in high- T c superconductors, 1–20 (2006).

105. M. R. N. and C. Pepin, The electronic nature of high temperature cuprate. *Reports Prog. Physics, 66,.* **1547** (2003).

106. J. S. Z. Sefrioui, D. Arias, M. Varela, J. E. Villegas, M. A. Lodpez de la Torre, C. Leon, G.D. Loos, Crossover from a three-dimensional to purely two-dimensional vortex-glass transition in deoxygenated YBa 2 Cu 3 O 7-x thin films. *Phys. Rev 108, 1175.* **60**, 423–429 (1999).

107. T. K. and K. K. Y. Ando, G. S. Boebinger, and A. Passner, Logarithmic Divergence of both In-Plane and Out-of-Plane Normal-State resistivities of Superconducting La2-xSrCuO4 in the Zero-Temperature Limit. *Phys. Rev. Lett.* **75** (1995).

108. and S. K. Y. Ando, K. Segawa, A. N. Lavrov, Charge Transport Porperties of Lightly-Doped Cuprate: Behavior of the Hall Coefficient. *J. Low. Temp. Phys.* **131**, 793–801 (2003).

109. and S. U. T. Ito, K. Takenaka, Systematic Deviation from T-Linear Behavior in the In-Plane Resistivity of YBa2CuO7-y: Evidence for Dominant Spin Scattering. *Phys. Rev. Lett.* **70** (1993).

110. M. R. H. Ding, T. Yokoya, J. C. Campuzano, T. Takahashi, M. Randeria, and J. G. Norman, T. Mochiku, K. Kadowaki, Spectroscopic evidence for a pseudogap in the normal state of underdoped high-TC superconductors. *Nature, 382:51–54* (1996).

111. C. H. P. A. G. Loeser, Z.-X. Shen, D. S. Dessau, D. S. Marshall, and A. K. P. Fournier, Excitation gap in the normal state of underdoped Bi2Sr2CaCu2O8+d. *Sci. 273325–329,*. (1996).

112. and Ø. F. Ch. Renner, B. Revaz, J.-Y. Genoud, K. Kadowaki, Pseudogap precursor of the superconducting gap in under- and overdoped. *Phys. Rev. Lett., 80149–152,*.

113. A. Takeshi Kondo, Tsunehiro Takeuchi, Adam Kaminski, Syunsuke Tsuda, S. Shin., Evidence for two energy scales in the superconducting state of optimally doped (Bi,Pb)2(Sr,La)2CuO6+d. *Phys. Rev. Lett., 98267004,*.

114. R. Kiyohisa Tanaka, W. S. Lee, D. H. Lu, A. Fujimori, T. Fujii, and Z.-X. S. I. Terasaki, D. J. Scalapino, T. P. Devereaux, Z. Hussain, Distinct fermi-momentum-dependent energy gaps in deeply underdoped Bi2212. *Sci. 3141910–1913,* (2006).

115. T. K. M. C. Boyer, W. D. Wise, Kamalesh Chatterjee, Ming Yi, and E. W. H. T. Takeuchi, H. Ikuta, Imaging the two gaps of the high-temperature superconductor Bi2Sr2CuO6+x. *Nat. Phys, 3802–806,* (2007).

116. A. K. R. Khasanov, Takeshi Kondo, S. Str¨assle, D. O. G. Heron, and T. T. H. Keller, S. L. Lee, Evidence for a competition between the superconducting state and the pseudogap state of (BiPb)2(SrLa)2CuO6+d from muon spin rotation experiments. *Rev., Phys. Lett., 101:227002*.

117. J. Chang *et al.*, Direct observation of competition between superconductivity and charge density wave order in YBa2Cu3O6.67. *Nat. Phys.* **8**, 871–876 (2012).

118. a. J. Achkar *et al.*, Distinct charge orders in the planes and chains of ortho-III-ordered YBa 2Cu 3O 6+δ superconductors identified by resonant elastic

X-ray scattering. *Phys. Rev. Lett.* **109**, 1–5 (2012).

119. and F. D. H. A. Mook, Pengcheng Dai, Observation of magnetic moments in the superconducting state of YBa2Cu3O6.6. *Phys. Rev. B, 64012502*.

120. X. Z. No Y. Li, V. Baledent, N. Barisic, Y. Cho, B. Fauque, Y. Sidis, G. Yu, and M. G. P. Bourges, Unusual magnetic order in the pseudogap region of the superconductor HgBa2CuO4+d. *Nature, 455:372–375,*.

121. and A. Michael Vershinin, Shashank Misra, S. Ono, Y. Abe, Yoichi Ando, Yazdani., Local ordering in the pseudogap state of the high-TC superconductor Bi2Sr2CaCu2O8+d. *Sci. 3031995–1998* (2004).

122. A. P. Colin V. Parker, Pegor Aynajian, Eduardo H. da Silva Neto, and A. Y. Shimpei Ono, Jinsheng Wen, Zhijun Xu, Genda Gu, Fluctuating stripes at the onset of the pseudogap in the high-TC superconductor Bi2Sr2CaCu2O8+x. *Nature, 468:677–680,* (2010).

123. N. Olivier Cyr-Choiniere, R. Daou, Francis Laliberte, David LeBoeuf, J. B. G. Doiron-Leyraud, J. Chang, J.-Q. Yan, J.-G. Cheng, J.-S. Zhou, and L. T. S. Pyon, T. Takayama, H. Takagi, Y. Tanaka, Enhancement of the nernst effect by stripe order in a high-TC superconductor. *Nature, 458:743–745,* (2009).

124. and B. B. C. Hess, E.M. Ahmed, U. Ammerahl, A. Revcolevschi, Nernst effect of stripe ordering La1.8−xEu0.2SrxCuO4. *Eur. Phys. J. - Spec. Top. 188103–112,* (2010).

125. T. T. Takeshi Kondo, Yoichiro Hamaya, Ari D. Palczewski, and A. K. J. S. Wen, Z. J. Xu, Genda Gu, Jorg Schmalian, Disentangling cooper-pair formation above the transition temperature from the pseudogap state in the cuprates. *Nat. Phys, 721–25,* (2011).

126. A. Kaminski, T. Kondo, T. Takeuchi, G. Gu, Pairing, Pseudogap and Fermi Arcs in Cuprates. *Condens. Matter* (2014).

127. S.-C. Zhang, A unified theory based on SO(5) symmetry of superconductivity and antiferromagnetism. *Sci. 2751089–1096,* (1997).

128. and D. S. S. L. Sondhi, S. M. Girvin, J. P. Carini, Continuous quantum phase transitions. *Rev. Mod. Phys., 69315–333*.

129. V. F. G. and V. T. Dolgopolov., Superconductor-insulator quantum phase transition. *Physics-Uspekhi, 53:1–49* (2010).

130. and A. M. G. D. B. Haviland, Y. Liu, Onset of superconductivity in the two-dimensional limit. *Phys. Rev. Lett., 622180–2183,*.

131. J. W. H. Y. Liu, K. A. McGreer, B. Nease, D. B. Haviland, G. Martinez, and A. M. Goldman., Scaling of the insulator-to-superconductor transition in ultrathin amorphous Bi films. *Phys. Rev. Lett., 672068–2071,*.

132. A. F. H. and M. A. Paalanen., Magnetic-field-tuned superconductorinsulator transition in two-dimensional films. *Phys. Rev. Lett., 65927–930*.

133. and R. R. R. M. A. Paalanen, A. F. Hebard, Low-temperature insulating phases of uniformly disordered two-dimensional superconductors. Phys. Rev. Lett., 69:1604–1607, Sep 1992. *Phys. Rev. Lett., 691604–1607*.

134. A. Y. and A. Kapitulnik., Superconducting-insulating transition in two-dimensional a-MoGe thin films. *Phys. Rev. Lett., 743037–3040*.

135. K. A. P. et Al., Electrostatic tuning of the superconductor-insulator transition in two dimensions. *Phys. Rev. Lett., 94197004,*.

136. D. W. Greve, *Field Effect Devices and Applications* (Prentice H., 1998).

137. a. Spinelli, M. a. Torija, C. Liu, C. Jan, C. Leighton, Electronic transport in doped SrTiO_{3} : Conduction mechanisms and potential applications. *Phys. Rev. B.* **81**, 1–14 (2010).

138. B. G. Streetman, *Solid State Electronic Devices* (2nd Editio., 1980).

139. J. E. Lilienfeld, U.S. Patent 1, 745, 175 (1926).

140. and Y. I. H. Shimotani, H. Asanuma, J. Takeya, Electrolyte-gated charge accumulation in organic single crystals. *Appl. Phys. Lett. 89*. **203501** (2006), doi:10.1063/1.2387884.

141. Y. Zhou, S. Ramanathan, Correlated Electron Materials and Field Effect Transistors for Logic : A Review. *Crit. Rev. Solid State Mater. Sci.* (2013).

142. G. K. and G. M. D. S. Fisher, Midgap states in doped Mott insulators in infinite dimensions. *Phys. Rev. B, 52*. **52**, 17112–17118 (1995).

143. R. O. A. J. W. Allen, C. G. Olson, M. B. Maple, J. S. Kang, L. Z. Liu, J. H. Park, Y. D. and R. L. W. P. Ellis, J. T. Markert, Resonant photoemission study of Nd2-xCexCuO4-y: Nature of electronic states near the Fermi level. *Phys. Rev. Lett. 64,*. **64**, 595–598 (1990).

144. G. A. S. and W. A. G. M. A. van Veenendaal, Electronic structure of Bi2Sr2Ca1-xYxCu2O8+δ: Cu 2p x-ray-photoelectron spectra and occupied and unoccupied low-energy states. *Phys. Rev. B, 49*. **49** (1994).

145. G. A. S. and H. V. P. Kuiper, G. Kruizinga, J. Ghijsen, Character of Holes in LixNi1-xO and Their Magnetic Behavior. *Phys. Rev. Lett. 62*. **62**, 221–224 (1989).

146. M. C. T. Chen, F. Sette, Y. Ma, M. S. Hybertsen, E. B. Stechel, W. M. C. Foulkes, Z. H. Schulter, S. W. Cheong, A. S. Cooper, L. W. Rupp, Jr., B. Batlogg, Y. L. Soo, A. K. and Y. H. K. Ming, Electronic states in La2-xSrxCuO4 probed by soft-x-ray absorption. *Phys. Rev. Lett. 66*. **66**, 104–107 (1991).

147. G. B. and R. M. Sing, S. Glawion, M. Schlachter, M. R. Scholz, K. Goss, J. Heidler, Claessen., Photoemission of a Doped Mott Insulator : Spectral Weight Transfer and a Qualitative Mott-Hubbard Description. *Phys. Rev. Lett. 106*. **056403**, 1–4 (2011).

148. J. C. Duchene et al., Initiation of switching in VO2 Coplanar devices. *Electron Devices, IEEE Trans. 18* (1971), doi:10.1109/T-ED.1971.17347.

149. C. N. Berglund, Thermal Filaments in Vanadium Dioxide. *Electron Devices, IEEE Trans. 16* (1969), doi:10.1109/T-ED.1969.16773.

150. and J. C. D. G. B. Adam, Electro Thermal Initiation of Switching in Sandwich Structures. *Solid State Comm. 9*.

151. and J. C. D. G. B. Adam, Pulse Investigation of Switching Delays in VO2 Coplanar Devices. *Electron Devices, IEEE Trans. 19* (1972).

152. and R. S. A. Mansingh, The mechanism of electrical threshold switching in VO , cry st als. *J. Phys. C Solid State Phys. 13* (1980).

153. and S. B. K. A. Mansingh, R. Singh, Electrical Switching in Single Crystal VO2. *Solid-State Elec. 23* (1980).

154. S. R. Ovshinsky, Reversible Electrical Switching Phenomena in Disordered Structures. *Phys. Rev. Lett. 21*. **21** (1968).

155. M. P. Shaw, Thermal Instability - The Precursor to Switching in Inhomogeneous Thin Films. *Electron Devices, IEEE Trans. 26* (1979).

156. and S. N. M. D. Adler, H. K. Henisch, The mechanism of threshold switching in amorphous alloys. *Rev. Mod. Phys. 50*. **50** (1978).

157. D. S. G. Stefanovich, A. Pergament, Electrical switching and Mott transition in VO2. *J. Phys. Condens. Matt. 12*, 8837–8845 (2000).

158. F. A. Chudnovskii et al., Switching phenomena in chromium-doped vanadium sesquioxide. *J. Appl. Phys. 84* (1998).

159. A. Asamitsu, Y. Tomioka, H. Kuwahara, Y. Tokura, Current switching of resistive states in magnetoresistive manganites. *Nat. 388*. **388**, 1995–1997 (1997).

160. S. Yamanouchi, Y. Taguchi, Y. Tokura, Dielectric Breakdown of the Insulating Charge-Ordered State in La 2 2 x Sr x NiO 4. *Phys. Rev. Lett. 83*, 5555–5558 (1999).

161. Y. Taguchi, T. Matsumoto, Y. Tokura, T. Sr, Dielectric breakdown of one-dimensional Mott insulators Sr 2 CuO 3 and SrCuO 2. *Phys. Rev. B 62*. **62**, 7015–7018 (2000).

162. H. Kim, B. Chae, D. Youn, Mechanism and observation of Mott transition in VO2-based two- and three-terminal devices. *New J. Phys. 6*. **52** (2004).

163. H. Kim, Raman study of electric-field-induced first- order metal-insulator transition in VO2-based devices. *Appl. Phys. Lett. 86* (2005).

164. B. G. Chae, Abrupt metal – insulator transition observed in VO 2 thin films induced by a switching voltage pulse. *Phys. B Condens. Matt. 369*. **369**, 76–80 (2005).

165. J. S. K. Okimura, Time-dependent Characteristics of Electric Fieldinduced Metal–Insulator Transition of Planer VO2/c-Al2O3 Structure. *Jpn J. Appl. Phys. 46*. **813** (2007), doi:10.1143/JJAP.46.L813.

166. J. Cao *et al.*, Constant threshold resistivity in the metal-insulator transition of VO 2. *Phys. Rev. B 82*, 1–4 (2010).

167. S. Lee et al., Electrically driven phase transition in magnetite nanostructures. *Nat. Mater. 7* (2008).

168. X. Zhong *et al.*, Avalanche breakdown in microscale VO2 structures Avalanche breakdown in microscale VO 2 structures. *J. Appl. Phys. 110*. **084516**, doi:10.1063/1.3654121.

169. M. Eckstein, T. Oka, P. Werner, Dielectric Breakdown of Mott Insulators in Dynamical Mean-Field Theory. *Phys. Rev. Lett. 105*. **146404**, 1–4 (2010).

170. T. Oka, R. Arita, H. Aoki, Breakdown of a Mott Insulator : A Nonadiabatic Tunneling Mechanism. *Phys. Rev. Lett. 91*, 1–4 (2003).

171. and H. A. T. Oka, R. Arita, Nonlinear transport in a one-dimensional Mott insulator in strong electric fields. *Phys. B Condens. Matt. 359-36*. **361**, 759–761 (2005).

172. N. Sugimoto, S. Onoda, N. Nagaosa, Field-induced metal-insulator transition and switching phenomenon in correlated insulators. *Phys. Rev. B 78*, 1–5 (2008).

173. F. H.-M. et Al., Nonequilibrium electronic transport in a one-dimensional Mott insulator. *Phys. Rev. B 82*, 1–11 (2010).

174. a Ohtomo, H. Y. Hwang, A high-mobility electron gas at the LaAlO3/SrTiO3 heterointerface. *Nature*. **427**, 423–426 (2004).

175. S. Thiel, G. Hammerl, a Schmehl, C. W. Schneider, J. Mannhart, Tunable quasi-two-dimensional electron gases in oxide heterostructures. *Science*. **313**, 1942–1945 (2006).

176. H. S. P. Wong., Beyond the conventional transistor. *IBM J. Res. Dev. 46*. **46**, 133–168 (2002).

177. J. R. Miller, P. Simon, FUNDAMENTALS OF ELECTROCHEMICAL CAPACITOR DESIGN AND OPERATION. **c**.

178. J. R. Miller, IEEE Electrical Insulation Magazine 0883. *IEEE Electr. Insul. Mag. 0883* (2010).

179. H. von Helmholtz, No Title. *Pogg. Ann. LXXXIX*, *211* (1853).

180. R. Kötz, R. Kötz, M. Carlen, M. Carlen, Principles and applications of electrochemical capacitors. *Electrochim. Acta*. **45**, 2483–2498 (2000).

181. M. M. and A. F. H. R. Misra, Electric field gating with ionic liquids. *Appl. Phys. Lett. 90*, 052905–052903 (2007).

182. L. A. B. and J. O. T. J. R. Thompson, Very low-temperature search for superconductivity in semiconducting KTaO3. *J. Low Temp. Physics*, *47*, 467–475 (1982).

183. M. Lee, J. R. Williams, S. Zhang, C. D. Frisbie, D. Goldhaber-Gordon, Electrolyte gate-controlled kondo effect in SrTiO 3. *Phys. Rev. Lett.* **107**, 1–5 (2011).

184. Y. Lee *et al.*, Phase diagram of electrostatically doped SrTiO3. *Phys. Rev. Lett.* **106**, 1–4 (2011).

185. M. Nakano *et al.*, Collective bulk carrier delocalization driven by electrostatic surface charge accumulation. *Nature*. **487**, 459–462 (2012).

186. Z. Yang, Y. Zhou, S. Ramanathan, Studies on room-temperature electric-field effect in ionic-liquid gated VO 2 three-terminal devices. *J. Appl. Phys.* **111**, 2–6 (2012).

187. S. Asanuma *et al.*, Tuning of the metal-insulator transition in electrolyte-gated NdNiO 3 thin films. *Appl. Phys. Lett.* **97**, 3–6 (2010).

188. B. R. Scherwitzl *et al.*, Electric-Field Control of the Metal-Insulator Transition in Ultrathin NdNiO 3 Films. *Adv. Mater. 22*, 5517–5520 (2010).

189. E. J. A. and C. N. J. B. Torrance, P. Lacorre, A. I. Nazzal, Systematic study of insulator-metal transitions in perovskites RNiO3 (R=Pr,Nd,Sm,Eu) due to closing of charge-transfer gap. *Phys. Rev. B, 45*. **45**, 8209–8212 (1992).

190. A. S. C. and P. C. C. S. W. Cheong, H. Y. Hwang, B. Batlogg, Electron-hole doping of the metal-insulator transition compound ReNiO3. *Phys. B Condens. Matter, 194-196, Part 1,*. **1087-1088** (1994).

191. M. J. M.-L. and J. A. A. J. L. Garcia-Munoz, M. Suaaidi, Influence of carrier injection on the metal-insulator transition in electron- and hole-doped R1-xAxNiO3 perovskites. *Phys. Rev. B, 52,*. **52**, 13563–13569 (1995).

192. S. M. U. Staub, G. I. Meijer, F. Fauth, R. Allenspach, J. G. Bednorz, J. Karpinski, L. P. and F. d'Acapito Kazakov, Direct Observation of Charge Order in an Epitaxial NdNiO 3 Film. *Phys. Rev. Lett. 88,*. **126402** (2002), doi:10.1103/PhysRevLett.88.126402.

193. I. I. Mazin *et al.*, Charge Ordering as Alternative to Jahn-Teller Distortion. *Phys. Rev. Lett. 98,*. **176406** (2007), doi:10.1103/PhysRevLett.98.176406.

194. K. Shimamura *et al.*, Electrical control of Curie temperature in cobalt using an ionic liquid film Electrical control of Curie temperature in cobalt using an ionic liquid film. *Appl. Phys. Lett. 100*. **122402** (2012), doi:10.1063/1.3695160.

195. A. Guinier, Xray diffraction in crystals, imperfect crystals and amorphous bodies. *Dover Publ.* (1994).

196. E. E. Fullerton, I. K. Schuller, Structural refinement of superlattices from x-ray diffraction. *Phys. Rev B.* **45**, 9292–9310 (1992).

197. O. Nakamura, E. E. Fullerton, J. Guimpel, I. K. Schuller, High Tc thin films with roughness smaller than one unit cell. *Appl. Phys. Lett. 60*, 120–122 (1992).

198. D. M. Kelly, E. E. Fullerton, J. Santa-maria, I. K. Schuller, X-RAY REFLECTIVITY FROM MULTILAYERS WITH CUMULATIVE ROUGHNESS ROUGHNESS. *Scr. Met. Mater. 33, 1603* (1995).

199. R. Egerton, Rep. Prog. Phys. 72, 016502 (2009).

200. O. L. Krivanek, G. J. Corbin, N. Dellby, B. F. Elston, R. J. Keyse, M. F. Murfitt, C. S. Own, Z. S. Szilagyi, and J. W. Woodruff, Ultramicroscopy 108, 179 (2008).

201. C. Jeanguillaume and C. Colliex, Ultramicroscopy 28, 252 (1989).

202. J. M. Cowley, Bull. Mater. Sci. 6, 477 (1984).

203. S. J. Pennycook, and L. A. Boatner, Nature 336, 565 (1988).

204. S. J. Pennycook, Ultramicroscopy 30, 58 (1989).

205. E. Okunishi, I. Ishikawa, H. Sawada, F. Hosokawa, M. Hori and Y. Kondo, Microsc. Microanal. 15, 164 (2009).

206. S. D. Findlay, N. Shibata, and H. Sawada, Appl. Phys. Lett. 95, 191913 (2009).

207. and S. J. P. N. D. Browing, M. F. Chisholm, No Title. *Nature*. **366, 143** (1993).

208. P. E. Batson, No Title. *Nature*. **366, 727** (1993).

209. and S. P. N. Browning, D. Wallis, P. Nellist, No Title. *Micron*. **28, 333** (1997).

210. and J. H. P. O. L. Krivanek, No Title. *Ultramicroscopy*. **32, 313** (1990).

211. and P. R. B. J. H. Rask, B. A. Miner, No Title. *Ultramicroscopy*. **21, 321** (1987).

212. V. der Pauw, A method of measuring the resistivity and Hall coefficient on lamellae of arbitrary shape. *Philips Tech. Rev.* (1958).

213. A. R. Irvine, J. T. S.; Sinclair, D. C.; West, Electroceramics: Characterization by Impedance Spectroscopy. *Adv. Mater.* **2, (3), 13** (1990).

214. R. Schmidt, in *In Ceramic Materials Research Trends, Lin, P. B., Ed. Hauppauge*, (2007), p. p 321.

215. M. U. Penner-Hahn, J.E., The University of Michigan, Ann Arbor.

216. C. for A. R. S. Newville, Matthew, Fundamentals of XAFS (2004).

217. Bearden, J. A.; Burr, A. F. Rev. Mod. Phys. 1967, 39, 125–142.

218. James, R. W. The Optical Principles of the Diffraction of X-ray; Ox Bow Press, 1982.

219. Markowicz, A. A. In Handbook of X-ray Spectrometry; 2nd ed.; Van Grieken, R. E., Markowicz, A. A., Eds.; Marcel Dekker: New York, 2002.

220. Compton, A. H.; Allison, S. K. X-rays in Theory and Experiment; 2nd ed.; D. Van Nostrand Company: Princeton, 1935.

221. X-ray Data Booklet, 2nd ed.; Thompson, A. C.; Vaughan, D. Eds.; Lawrence Berkeley National Laboratory: Berkeley, 2001.

222. Bearden, J. A. Rev. Mod. Phys. 1967, 39, 78.

223. Krause, M. O.; Oliver, J. H. J. Phys. Chem. Ref. Data 1979, 8, 329.

224. Pettifer, R. F.; Borowski, M.; Loeffen, P. W. J. Synchrot. Radiat. 1999, 6, 217–219.

225. G. S. . E. Jaklevic, J.; Kirby, J. A.; Klein, M. P.; Robertson, A. S.; Brown, Jaklevic, J.; Kirby, J. A.; Klein, M. P.; Robertson, A. S.; Brown, G. S.; Eisenberger, P. Solid State Commun. 1977, 23, 679–682. *P. Solid State Commun. 23*. **23**, 679–682 (1977).

226. A. T. Ellis, *In Handbook of X-ray Spectrometry; 2nd ed.; Van Grieken, R. E., Markowicz, A. A., Eds.; Marcel Dekker: New York.* (2002).

227. J. J. Haase, No Title. *Chem. Soc.-Faraday Trans.* **92**, 1653–1667 (1996).

228. M. P. Kirby, J. A.; Goodin, D. B.; Wydrzynski, T.; Robertson, A. S.; Klein, No Title. *J. Am. Chem. Soc.* **103**, 5537–5542 (1981).

229. N. V. D'Angelo, P.; Benfatto, M.; Della Longa, S.; Pavel, No Title. *Phys. Rev. B.* **66** (2002).

230. C. W. . Steinberger, I. T.; Teodorescu, C. M.; Gravel, D.; Flesch, R.; Wassermann, B.; Reichardt, G.; Hutchings, E. Hitchcock, A. P.; Ruhl, No Title. *Phys. Rev. B.* **60**, 3995–4004 (1999).

231. E. I. Kau, L. S.; Spira-Solomon, D. J.; Penner-Hahn, J. E.; Hodgson, K. O.; Solomon, No Title. *J. Am. Chem. Soc.* **109**, 6433–6442 (1987).

232. Stern, E. A.; Sayers, D. E.; Lytle, F. W. Phys. Rev. B 1975, 11, 4836–4846.

233. Lee, P. A.; Pendry, J. B. Phys. Rev. B 1975, 11, 2795–2811.

234. Ashley, C. A.; Doniach, S. Phys. Rev. B 1975, 11, 1279–1288.

235. M. Varela, W. Grogger, D. Arias, Z. Sefrioui, C. Leon, L. Vazquez, C. Ballesteros, K. M. Krishnan, J. Santamarıa, Effects of epitaxial strain on the growth mechanism in YBCO thin films in YBco/PBCO superlattices. *Phys. Rev B.* **66, 174514**, 2–7 (2002).

236. J.-M. Triscone, Ø. Fischer, Superlattices of high-temperature superconductors: synthetically modulated structures, critical temperatures and vortex dynamics. *Reports Prog. Phys.* **60**, 1673–1721 (1997).

237. M. V. J.Santamaria, C.Ballesteros, C.Leon, Z. Sefrioui, D. Arias, Epitaxial mismatch strain in YBCO/PBCO superlattices. *Phys. Rev. B.* **62**, 509–515 (2000).

238. L. X. Cao *et al.*, Strain release and twin structure in GdBa2Cu3O7-d films on (001)SrTiO3 and NdGaO3. *Phys. Rev B.* **65**, 1–4 (2002).

239. M. Salluzzo *et al.*, Thickness effect on the structure and superconductivity of Nd1.2Ba1.8Cu3Oz epitaxial films, 1–12 (2005).

240. M. Varela *et al.*, Intracell Changes in Epitaxially Strained YBa2Cu3O7-x Ultrathin Layers in YBa2Cu3O7-x/PrBa2Cu3O7 Superlattices. *Phys. Rev. Lett.* **83**, 3936–3939 (1999).

241. M. Varela, thesis (2001).

242. M. K. and Y. H. Yuan, H. Shimotani, J. Ye, S. Yoon, H. Aliah, A. Tsukazaki, Iwasa., Electrostatic and electrochemical nature of liquid-gated electric-double-layer transistors based on oxide semiconductors. *J. Am. Chem. Soc.* **132**, 18402–18407 (2010).

243. T. Fujimoto, K. Awaga, Electric-double-layer field-effect transistors with ionic liquids. *Phys. Chem. Chem. Phys.* **15**, 8983–9006 (2013).

244. T. Sato, G. Masuda, K. Takagi, Electrochemical properties of novel ionic liquids for electric double layer capacitor applications. *Electrochim. Acta*. **49**, 3603–3611 (2004).

245. K. R. S. Natalia V. Plechkova, *Ionic Liquids further UnCOILed. Critical experts overview.* (Wiley, 2014).

246. A.K.Jonscher, *Dielectric relaxation in Solids. Chelsea Dielectric Press,London*, (1983).

247. W. K. Lee, J. F. Liu, A. S. Nowick, Limiting behavior of ac conductivity

in ionically conducting crystals and glasses: A new universality. *Phys. Rev. Lett.* **67**, 1559–1561 (1991).

248. Y. Zhou, S. Ramanathan, Relaxation dynamics of ionic liquid-VO 2 interfaces and influence in electric double-layer transistors. *J. Appl. Phys.* **111** (2012), doi:10.1063/1.4704689.

249. T. Ichimura, K. Fujiwara, H. Tanaka, Dual field effects in electrolyte-gated spinel ferrite: electrostatic carrier doping and redox reactions. *Sci. Rep.* **4**, 2–6 (2014).

250. A. A. Abrikosov, L. P. G. O. R. Kov, ON THE PROBLEM OF THE KNIGHT SHIFT IN SUPERCONDUCTORS. **12**, 337–339 (1961).

251. N. Doiron-leyraud *et al.*, Quantum oscillations and the Fermi surface in an underdoped high- T c superconductor. **447**, 565–568 (2007).

252. A. Gaur, B. D. Shrivastava, S. K. Joshi, Copper K-edge XANES of Cu(I) and Cu(II) oxide mixtures. *J. Phys. Conf. Ser.* **190**, 012084 (2009).

253. H. Tolentino *et al.*, Valence changes of copper under oxygen uptake and removal in YBa2Cu3O7−δ observed in situ by X-ray absorption spectroscopy. *Phys. Lett. A.* **139**, 474–480 (1989).

254. A. R. M. and Y. X. J.M. Tranquada, S.M.Heald, Mixed valency, hole concentration, and TC in YB2C3O6+x. *Phys. Rev B.* **38** (1988).

255. R. Y. T.i lwazumi, I. Nakai, M. IzumI, H.oyanagi, H. Sawada, H. Ikeda, Y. Saito. Y. Abe, K. Takita, STUDY ON COPPER VALENCY OF HIGH-T SUPERCONDUCTOR YBa~Cu~O~ BY HIGH TEMPERATURE X-RAY A§SORPTION SPECTROSCOPY. **65**, 303–310 (1988).

256. N. Gauquelin *et al.*, Atomic scale real-space mapping of holes in YBa2Cu3O(6+δ). *Nat. Commun.* **5**, 4275 (2014).

257. L. M.-S. P. Giannozzi, S. Baroni, N. Bonini, M. Calandra, R. Car, C. Cavazzoni, D. Ceresoli, G. L. Chiarotti, M. Cococcioni, I. Dabo, A. Dal Corso, S. Fabris, G. Fratesi, S. de Gironcoli, R.Gebauer, U. Gerstmann, C. Gougoussis, A. Kokalj, M. Lazzeri, QUANTUM ESPRESSO: a modular and open-source software project for quantum simulations of materials. *J.Phys.Condens.Matter*,. **21** (2009).

258. A. P. S. and F. M. C. Gougoussis, M. Calandra, First-principles calculations of X- ray absorption in a scheme based on ultrasoft pseudopotentials: From α-quartz to high-Tc compounds. *Phys. Rev. B.* **80** (2009).

259. D. P. and G. G. D. Prendergast and G. Galli, X-ray absorption spectra of water from first-principles calculations. *Phys. Rev. Lett.* **96** (2006).

260. D. P. and S. G. Louie, Bloch- state-based interpolation: An efficient generalization of the Shirley approach to interpolating electronic structure.

Phys. Rev. B. **80** (2009).

261. G. A. S. D. G.Hawthorn, K. M.Shen, J. Geck, D. C.Peets, H. Wadati, J. Okamoto, S.W. Huang, D. J. Huang, H.J.lin, J.D.Denlinger, R. Liang, D.A. Bonn, W.N.Hardy, Resonant elastic soft x-ray scattering in oxygen-ordered YBa 2Cu3O6. *Phys. Rev. B - Condens. Matter Mater. Phys.* **84**, 1–10 (2011).

262. R. A. B. B. H. Moeckly, D. K. Lathrop, Electromigration Study of Oxygen Disorder and Grain-Boundary Effects in YBa2Cu3O7-d thin films,. *Phys. Rev. B.* **47**, 400–417 (1993).

263. T. S. R. K Govinda Rajan, P Parameswaran, J Janaki, Electromigration of oxygen in YBa2Cu3O7-d. *J. Phys. D Appl. Phys.* **23** (1990).

264. Y. Zhou *et al.*, Control of Emergent Properties at a Correlated Oxide Interface with Graphene. *Nano Lett.* **15**, 1627–1634 (2015).

265. C. R. Lattices, Absence of Diffusion in Certain Random Lattices. **386** (1956).

266. L. Taillefer, Scattering and Pairing in Cuprate Superconductors. *Annu. Rev. Condens. Matter Phys.* **1**, 51–70 (2010).

267. A. S. Dhoot *et al.*, Increased T(c) in electrolyte-gated cuprates. *Adv. Mater.* **22**, 2529–2533 (2010).

268. H. Schäfer, E. Sternin, R. Stannarius, M. Arndt, F. Kremer, Novel approach to the analysis of broadband dielectric spectra. *Phys. Rev. Lett.* **76**, 2177–2180 (1996).

269. L. Joly, C. Ybert, E. Trizac, L. Bocquet, Hydrodynamics within the electric double layer on slipping surfaces. *Phys. Rev. Lett.* **93**, 1–4 (2004).

270. Y. Lauw, M. D. Horne, T. Rodopoulos, F. A. M. Leermakers, Room-Temperature Ionic Liquids: Excluded Volume and Ion Polarizability Effects in the Electrical Double-Layer Structure and Capacitance. *Phys. Rev. Lett.* **103**, 1–4 (2009).

271. D. T. Limmer, Interfacial Ordering and Accompanying Divergent Capacitance at Ionic Liquid-Metal Interfaces. *Pysical Rev. Lett.* **115**, 256102 (2015).

272. A. A. Kornyshev, Double-Layer in Ionic Liquids: Paradigm Change? *J. Phys. Chem. B.* **111**, 5545–5557 (2007).

273. K. B. Oldham, A Gouy-Chapman-Stern model of the double layer at a (metal)/(ionic liquid) interface. *J. Electroanal. Chem.* **613**, 131–138 (2008).

274. M. T. Alam, M. M. Islam, M. T. Alam, T. Ohsaka, T. Ohsaka, Electrical Double-Layer Structure in Ionic Liquids: A Corroboration of the

Theoretical Model by Experimental Results. *J. Phys. Chem. C*. **112**, 16568–16574 (2008).

275. M. Islam, M. T. Alam, T. Okajima, T. Ohsaka, Electrical Double Layer Structure in Ionic Liquids : An Understanding of the Unusual Capacitance - Potential Curve at a Nonmetallic Electrode. **2**, 3386–3389 (2009).

276. P. Simon, Y. Gogotsi, Materials for electrochemical capacitors. *Nat. Mater.* **7**, 845–854 (2008).

277. E. Dagotto, T. Hotta, A. Moreo, Colossal magnetoresistant materials: the key role of phase separation. *Phys. Rep.* **344**, 1–153 (2001).

278. Y. Tokura, N. Nagaosa, Orbital Physics in Transition-Metal Oxides. *Science (80-.).* **288** (2000), pp. 462–468.

279. E. Dagotto, Complexity in strongly correlated electronic systems. *Science*. **309**, 257–262 (2005).

280. Y. Tokura, Correlated-Electron Physics in Transition-Metal Oxides. *Phys. Today*. **56**, 50 (2003).